ABSTRACT

Title of dissertation: MEASUREMENT OF COUPLING BETWEEN THE ELECTRON GAS AND NANOMECHANICAL MODES

Patrick A. Truitt
Doctor of Philosophy, 2007

Dissertation directed by: Adjunct Professor Keith Schwab
Department of Physics

One of the challenges for nanomechanical devices is to understand the different sources of noise and dissipation that act on such systems. In thermal equilibrium, these noise sources all have the same temperature and are thus indistinguishable from each other. It has been proposed, however, that the noise from electrons scattering off impurities and boundaries in the nanoresonator can be driven above the bath noise by applying a voltage across the resonator. The force acting on the nanoresonator due to these collisions is predicted to be detectable with current technology.

Here we describe experiments to measure this noise. Using a radio-frequency single electron transistor to measure the effective temperature of a nanomechanical mode, we have found that a) the mode temperature increases linearly with current through the nanoresonator and b) the mode temperature follows the expected temperature of the electron gas due to Joule heating.

We have not been able to identify the associated damping, however. Experi-

ments on aluminum based nanoresonators have failed to yield the expected increase in dissipation at the crossover between the superconducting and normal states. We are left to conclude that the nanomechanical mode is coupled to the electron gas, but it is unclear whether this coupling is direct or the result of an intermediate dissipative system that itself is heated by the electron gas.

MEASUREMENT OF COUPLING BETWEEN THE ELECTRON GAS AND NANOMECHANICAL MODES

by

Patrick A. Truitt

Dissertation submitted to the Faculty of the Graduate School of the
University of Maryland, College Park in partial fulfillment
of the requirements for the degree of
Doctor of Philosophy
2007

Advisory Committee:
Professor Dennis Drew, Chair
Professor Keith Schwab, Advisor
Professor Alex Dragt
Professor Steven Anlage
Professor John Cumings
Professor Peter Sandborn

Dedication

To My Family

ACKNOWLEDGEMENTS

I will always count myself priveleged to have worked with the talented individuals who made up the nanomechanics group at LPS. First, I thank my advisor, Keith Schwab, for creating a research environment that was dedicated to challenging experiments and high-level scientific achievement, while also being fun to work in. I feel fortunate for the insights into physics and being a successful scientist that I have gained from him.

Keith also brought together an amazingly talented group of individuals that I am thankful to have worked with. Everyone was a joy to work with and I count my labmates as not only colleagues, but also friends.

When I first joined the group, I had almost no experimental research experience. My first project was done under the guidance of Alex Hutchinson, who taught me much of what I know about running cryogenic systems. I am also thankful to Olivier Buu, who was a constant source of information and entertainment. Whenever there was something I was not sure of how to do, Olivier would be the one to ask.

I have to thank Matt LaHaye for his work developing the RF-SET displacement detector. The technology he developed made experiments like mine much more possible. I also found his dissertation invaluable when it became my turn to operate the RF-SET.

Of course, the RF-SET would have been of little use to me if it were not for Akshay Naik, who taught me all aspects of its operation. Akshay also taught me how to fabricate devices and how to operate the dilution refigerator.

Emrah Altunkaya, Harish Bhaskaran and Benedetta Camarota were all great friends and made coming to the lab worthwhile even in the most frustrating of times. And I must especially thank Jared Hertzberg, without whose tireless efforts this work would be far less complete. Because of the impending termination of our support from The Laboratory for Physical Sciences, the bulk of this work had to be completed in a short time. Jared's willingness to dedicate his time to assisting me with my work allowed me to get results in a timely manner.

I would also like to thank members of the Physics Department, especially Jordan Goodman, Nicholas Chant, Drew Baden, Greg Sullivan, and Michael Fisher who took interest in the well-being of Keith's students at LPS. Without their intervention, I would not have been able to finish my experiments.

I thank my family, especially my parents, for their love and support over the years. Their encouragement and support helped lead me to undertaking this endeavour and they have done all they can to assist me in reaching my goals.

And finally, I thank Anne Marie, for her patience, love and understanding. Having someone close to me, who I can confide in, who knows what is involved in research, and who I could share the successes and failures of each day with was a great help. I hope she finds as much support from me in all that she does.

Table of Contents

List of Tables

List of Figures

List of Abbreviations

A	cross sectional area of resonator
C_1	capacitance of 1st SET junction
C_2	capacitance of 2nd SET junction
C_c	cable capacitance
C_m	mechanical capacitance
C_{NR}	capacitance between nanoresonator and gate or SET
C_T	tank capacitance
C_Σ	total capacitance of SET
d	gap between nanoresonator and SET or gate
E_C	SET charging energy
G	gain
h	thickness of nanoresonator
I_{DS}	SET drain-source current
I_F	bias current through beam
K_C	electrostatic spring constant
K_{eff}	effective spring constant
l	length of nanoresonator
l_D	length of detector (SET or gate)
L_c	cable inductance
L_m	mechanical inductance
L_T	tank inductance
ℓ	mean free path
M	effective mass
n_e	density of conduction electrons
p_F	Fermi momentum
Q	nanoresonator quality factor
Q_{em}	electromechanical quality factor
Q_e	quality factor due to electrons
Q_G	charge on SET gate
Q_L	loaded quality factor
Q_m	quality factor of resonant mode
Q_p	quality factor not due to electrons
Q_T	tank quality factor
R_0	source resistance
R_c	cable resistance
R_m	mechanical resistance
R_q	resistance quantum
R_S	set resistance
R_T	tank resistance
R_x	real part of external impedance
S_F	force noise power spectral density
S_X	position noise power spectral density
t_{Au}	thickness of gold

t_{SiN}	thickness of nitride
T	temperature
T_b	bath temperature
T_e	electron temperature
T_m	mode temperature
T_n	noise temperature
T_p	phonon temperature
V_{DS}	SET drain-source voltage
V_G	gate voltage
V_{NR}	coupling voltage between beam and SET or gate
V_p	pump voltage
V_{REF}	calibration signal sent to gate
V_s	drive voltage
V_T	threshold voltage
w	width of nanoresonator
Y_{Al}	Young's modulus of aluminum
Y_{Au}	Young's modulus of gold
Y_{SiN}	Young's modulus of nitride
Z_{LC}	characteristic impedance
Z_T	tank impedance
γ_{em}	electromechanical dissipation
Γ_{11}	reflection coefficient
u	mode shape
ω_T	tank resonance frequency
ω_0	beam resonance frequency

Chapter 1

Introduction

Over the last decade, the ability to fabricate mechanical structures with submicron dimensions has provided a wealth of interesting physics to explore. One such structure is the nanomechanical resonator, a suspended "beam", usually of semi-conducting material, that is either clamped on both ends or with one end free (cantilever). Currently, applications such as ultrasensitive force detection [1], signal processing [2] and ultralow mass sensing [3, 4] are being explored for these devices. In addition, it has been proposed that these devices be used in quantum information processing systems [5, 6].

One aspect of nanomechanical resonators that affects all the applications mentioned above, and that is interesting physics in its own right, is the source of noise and dissipation. Extrinsic souces of dissipation, such as gas damping [7], circuit loading [8], and clamping losses [9] have been studied and are well understood. *Intrinsic* dissipation, however, is much less well understood. While some work has gone into understanding nanomechanical dissipation in terms of such processes as thermoelastic losses [10] or defect motion [11], a comprehensive understanding of the limits of nanomechanical quality factors (a quantity proportional to the inverse of the dissipation) is still lacking.

The purpose of this thesis is to investigate a possible source of dissipation

in metallized nanoresonators: scattering of conduction electrons off impurities and the resonator surface. This process is studied both in terms of the dissipation, by measuring the quality factors of metallized nanoresonators, and the associated fluctuations, by driving current through the metallic layer and observing the position noise of the resonator.

1.1 Structure of the Thesis

The rest of this chapter will review the theory for nanomechanical resonators undergoing flexural motion. It will also introduce the theory for electromechanical noise in such systems. Chapter 2 describes the transduction mechanisms used to read-out the nanoresonator's position. Chapters 3 and 4 provide more detail on the experimental methods used, including device fabrication and operation of the read-out circuitry. Experimental results are presented in chapter 5 and discussed in chapter 6. Finally, an appendix presents more data on the capacitive detection technique.

1.2 Dynamics of a Nanomechanical Resonator

Here I show how a doubly-clamped beam subject to a transverse force can be described by an equivalent mass-spring system (harmonic oscillator). Figure 1.1 illustrates the basic system: the nanoresonator is a doubly-clamped prismatic beam of uniform cross section with width w (in the plane of the substrate), axial length l and thickness h. The bare mass of the nanoresonator is thus $m = \rho A l$ where ρ is

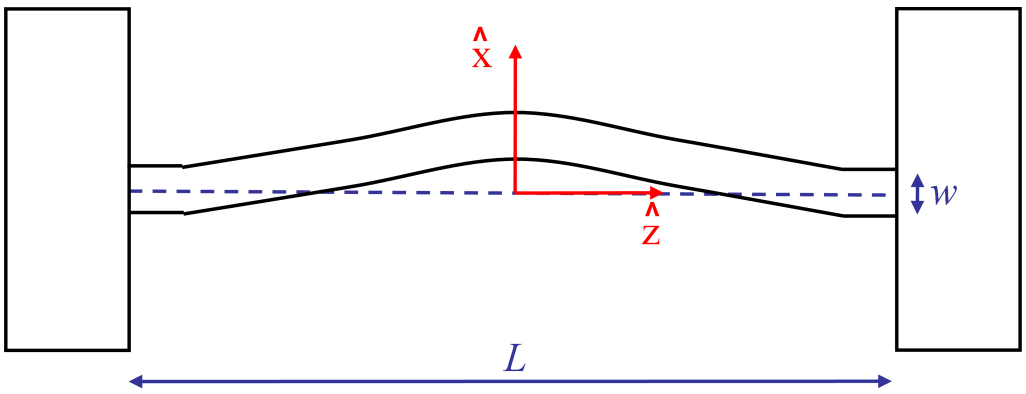

Figure 1.1: Schematic of a doubly clamped beam showing the axes convention used in the text. The beam's axis lies along the $\hat{z}$ direction, with transverse bending motion in the $\hat{x}$ direction (in the plane of the substrate).

the density and A is the cross sectional area. For small displacements, where the cross sectional area of the beam remain deformationless and perpendicular to the beam's axis, the Euler-Bernoulli theory gives the transverse motion of the beam as being governed by [12]

$$\rho A \frac{\partial^2 x}{\partial t^2} + \mu \frac{\partial x}{\partial t} + YI \frac{\partial^4 x}{\partial z^4} = f(t) \tag{1.1}$$

with the boundary conditions that x and its derivative with respect to z at the endpoints must be zero. The third term is the elastic restoring force, where Y is the Young's modulus (a measure of the stiffness), $I = w^3 h/12$ is the bending moment[1] and t is the time. The second term represents the damping, where μ is the dissipation constant. A time varying force per unit length, $f(t) = f_0 e^{i\omega t}$, acting in the $\hat{x}$ direction has also been included.

[1]For metal coated resonators vibrating in the plane of the substrate, replace ρA by $\rho_1 A_1 + \rho_2 A_2$ and YI by $Y_1 I_1 + Y_2 I_2$ where the indices refer to the two materials [13].

To solve Eq. 1.1 I separate variables

$$x(z,t) = X(t)u(z) \tag{1.2}$$

The spatial component, $u(z)$, is known as the mode shape and describes the relative displacement along the beam axis. With the convention that the midpoint of the resonator lies at $z = 0$ it is given by [14]:

$$u(z) = N\left[\cosh(\eta)\cos\left(\frac{2\eta z}{l}\right) - \cos(\eta)\cosh\left(\frac{2\eta z}{l}\right)\right] \tag{1.3}$$

In our experiments, we are concerned with the fundamental flexural mode, for which the eigenvalue η is given by the first nonzero root of $\tan\eta = -\tanh\eta$, so $\eta \simeq 2.365$. The normalization constant, N, is arbitrary. For our purposes, it is convenient to set the normalization by requiring

$$\int_{-l_D/2}^{l_D/2} u(z)\,\mathrm{d}z = l_D \tag{1.4}$$

where l_D is the length of the detector (either the gate for capacitive detection or the SET island for RF-SET detection). The reason for choosing this normalization is that it defines X as the average displacement of the nanoresonator over the length of the detector, which is the measured quantity.

By inserting Eq. 1.2 into 1.1, mulitplying by $u(z)$ and integrating over the length of the nanoresonator, the time-dependent component, $X(t)$ can be shown

[15] to satisfy

$$M\left(\frac{\mathrm{d}^2X}{\mathrm{d}t^2}+\frac{\omega_0}{Q}\frac{\mathrm{d}X}{\mathrm{d}t}\right)+KX=F(t) \tag{1.5}$$

where $\omega_0=\sqrt{K/M}$ is the nanoresonator's resonance frequency, $Q=\omega_0 M/\mu$ is the quality factor, which defines the linewidth of the resonance, and $F(t)$ is the product of the mode shape $u(z)$ and the applied driving force $f(t)$, integrated over the length of the beam. The other coefficients in Eq. 1.5 are given by

$$M = \frac{m}{l}\int_{-l/2}^{l/2}u^2(z)\mathrm{d}z\simeq 0.4m \tag{1.6}$$

$$K = YI\left(\frac{2\eta}{l}\right)^4\int_{-l/2}^{l/2}u^2(z)\mathrm{d}z\simeq 201.3\frac{YI}{l^3} \tag{1.7}$$

where the numerical values are given for a detector length one-tenth the length of the nanoresonator, as was the case with our RF-SET based samples.

To solve for the frequency response, I again separate variables, inserting the sinusoidal solution $X(t)=X_0e^{i\omega t}$ into Eq. 1.5 to find

$$X_0(\omega)=\frac{F/M}{\omega_0^2-\omega^2+i\frac{\omega\omega_0}{Q}} \tag{1.8}$$

For $Q>>1$, this frequency response is the same as for a driven, damped one-dimensional harmonic oscillator (i.e. mass-spring system) [14], with effective spring constant K and effective mass M, such as shown in Fig. 1.2. On resonance, the displacement is given by $X_0(\omega_0)=iFQ/K$.

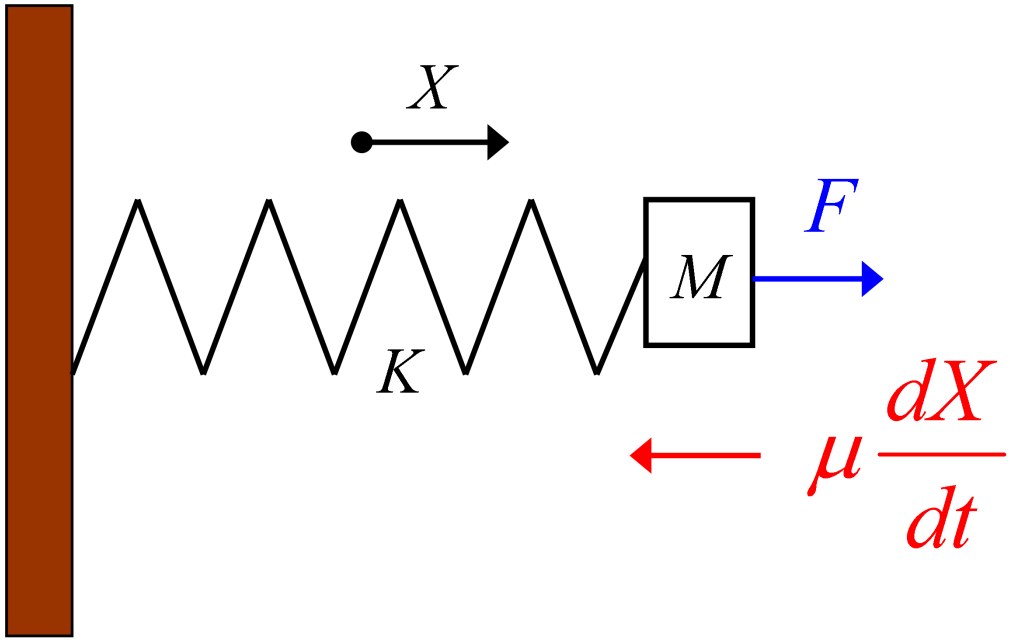

Figure 1.2: The bending beam acts as a mass-spring system with effective mass M and effective spring constant K. The motion is driven by the force $F(t)$. A force proportional to the velocity with proportionality constant μ damps the motion.

1.3 Dissipation and Noise

Equation 1.8 tells us that a nanoresonator subject to a random fluctuating force noise S_F (in units of N^2/Hz), with white spectral density, has a displacement noise (in units of m^2/Hz)

$$S_X = \frac{S_F/M^2}{\left(\omega_0^2 - \omega^2\right)^2 + \left(\frac{\omega\omega_0}{Q}\right)^2} \tag{1.9}$$

in the limit $Q >> 1$. Integrating over ω, we find the total displacement noise power

$$\langle X_0^2 \rangle = \frac{S_F Q^2}{K^2}\frac{\omega_0}{4Q} \tag{1.10}$$

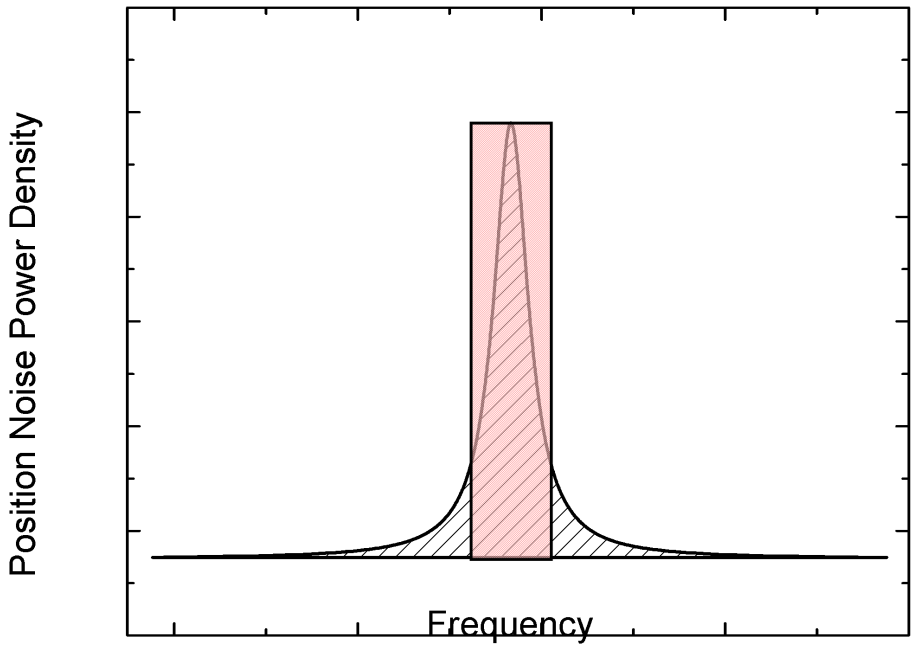

Figure 1.3: Position noise power density as a function of frequency. The area under the Lorentzian is the same as the area in the red box, giving the effective bandwidth $\omega_0/4Q$.

Thus, we can write the integrated response as the response on resonance multiplied by an effective bandwidth $\omega_0/4Q$ (see Fig. 1.3).

Equipartition of energy requires that the integrated response have an energy

$$\frac{1}{2}K\langle X_0^2\rangle = \frac{1}{2}k_BT \tag{1.11}$$

This equality allows us to write the force noise power spectral density as

$$S_F = \frac{4k_BTM\omega_0}{Q} \tag{1.12}$$

Equation 1.12 is an expression of the fluctuation-dissipation theorem [16] that

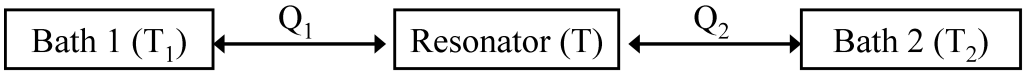

Figure 1.4: A resonator can be coupled to more than one thermal bath. The resulting temperature, T, and quality factor, Q, of the mode are given in the text.

relates the fluctuating forces from a thermal bath at temperature T to the dissipation $(1/Q)$ that thermalizes the resonator mode to the bath. In practice, the resonator mode may be coupled to several different baths, each with their own temperature and associated dissipation. When there is more than one source of noise, the noise powers are simply added together, so we can sum the force noise from each bath according to Eq. 1.12

$$S_F = 4k_B M\omega_0 \left(\frac{T_1}{Q_1} + \frac{T_2}{Q_2} + \cdots + \frac{T_n}{Q_n}\right) \tag{1.13}$$

where T_n and Q_n are the temperature and quality factor associated with bath n. The result is that the resonator mode equilibrates to a temperature

$$T = Q\left(\frac{T_1}{Q_1} + \frac{T_2}{Q_2} + \cdots + \frac{T_n}{Q_n}\right) \tag{1.14}$$

where the net quality factor Q is given by

$$\frac{1}{Q} = \left(\frac{1}{Q_1} + \frac{1}{Q_2} + \cdots + \frac{1}{Q_n}\right) \tag{1.15}$$

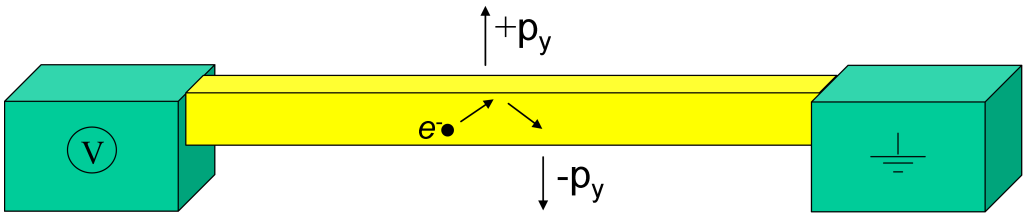

Figure 1.5: The basic idea behind electromechanical noise. Electron collisions impart momentum to the lattice. A voltage bias, V, drives the noise out of equilibrium.

1.4 Electromechanical Noise

This thesis was motivated by a theoretical description of a particular form of noise, known as electromechanical noise, given in a paper by Shytov, Levitov and Beenakker (*Phys. Rev. Lett.*, 88 (2002)). This noise is due to momentum transfer between electrons in a diffusive conductor and the lattice as they undergo collisions with impurities and surface boundaries. In their paper, they describe how this momentum transfer, when applied to a suspended conductor (such as a nanowire or metallized semiconducting nanoresonator), results in an effective transverse force that gives rise to a bending mode in the device.

When the conduction electrons are in thermal equilbrium, electromechanical noise is just one of many sources of dissipation that serve to thermalize the nanoresonator to the bath. In order to distinguish the effect of electromechanical noise, it must be driven out of equilbrium by establishing a voltage bias across the device to raise the energy of the electrons, eV, above the bath energy, $k_B T_b$.

Shytov et al. first give an order of magnitude estimate for the momentum transfer based on the mean scattering time for the electrons. They estimate that only the NeV/E_F electrons within a range eV of the Fermi energy E_F contribute to

the noise, where N is the total number of conduction electrons. They then assume that these electrons transfer a momentum $\Delta_p = p_F$ in a mean scattering time τ. The full Fermi momentum, p_F, is transferred to the lattice due to the elastic nature of the collisions. With these assumptions, the mean-square momentum transfer in a time t is given by

$$\begin{aligned} P \times t &= \frac{NeV}{E_F} (\Delta_p)^2 \left(\frac{t}{\tau}\right) \\ &= Nm_e V \left(\frac{t}{\tau}\right) \end{aligned} \tag{1.16}$$

where m_e is the effective electron mass.

To get a more exact result, the authors take a semiclassical approach, starting with the Boltzmann-Langevin equation

$$\left(\partial_t + v \cdot \nabla_r + eE \cdot \nabla_p + S\right) n = \delta J \tag{1.17}$$

for the distribution function $n(r, p, t)$ with a fluctuating source $\delta J(r, p, t)$ and elastic collision integral S. They find that the approximate momentum transfer to the lattice in the transverse direction is reduced from the value given in Eq. 1.16 by a factor of $(\ell/L)^2$ where ℓ is the mean free path and L is the length of the conductor. This reduction is a consequence of the fact that an electron being scattered back and forth ends up alternatively transferring both positive and negative momentum to the lattice and so many of the collisions tend to cancel each other out.

Applying their theory to the fundamental transverse mode of a doubly-clamped

resonator, they find that the momentum transfer gives rise to a force noise (in N^2/Hz) given by

$$S_F = \frac{4}{5} n_e p_F \frac{\ell A}{L} \int_{-L/2}^{L/2} LK(z) \left[g'(z)\right]^2 \mathrm{d}x \tag{1.18}$$

where n_e is the density of conduction electrons, ℓ is the mean free path, A is the cross sectional area of the conductor of length L with midpoint at $x = 0$ and $g'(z)$ is the first derivative with respect to z of the normalized mode shape. $K(z)$ describes the profile of electron energies across the conductor and for the theory considered here, where $eV >> k_B T_b$ and inelastic electron scattering is absent, $K(z)$ is given by

$$K(z) = (eV/L)z(1 - z/L) \tag{1.19}$$

Finally, Shytov et al. evaluate Eq. 1.18 to find the equivalent force noise applied as a point force at the resonator's center (by normalizing the mode shape by its value at the center) and find

$$S_F = \frac{4}{5} n_e p_F \frac{\ell A}{L} \times 0.83eV \tag{1.20}$$

1.5 Noise at Finite Temperatures

So far, we have ignored the effect of the finite temperature of the bath on the electromechanical noise. First, I note that at zero bias, the conduction electrons will be in thermal equilibrium with the bath, and so the noise is found by replacing the

kernal $K(x)$ in Eq. 1.18 with k_BT. The result is

$$S_F(V=0) = \frac{4}{5} n_e p_F \frac{\ell A}{L} \times 4.87 k_B T_b \tag{1.21}$$

Note that this is only the equilbrium electromechanical noise and does not include other, non-electronic, sources of noise from the bath. This result is also useful in that we can apply it to Eq. 1.12 to find the dissipation associated with the electromechanical noise [17]

$$\frac{1}{Q_{em}} = \frac{4.87}{5} \frac{n_e p_F}{M\omega_0} \frac{\ell A}{l} \tag{1.22}$$

$$= \frac{4.87}{5} \frac{p_F^2}{M\omega_0 e^2} \frac{1}{R} \tag{1.23}$$

The full expression for the electromechanical noise at finite temperature is given by [18]

$$S_F = 3.22 \left[\frac{4}{5} n_e p_F \frac{\ell A}{L}\right] k_B T_b + 0.83 \left[\frac{4}{5} n_e p_F \frac{\ell A}{L}\right] eV \coth \frac{eV}{2k_B T_b} \tag{1.24}$$

In Fig. 1.6, I plot Eq. 1.24 together with the $eV >> k_BT_b$ approximation (Eq. 1.18), with the terms in square brackets in Eq. 1.24 set equal to 1. The error becomes less than 10% for $eV/k_BT_b > 35$.

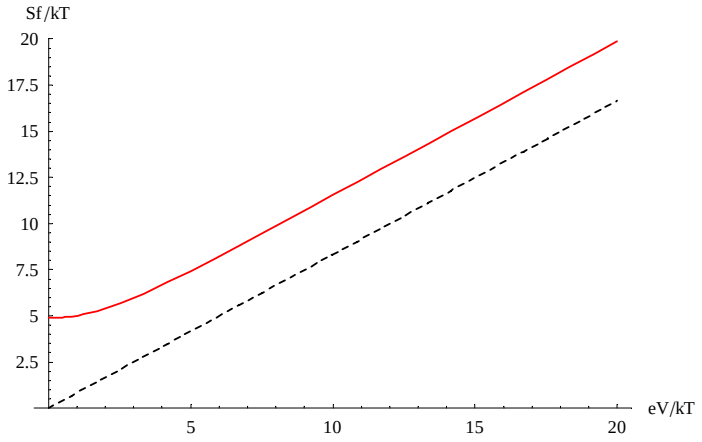

Figure 1.6: Comparison of electromechanical noise in zero (black, dashed) and finite temperature (red, solid) cases.

1.6 Thermalized Electrons

Another process we must include is inelastic electron scattering. In thin gold films, electrons travel a distance on the order of 10 μm [19] before inelastically scattering off another electron (electron-electron scattering). This is the same length as our resonators, so it is not unlikely that such scattering occurs and that the electron gas has a well-defined temperature determined by its connection to the bath and the dissipated power due to the bias current. Another possible inelastic process, electron-phonon scattering, will be considered at the end of this thesis.

Without electron-phonon scattering, the only way for the heat deposited into the electron gas to flow to the bath is through diffusion of the conduction electrons. At low temperatures, this heat flow is governed by the Wiedemann-Franz law [20], which relates the thermal and electrical conductivities. For dissipated power $P = I^2R$ into a wire of resistance R and length L, the temperature profile of the electron gas is given by [21]

$$T_e(z) = T_b\sqrt{1 + \frac{z}{L}\left(1 - \frac{z}{L}\right)p'} \tag{1.25}$$

where $p' = (PR)/(\lambda T_b^2)$ with $\lambda \simeq 2.45 \times 10^{-8}$ (the Lorenz number). The average electron temperature is

$$\langle T_e \rangle = \frac{T_b}{2}\left[1 + \left(\frac{2}{\sqrt{p'}} + \frac{\sqrt{p'}}{2}\right)\arcsin\sqrt{\frac{p'}{4+p'}}\right] \tag{1.26}$$

Putting the above electron temperature profile into the theory for electromechanical

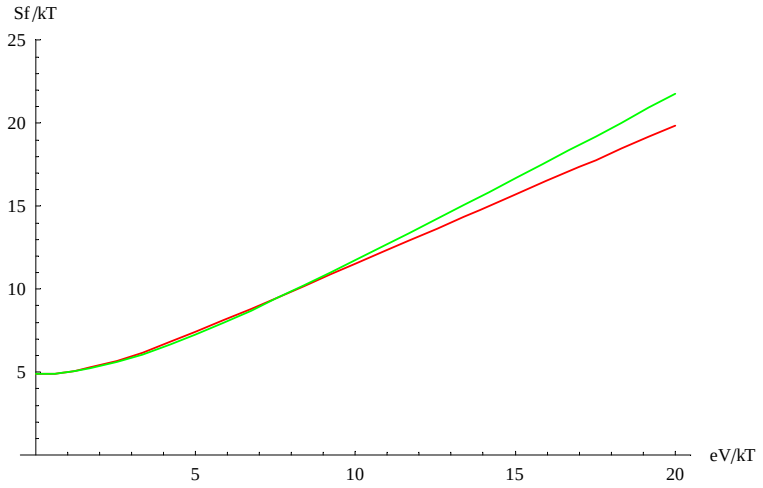

Figure 1.7: Comparison of electromechanical noise for interacting (green, upper curve) and non-interacting (red, lower curve) electrons.

noise results in the force noise [18]

$$S_F = \frac{4.87 k_B T_b}{2} \left[1 + \left(\nu + \frac{1}{\nu} \right) \arctan \nu \right] \tag{1.27}$$

where $\nu = (\sqrt{3}eV)/(2\pi k_B T_b)$. In Fig. 1.7, I plot $S_F/k_B T_b$ for both thermalized and non-thermalized electrons (Eq. 1.24). It is apparent that heating of the electron gas results in a small increase in the force noise.

Finally, I note that the electromechanical noise is very analagous to electrical shot noise, which for a diffusive conductor has the same form as Eq. 1.24 or Eq. 1.27 for non-interacting electrons or interacting electrons, respectively. For $eV >> k_B T_b$

this leads to the observed [19] reduction below the usual $2eI$ value by a factor of $1/3$ in the former case and $\sqrt{3}/4$ in the latter.

Chapter 2

Measurement Scheme

In our experiments, we seek to excite electromechanical noise fluctuations by passing current through the metallic layer of a nanomechanical resonator. In this chapter, I discuss the techniques used for detecting the position fluctuations induced by the electromechanical force noise, starting with a capacitive displacement detection method. This method relies on the changing capacitance between the moving metallized nanoresonator and a nearby gate electrode. This discussion then naturally leads into a discussion of the other displacement detection method used, the radio-frequency single electron transistor (RF-SET) displacement detector, where the nanoresonator is capacitively coupled not to a simple gate, but rather a mesoscopic tunneling device (the SET).

2.1 Capactive Detection

We used a capacitive detection technique for measuring dissipation in aluminum coated resonators in the normal and superconducting states. Application of this technique to nano-electromechanical systems (NEMS) was one of the novel accomplishments of this work. Below I describe the basic principles as they apply to the main thesis, but Appendix A and [22] describe our findings about the technique in more detail.

2.1.1 The Challenge of Nanoscale Capacitive Detection

One perhaps obvious method for detecting the position of a macroscopic object is to monitor the capacitance between it and a nearby electrostatic gate, such as in Fig. 2.1. However, it has long been accepted [23] that this method is unsuitable for nanoscale mechanical resonators due to the tiny capacitances involved. A typical system, for instance, could be comprised of a resonator separated by a distance $d = 100\,\text{nm}$ from a $1\,\mu\text{m}$ gate, both with a 10 nm thick metal layer. In this case, the equilibrium capacitance would be on the order of $C_{NR} = \epsilon A/d \simeq 1\,\text{aF}$, where A is the 10 nm by $1\,\mu\text{m}$ area of overlap between the beam and gate electrodes and ϵ is the permittivity of free space. Nanomechanical resonator displacements are typically less than 1 nm and thus the motional change in capacitance can be expected to be less than 1%. This problem is further compounded by the fact that the coaxial cables used to read out the signal have their own capacitance to ground, on the order of 100 pF for a 1 m length of cable. This capacitance is in parallel with the capacitance between the beam and gate, and thus any change in impedance due to the beam's motion will be masked by the much smaller impedance through the larger cable capacitance.

2.1.2 Voltage-Biased Capacitive Detection

A solution to the above difficulty is shown in the inset to Fig. 2.1. Putting a DC bias voltage V_{NR} between the beam and gate changes the impedance behavior of the system dramatically. The technique described here is well known in

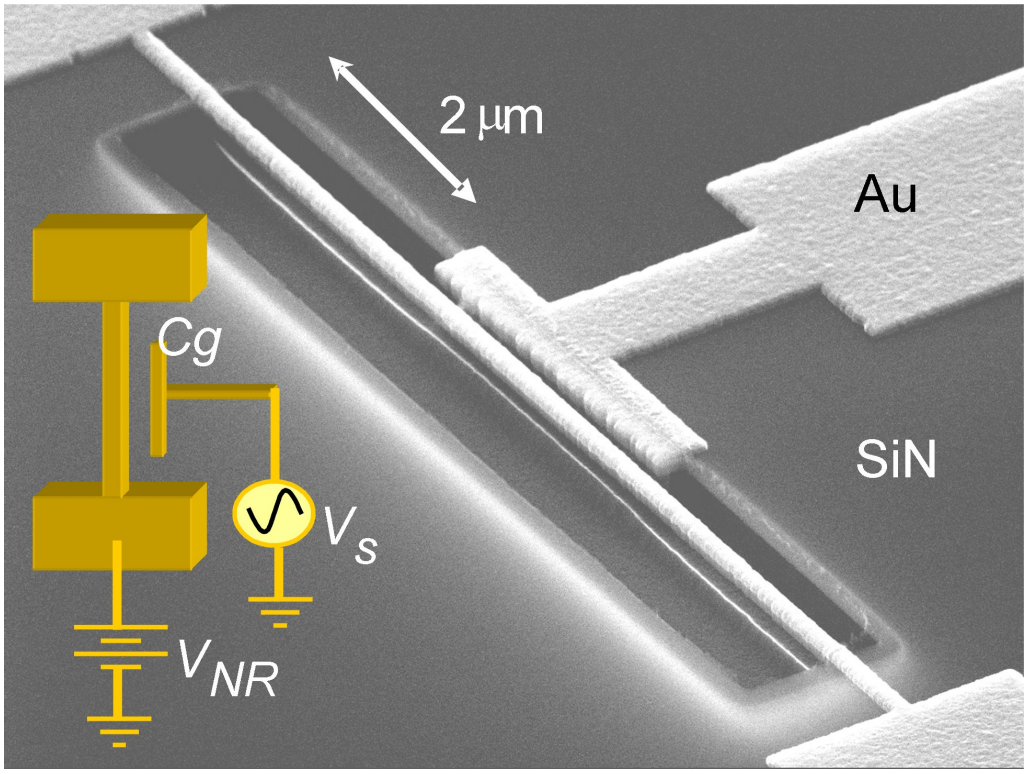

Figure 2.1: SEM micrograph of a metallized resonator with a nearby metallized gate electrode for electrostatic actuation and detection.

the MEMS community and is used in lower frequency microelectromechanical filters [24]. The purpose of this section is to show the applicability of this technique to *nano*electromechanical resonators and to explain the physics behind it.

To derive the appropriate impedance model for this system, we first consider the dependance of the capacitance between the beam and gate on the beam's displacement. The capacitance per unit length is

$$C(x) = \frac{\epsilon A}{d + X} \tag{2.1}$$

For small displacements, i.e. $X/d << 1$ we can write the above as

$$C(X) \simeq C_{NR}\left(1 - \frac{X}{d} + \left(\frac{X}{d}\right)^2 - \cdots\right) \tag{2.2}$$

where C_{NR} is the capacitance when the beam is in its equilibrium position $X = 0$.

Now consider what happens when we apply both a static DC bias voltage, V_{NR}, between the beam and gate as well as a sinusoidal driving voltage V_s with frequency ω. As X increases, the energy of the system changes as

$$\begin{aligned} U(X) &= -\frac{1}{2}C(X)V^2 & (2.3)\\ &= -\frac{1}{2}C_{NR}\left(1 - \frac{X}{d}\right)\left(V_{NR} + V_s\cos\omega t\right)^2 & (2.4)\end{aligned}$$

Using $F = -\mathrm{d}U/\mathrm{d}X$, the force on the resonator is

$$F(t) = -\frac{1}{2}\frac{C_{NR}}{d}\left(V_s^2\cos^2\omega t + 2V_{NR}V_s\cos\omega t + V_{NR}^2\right) \tag{2.5}$$

The third term above is a static force that merely serves to shift the equilibrium position of the resonator slightly. The first term (when expanded) is comprised of another DC force and a force at twice the the applied driving frequency, ω, both of which are small and can be ignored. Thus, the second term is the driving term of interest. Since only the term linear in $\cos\omega t$ is left, we can change to using $e^{i\omega t}$ notation used in Chapter 1, with the usual convention that only the real part is physical. Putting this force into Eq. 1.8, the absolute value of the average displacement of the resonator is seen to follow

$$X_0(\omega) = \frac{\frac{C_{NR}V_{NR}V_s}{dM}}{\omega_0^2 - \omega^2 + i\frac{\omega\omega_0}{Q}} \tag{2.6}$$

To detect the beam's motion, we want to measure the change in impedance due to the motional change in capacitance. To this end, I examine the current flow through the device in response to the applied voltage V_s. Using $q = CV$, and putting the above position response into the expression for the beam-gate capacitance, Eq. 2.2, the charge on the gate is

$$q = C_{NR}\left(V_{NR} + V_s e^{i\omega t}\right) - \frac{C_{NR}V_{NR}X_0(\omega)e^{i\omega t}}{d} \tag{2.7}$$

where once again I have dropped the term at 2ω. Taking the time derivative of Eq. 2.7 and using Eq. 1.8, I find the currents generated in the circuit

$$I = \dot{q} = \left(i\omega C_{NR} - i\omega\frac{C_{NR}^2V_{NR}^2}{Md^2}\frac{1}{\omega_0^2 - \omega^2 + i\frac{\omega\omega_0}{Q}}\right)V_s e^{i\omega t} \tag{2.8}$$

Essentially, the change in time of the capacitance between the beam and gate due to the beam's motion requires that the charge on the gate also change in time to maintain the DC bias $V_G = qC_{NR}$, thus sending currents through the device. Examining Eq. 2.8 in light of $I = V/R$, I find that the impedance of the beam-gate system is made up of two components in parallel, the equilibrium beam-gate capacitance C_{NR}, and a series RLC impedance due to the beam's motion. This nanoresonator effective impedance, referred to as the electromechanical impedance, has equivalent lumped element circuit values given by

$$L_m = \frac{d^2 M}{V_{NR}^2 C_{NR}^2} \tag{2.9}$$

$$C_m = \frac{V_{NR}^2 C_{NR}^2}{\omega_0^2 d^2 M} \tag{2.10}$$

$$R_m = \frac{d^2 M \omega_0}{V_{NR}^2 C_{NR}^2 Q} \tag{2.11}$$

The equivalent circuit model for this system is shown in Fig. 2.2.

The utility of this circuit model lies in the fact that off resonance, the electromechanical impedance is very large due to L_m or C_m, so the total impedance seen at the gate is determined by the much smaller parallel impedance $1/i\omega C_{NR}$. In contrast, on resonance, L_m and C_m cancel, leaving only R_m. For typical nanoresonator parameters ($M = 1 \times 10^{-15}$ kg, $Q = 20,000$, $\omega_0 = 2\pi \times 10^7$ rad/s, $C_{NR} = 50$ aF, $d = 200$ nm and $V_{NR} = 10$ V), the electromechanical impedance is composed of elements $L_m = 160$ H, $C_m = 1.6$ aF and $R_m = 500$ kΩ. Also, $1/\omega_0 C_{NR} \simeq 300$ MΩ. Thus, there is almost a three orders of magnitude decrease in impedance as we go through the resonance, as illustrated in Fig. 2.3.

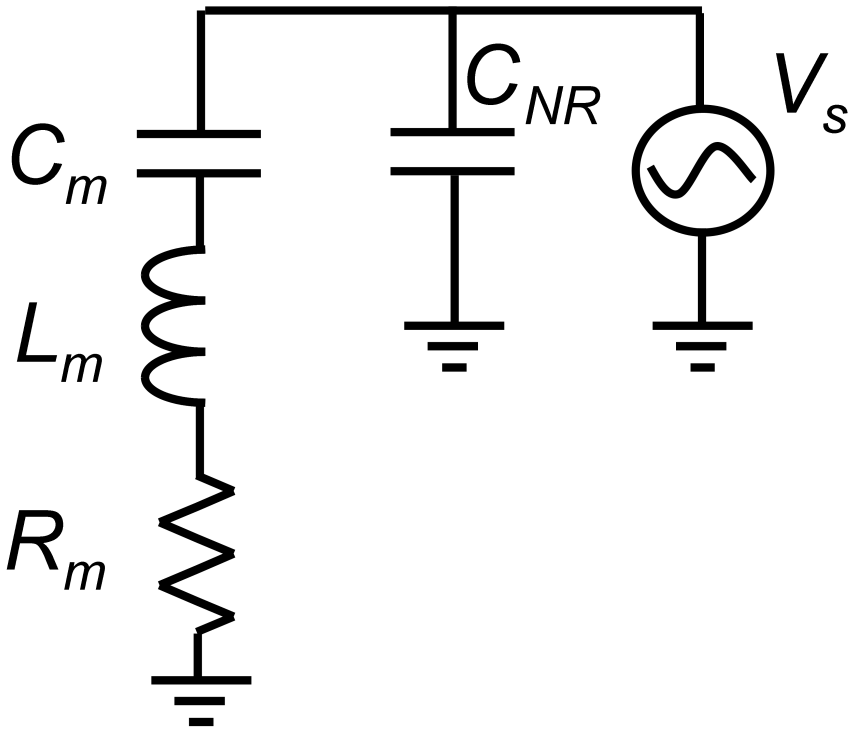

Figure 2.2: Equivalent circuit model for beam and nearby gate, showing the capacitance formed by the beam and gate electrode, C_{NR}, as well as the electromechanical impedance due to the beam's motion.

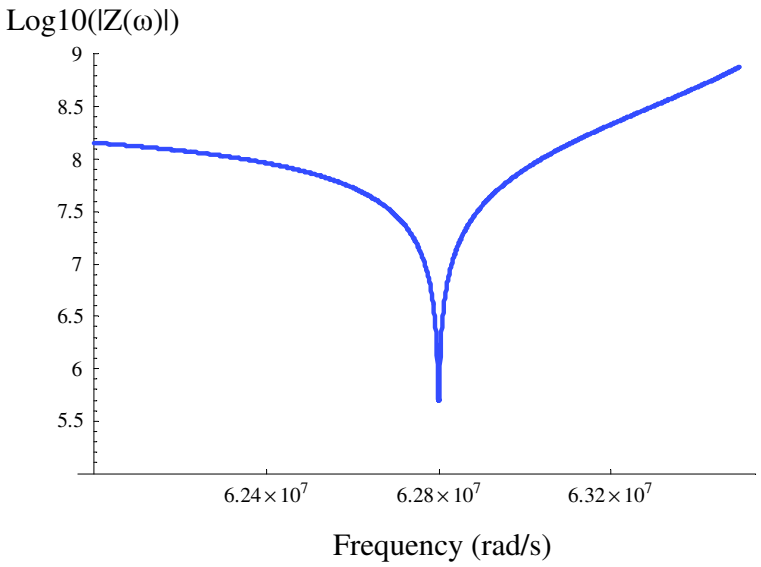

Figure 2.3: Modeled impedance seen at gate coupled capacitively to a nanoresonator (parameters given in text).

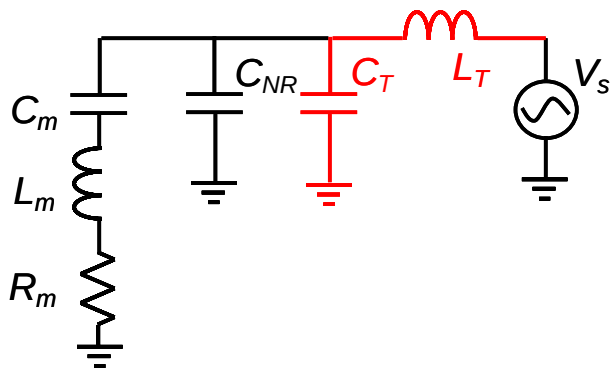

Figure 2.4: Equivalent circuit model including LC tank circuit (in red) used for impedance matching.

2.1.3 Impedance Matching

The impedance on resonance, R_m, is low enough that impedance matching to 50 Ω read-out electronics becomes practical. This matching can be accomplished with a simple LC tank circuit as shown in Fig. 2.4

When the tank circuit resonant frequency, $1/L_T C_T$, and the nanoresonator resonant frequency, ω_0, are equal, then the tank circuit transforms the electromechanical impedance on resonance from R_m to

$$Z_T(\omega_0) = \frac{Z_{LC}^2}{R_m} \tag{2.12}$$

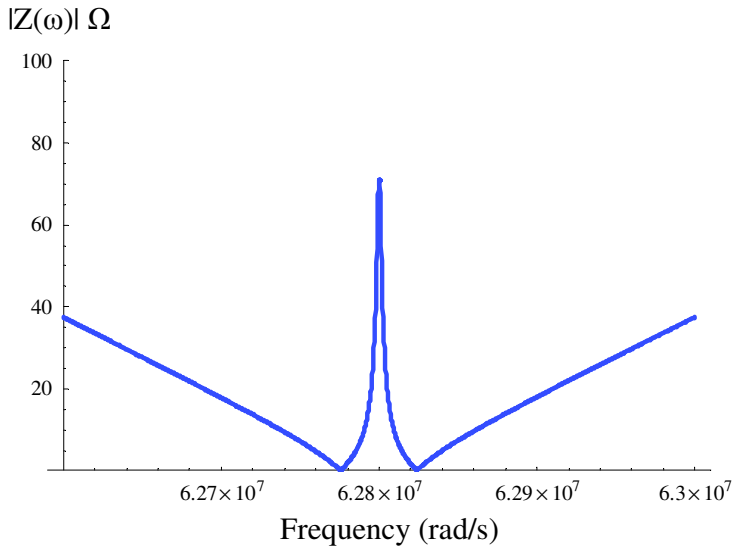

Figure 2.5: Impedance of same system as Fig. 2.3 when coupled to a matching tank circuit.

where $Z_{LC} = \sqrt{\frac{L_T}{C_T}}$ is the characterstic impedance of the tank circuit. For example, with $L_T = 95\,\mu$H and $C_T = 2.7$ pF, the impedance for the system described in the previous section drops to about 70 Ω, as shown in Fig. 2.5. When measuring the impedance with reflectometry, the improved matching greatly increases the contrast between the reflection coefficients on and off resonance.

2.2 Radio-Frequency Single Electron Transistor Detection

The other displacement detector used in this thesis was the RF-SET. This method was used for studying displacement noise in current biased gold coated nanoresonators. As with the capacitive technique, the nanoresonator is capacitively

coupled to the detector, but in this case the detector is a single electron transistor. The technique relies on the near ideal charge sensitivity of the SET [25] to achieve very high displacement sensitivity.

2.2.1 The Single Electron Transistor

The SET consists of a small conducting island connected via tunnel junctions to two external electron baths known as the drain and source. A nearby gate electrode is capacitively coupled to the island for biasing purposes (see Fig. 2.6 for the layout). Charge flow through the device proceeds by sequential tunneling of single electrons when two conditions are met [26]. First, the electrostatic energy cost of putting another electron on the island, known as the charging energy

$$E_C = \frac{e^2}{C_\Sigma} \tag{2.13}$$

must be greater than the bath thermal energy $k_B T$. Here, C_Σ is the sum of the capacitances of the junctions (C_1 and C_2) as well as the capacitances between the island and the gate, C_G, and between the island and the nanoresonator C_{NR}[1]. In contrast to capacitive detection, here the small capacitance between the SET island and the nanoresonator is helpful as we want C_Σ to be small so as to increase the charging energy. To further minimize thermal excitations, we also want the temperature low, and so our experiments were performed with the samples in a dilution

[1] I will use the same variable for parameters such as C_{NR} of V_{NR} that describe coupling between the nanoresonator and the detector, which can be either the gate or the SET. The meaning should be clear from the context.

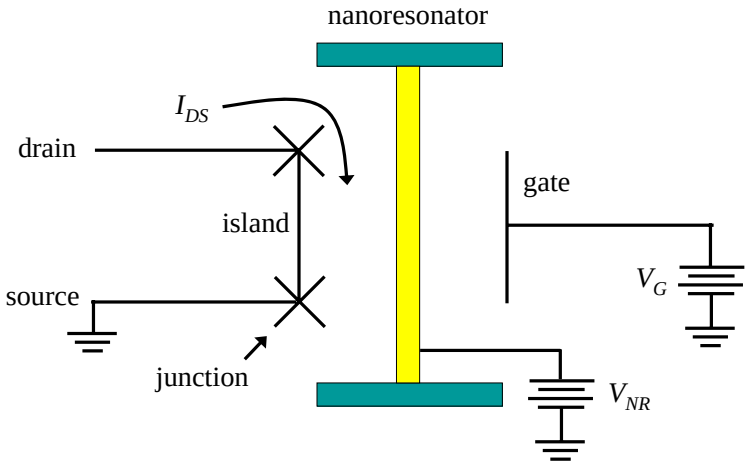

Figure 2.6: Schematic of a nanoresonator coupled to an SET, which consists of a conducting island connected to source and drain electrodes through two tunnel junctions. Motion of the nanoresonator modulates the current I_{DS} through the SET. A nearby gate electrode sets the bias point of the SET.

refigerator with base temperature of approximately 30 mK. The other condition for sequential tunneling is that the resistance through the device be greater than the resistance quantum, $R_q = h/e^2$.

Under these conditions, current flow from drain to source, I_{DS}, is suppressed for small drain-source bias voltages, V_{DS}. With no bias on the gate, current does not begin to flow until V_{DS} is raised high enough to overcome the charging energy, i.e. $V_{DS} > e/C_\Sigma$. The region of suppressed I_{DS}, illustrated in Fig. 2.7(a), is known as the Coulomb blockade.

However, I_{DS} can also be manipulated by application of a voltage, V_G, to the

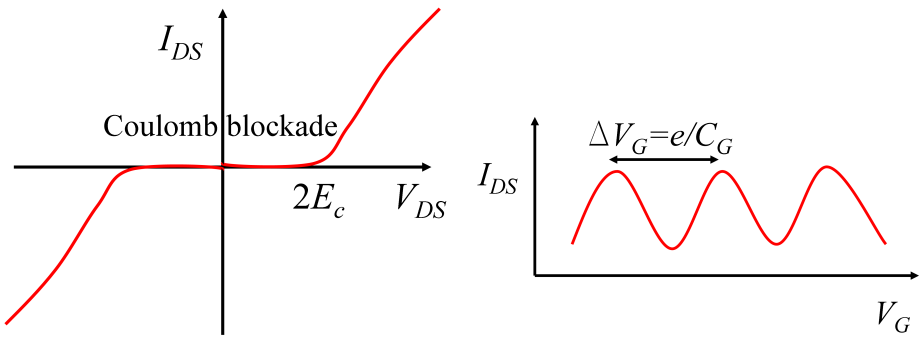

(a) I_{DS} vs. V_{DS} (b) I_{DS} vs. V_G

Figure 2.7: Schematic illustrating the IV characteristics of an SET.

gate electrode. If we increase V_G, we increase the energy level of the state with no additional electrons on the island while decreasing the energy level of the state with one additional electron. The two states are degenerage when the gate voltage corresponds to the charge of one-half an electron, allowing electrons to tunnel and current to flow across the device. As the gate voltage is increased further, the energy levels diverge again until current is stopped at a gate charge of one electron. The cycle then repeats, with the conductance of the SET in the Coulomb blockade region being periodic in V_G with a period of $1e$, as illustrated in Fig. 2.7(b).

2.2.2 The SET as a Position Detector

Once we understand how I_{DS} is modulated by application of a voltage to the gate, we can see how the SET can be used for displacement detection [27, 28]. The nanoresonator is also capacitively coupled to the SET island and acts as a second, *moving* gate electrode. As with capacitive detection, a DC bias voltage, V_{NR}, is kept between the nanoresonator and the detector, the SET. The displacement of the

nanoresonator varies the capacitance, C_{NR}, between them thus varying the charge bias point of the SET through the relation

$$q = C_{NR}(X)\, V_{NR} \tag{2.14}$$

The current through the SET is thus modulated according to [29]

$$\begin{aligned} \frac{\mathrm{d}I_{DS}}{\mathrm{d}X} &= \frac{\mathrm{d}I_{DS}}{\mathrm{d}V_G}\frac{\mathrm{d}V_G}{\mathrm{d}q}\frac{\mathrm{d}q}{\mathrm{d}X} \\ &= \frac{\mathrm{d}I_{DS}}{\mathrm{d}V_G}\frac{1}{C_G}\frac{\mathrm{d}C_{NR}}{\mathrm{d}X}V_{NR} \end{aligned} \tag{2.15}$$

where X is the displacement of the nanoresonator.

2.2.3 The Radio-Frequency Single Electron Transistor

Because the SET has a resistance through both junctions on the order of $100\,\mathrm{k}\Omega$ it suffers from bandwidth limitations due to the $\sim$ 100 pF capacitance in the cables used to bring signal out to room temperature electronics. To be able to read-out nanomechanical resonances on the order of $\sim$ 10 MHz, we use an LC tank circuit, the same as we do with capacitive detection, to transform the impedance of the SET close to 50Ω and operate the device as a radio-frequency single electron transistor (RF-SET) [28, 30]. This transformation allows us to use standard RF reflectometry to measure the SET impedance.

Chapter 3

Fabrication of Devices

In this chapter, I describe the steps taken to fabricate the devices used in the experiments. For the noise measurements, a single electron transistor (SET) was used for transduction and amplification of the mechanical motion. This SET was made out of aluminum and operated below its superconducting transition temperature, making it a superconducting single electron transistor (SSET). However, in order for a bias current through the nanoresonator to generate electromechanical noise, the nanoresonator had to be metallized with a diffusive metal. For these experiments, we used a gold coating on the nanoresonator. Thus, the nanoresonator and SSET had to be fabricated in separate lithography steps.

In contrast, the dissipation measurements utilized an aluminum coated resonator capacitively coupled to a nearby aluminum gate electrode, allowing both the nanoresonator and detection device to be fabricated in a single lithography step.

3.1 The Wafer

The wafer used for fabrication consisted of a silicon substrate coated with 50 nm of low-stress silicon nitride Si_3N_4. These wafers were provided by *NEMS Exchange* [31], who also fabricated the bond pads and tank circuits using the design shown in Fig. 3.1. In house fabrication was performed in the 100 μm x 100 μm

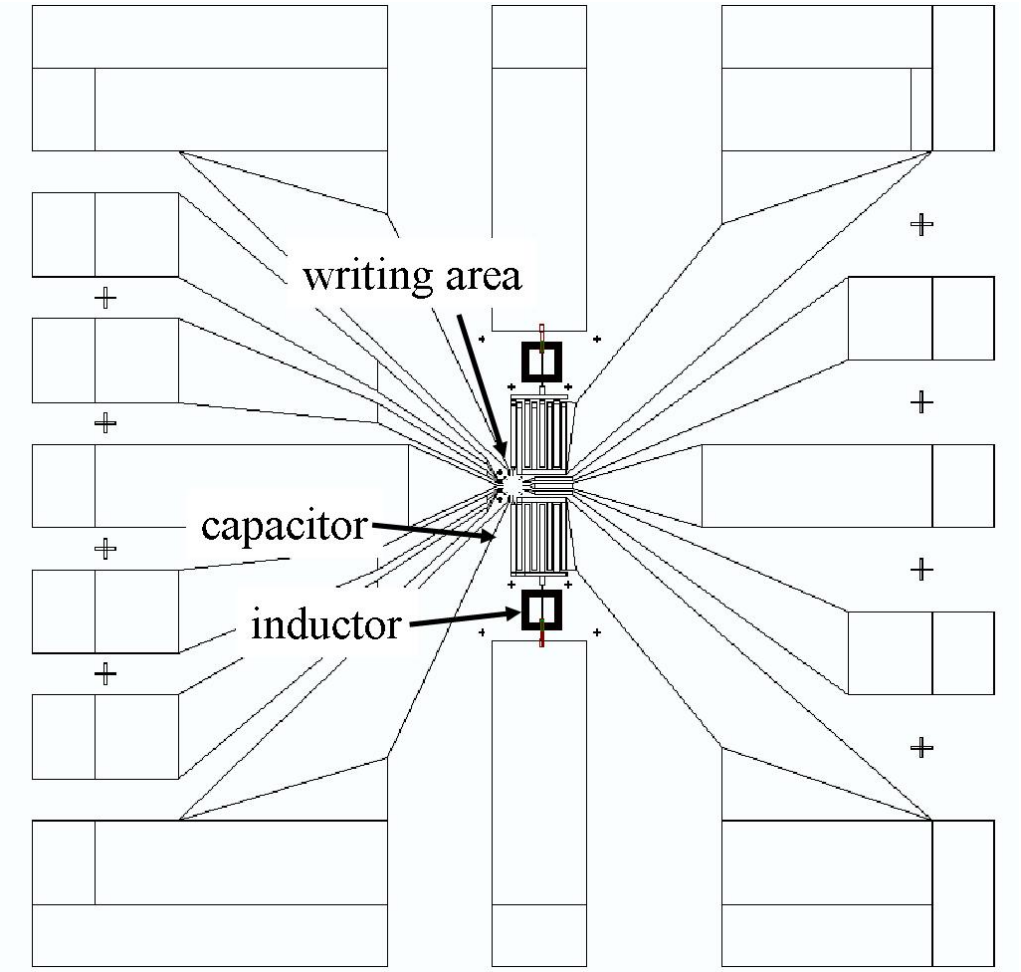

Figure 3.1: Design of individual sample die as provided by *NEMS Exchange*, showing the bond pads for connection to external circuitry as well as the coil inductor and interdigitated capacitor that make up the tank circuit for the RF-SET. The size of each sample is about 4 mm by 4 mm.

square writing area between the two tank circuits. The two tank circuits mean that each die can accomodate two samples, which we usually fabricate as sharing a common gate electrode.

3.2 Defining the Nanomechanical Resonator

After receiving the diced wavers from *NEMS Exchange*, each sample for the noise measurements was fabricated in three lithography steps. The first step was to deposit the gold layer that defines the width and length of the nanoresonator. The gold layer serves as a mask for when the nanoresonator is eventually freed from the substrate (which does not occur until the last step, seeing as the nanoresonator is the most fragile part of the sample). It also serves as the region through which the bias current is sent to generate electromechanical noise and it is used to capacitively couple the nanoresonator to the SET. A bilayer of e-beam resists (methacrylic acid (MMA) and polymethyl methacrylate (PMMA)) is used to facilitate lift-off. The steps for this part of the fabrication were as follows:

- The sample is cleaned by immersion in hot acetone. It is then further cleaned with methanol and isoprobyl alcohol (IPA) and then blow dried with nitrogen gas N_2.

- The sample is then coated with a bilayer of e-beam resist used for pattern writing in the scanning electron microscope (SEM). First, we spin copolymer MMA:EL Thinner (1:1) at 3000 RPM for 1 minute. The sample is then baked on a hot plate at 200° C for 5 minutes to cure the resist. The next layer, 950K PMMA A-4, is spun at 5000 RPM for 1 minute and the sample is again baked at 180° C for 1 minute.

- The sample is inserted into the SEM and exposed with the pattern shown in

Fig. 3.2 (detail in Fig. 3.3). Note that though the figure shows the complete drawing pattern, only the nanoresonator, gate and associated leads are exposed in this step. The dose was 380 μC/cm^2 for the resonator and 450 μC/cm^2 for the leads and gate. The pattern is designed to give the nanoresonator a nominal length and width of $l = 10\,\mu$m and $w = 170\,$nm, respectively. The gate electrode has a nominal length of $l_G = 2\,\mu$m. Also, the gap between the nanoresonator and the gate is approximately $d_G = 1300\,$nm.

- The resist is then developed by immersing the sample in MIBK (Methyl Iso Butyl Ketone):IPA (1:3) for 40 seconds and then rinsing it in IPA for 40 seconds followed by blow drying with N_2. The sample is then put in an RIE for 10 s of reactive ion etching with oxygen plasma to remove any residual resist from the exposed areas.

- The metallic layer is then deposited using electron beam evaporation. A 20 nm titanium adhesion layer is followed by 130 nm of gold.

- The remaining (non-exposed) resist is lifted off by immersion in hot acetone, leaving the deposited metal in only the exposed areas.

3.3 Fabrication of the SET

The second lithography step is the fabrication of the single electron transistor and associated leads. An SET is comprised of two tunnel junctions connected to a central conducting island. In our case, the tunnel junctions are formed by

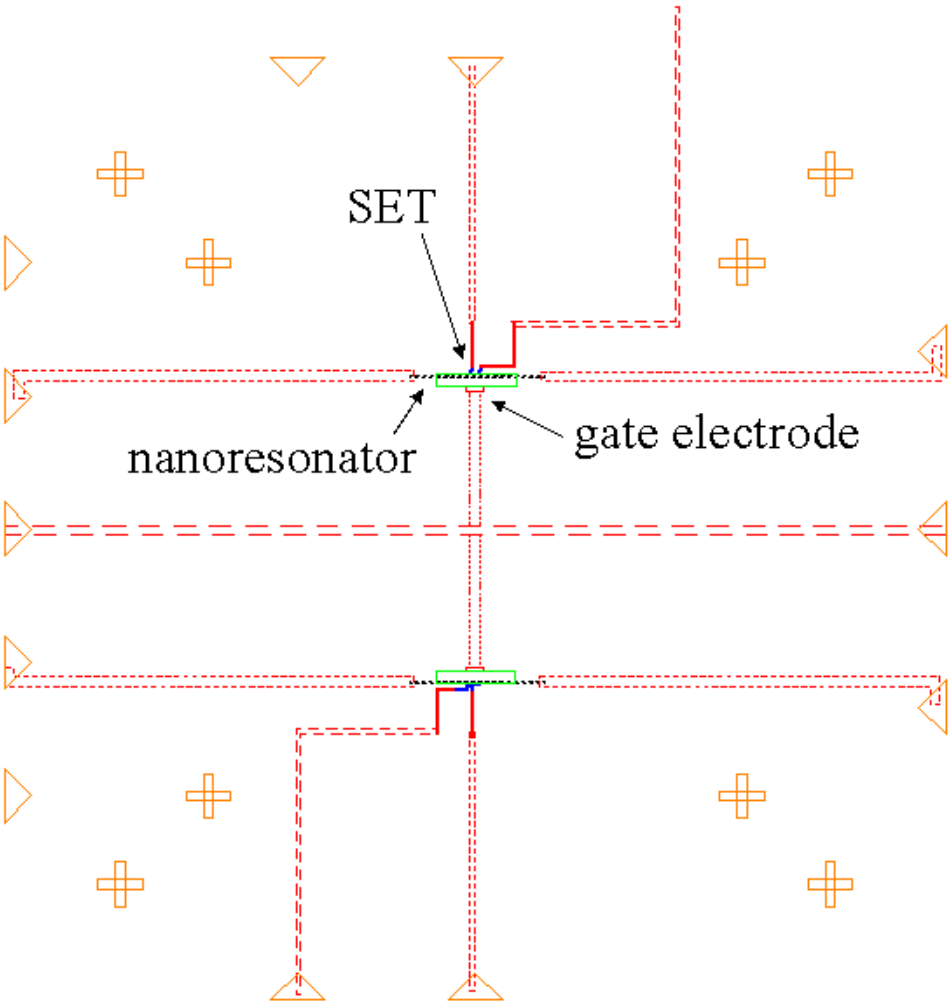

Figure 3.2: SEM pattern showing the position of the nanoresonator, SET and gate electrode. Detail is shown in Fig. 3.3.

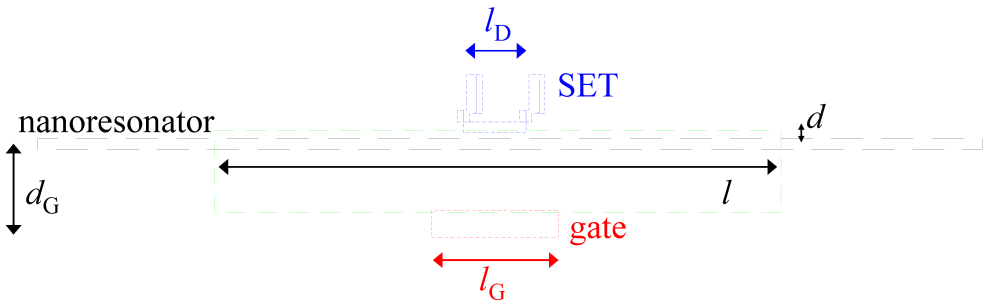

Figure 3.3: Detail of SEM drawing pattern around the nanoresonator and SET. The green window is the etch area for undercutting the beam.

overlapping aluminum leads separated by a thin layer of aluminum oxide. Fabrication of the junctions is accomplished through the technique known as double-angle evaporation [32, 33]. The complete recipe is as follows:

- The sample is cleaned of any residue from the previous step using acetone, methanol and IPA and then blow dried with N_2.

- E-beam resist, MMA 8.5:EL (1:1), is spun at 4000 RPM for 1 minute. The second layer is 950K PMMA A-4 spun at 5000 RPM for 1 minute. A 5 minute bake at 180° C follows each spin.

- In the SEM, the pattern for the SET and its leads shown in Fig. 3.2 and 3.3 is exposed. The leads to the bond pads and island are exposed with 450 μC/cm^2 and 350 μC/cm^2, respectively. The junction leads are exposed with a 1.4 nC/cm line dose and a 180 μC/cm^2 area dose to form an undercut used for the double-angle evaporation. The island is fabricated a distance $d = 300\,\text{nm}$ away from the beam and has length $l_D = 1\,\mu\text{m}$.

- The sample is developed in MIBK:IPA (1:3) for 1 minute, rinsed in IPA for 30 seconds and then blow dried in N_2. Any resist left in the exposed areas is removed with a 12 s RIE oxygen plasma etch.

- Deposition of the aluminum for the SET is performed in a thermal evaporator with a rotatable sample stage. The process is described below and illustrated in Fig. 3.4.

  – With sample at +10° to aluminum source, deposit 35 nm of aluminum

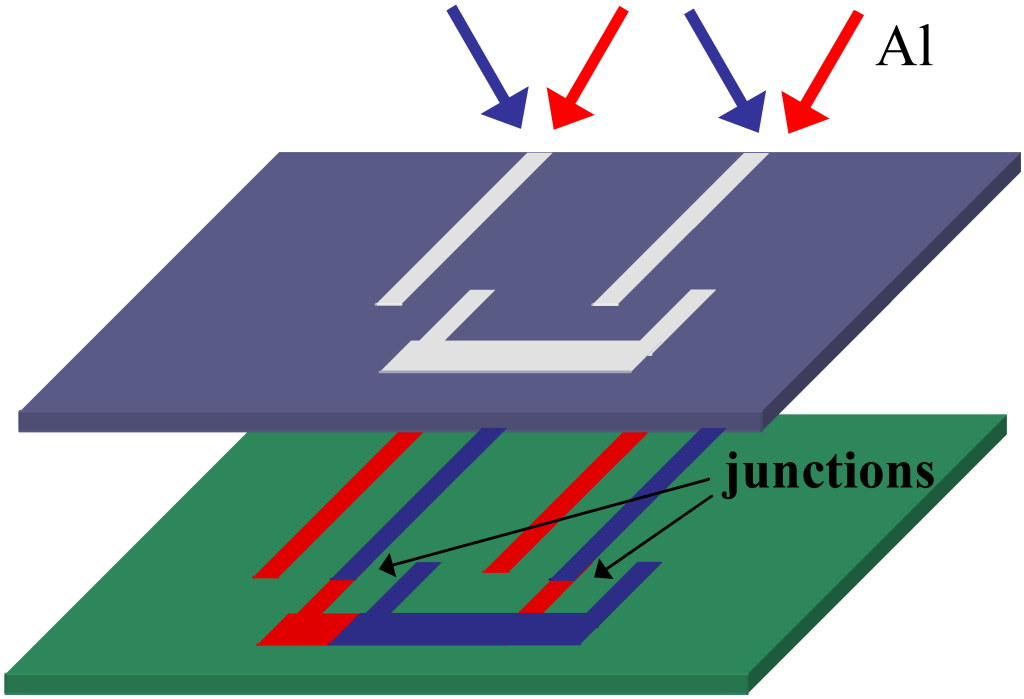

Figure 3.4: Illustration of double-angle evaporation. The green layer represents the Si_3N_4 that the SET is formed on. The purple layer is the resist with the exposed pattern and has been offset vertically for clarity. Two separate evaporations (red and blue) of aluminum are done at complementary angles so as to offset the pattern from one evaporation to the next. An intermediate oxidation step creates the tunnel barrier where the leads overlap.

at 0.5 nm/s.

  - Introduce oxygen O_2 at about 80 mTorr for approximately 2 minutes. This step produces an aluminum oxide tunnel barrier on the order of 1 nm.

  - Change sample orientation to -10° and deposit another 90 nm of aluminum.

- The rest of the resist is lifted-off in hot acetone.

3.4 Freeing the Nanoresonator

The final step is to free the nanoresonator into a freestanding structure. To do this, we used a dry undercut etch technique [13, 34, 35]. The advantage of using a dry etch over a wet etch is that we do not have to worry about surface tension snapping the beam. The steps are described below:

- The sample is cleaned again with acetone, methanol and IPA and blow dried with N_2.
- A single layer of PMMA 950K A7 is spun at 4000 RPM for 1 minute. The resist is then cured by baking the sample on a hot plate for 5 minutes at 180° C.
- In the SEM, we expose an etch window around the nanoresonator using a 400 $\mu C/cm^2$ dose.
- The sample is developed in MIBK:IPA (1:3) for 1 minute, rinsed in IPA for 30 seconds, and blow dried with N_2.
- Finally, we undercut the nanoresonator in the RIE. The steps, illustrated in Fig. 3.5, are listed below:
  - Etch in CHF_3 plasma for 2 minutes. This etch is anisotropic and removes the nitride one either side of the resonator, exposing the silicon underneath.

dimension	symbol	size (nm)
beam length	l	10000
beam width	w	170
thickness of Si_3N_4	t_{SiN}	500
thickness of Ti	t_{Ti}	20
thickness of Au	t_{Au}	130
gate length	l_G	2000
SET island length	l_D	1000
beam-gate distance	d_G	1300
beam-SET distance	d	300

Table 3.1: Relevant dimensions for noise measurement devices.

- Next, etch with SF_6, an isotropic silicon etch that etches underneath the beam and frees it from the substrate.
- Lastly, use oxygen plasma for approximately 3 minutes to remove the rest of the resist (optional).

From SEM observations of the area underneath the beam, we know that it is probable that a thin ridge of Si hangs underneath the beam. Figure 3.6 shows a closeup of a completed resonator + SET device. The important dimensions are summarized in Tab. 3.1.

3.5 Devices for Dissipation Measurements

The devices used for dissipation measurements were fabricated in a similar manner, except that they are optimized for capacitive detection and the nanoresonator is coated with aluminum rather than gold. The gate electrode is longer and positioned closer to the nanoresonator (100 nm) and since they are both made of aluminum they are both made in the same lithography step. The aluminum was

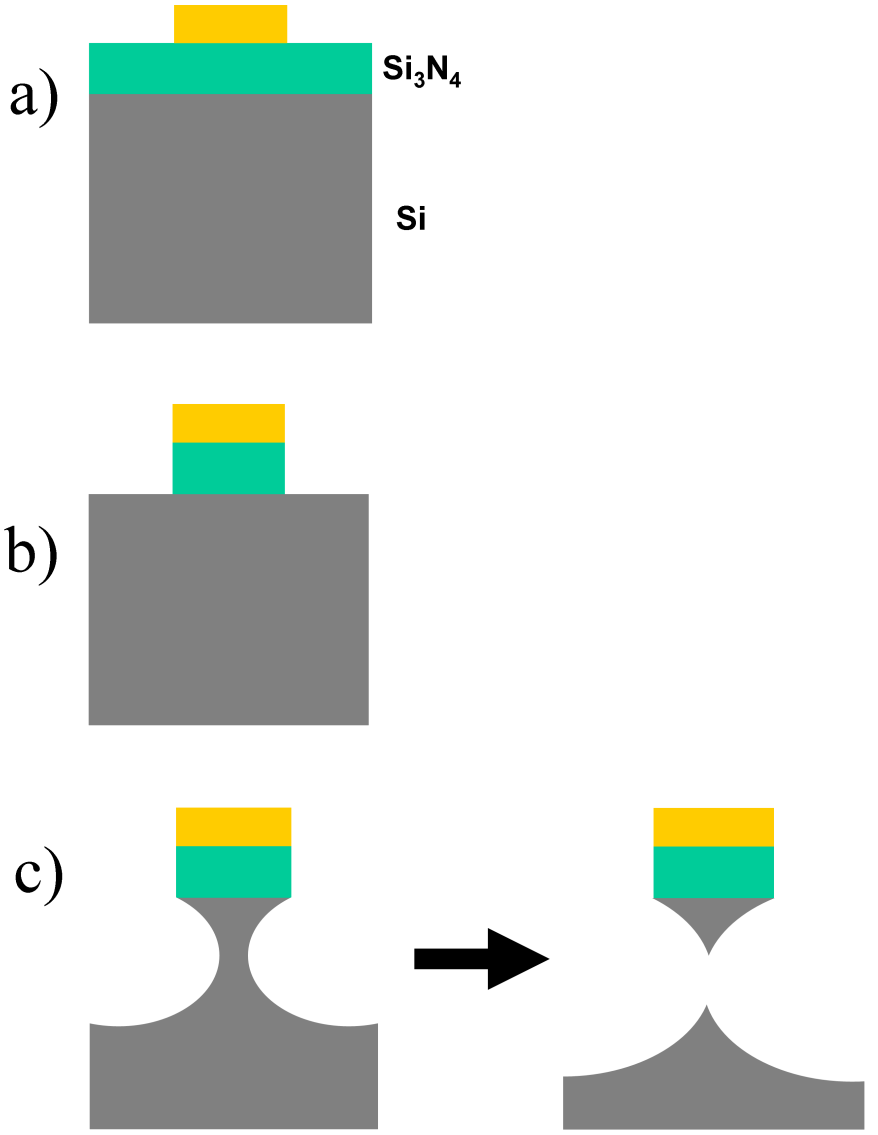

Figure 3.5: The undercut etch method for freeing the nanoresonator. a) Cross sectional view of nanoresonator mask (gold) on top of Si_3N_4 and Si substrate. Unshown areas to the left and right are covered in resist and are not etched. b) Anisotropic etch of Si_3N_4 to expose substrate. c) Isotropic etch of Si to free the nanoresonator.

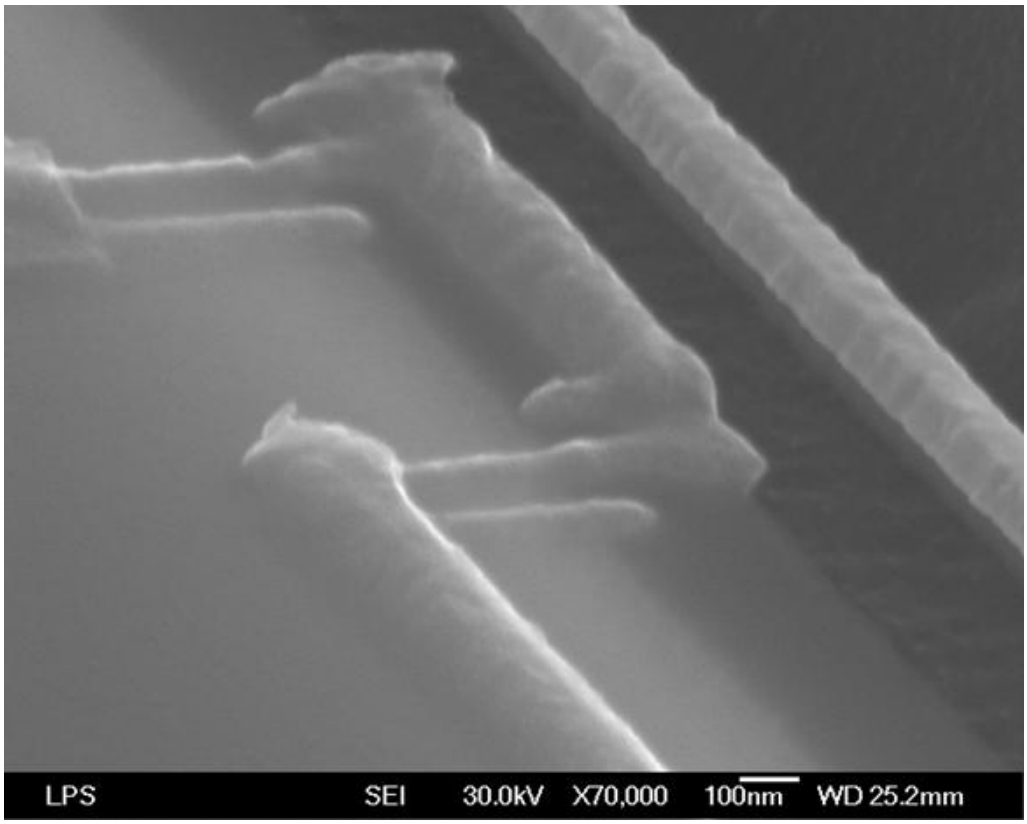

Figure 3.6: SEM photo showing closeup of SET with nearby resonator.

dimension	symbol	size (nm)
beam length	l	20000
beam width	w	200
thickness of Si_3N_4	t_{SiN}	500
thickness of Al	t_{Au}	130
gate length	l_D	12000
beam-gate distance	d	300

Table 3.2: Relevant dimensions for dissipation measurement devices.

deposited in a double-angle evaporation step, however, since these devices do have SET's (which are not utilized here). The dimensions are summarized in Tab. 3.2.

Chapter 4

Methods

This chapter describes in more detail the operation of the RF-SET and the capacitive detection circuit. I also describe the measurements used to extract the nanoresonator parameters.

Experiments were performed with the samples thermally anchored to the mixing chamber stage of a Oxford Kelvinox 400 dilution refigerator. We were able to obtain a base temperature of approximately 30 mK, as measured by a RuO resistance thermometer. The refigerator is mounted on an optical table with vibration isolation and sits in a copper shielded room to shield from stray RF. The following sections describe the operation of the position detection circuits.

4.1 Operation of the RF-SET

This section details how we operate the RF-SET for measurement of spectra due to nanomechanical motion. Figure 4.1 provides a color-coded reference to the various parts of the measurement circuit.

4.1.1 Reflectometry Circuit (Black/Solid Lines)

The impedance of the SET is measured through RF reflectometry. A 1 GHz carrier signal is sent down to the device through a directional coupler. The reflection

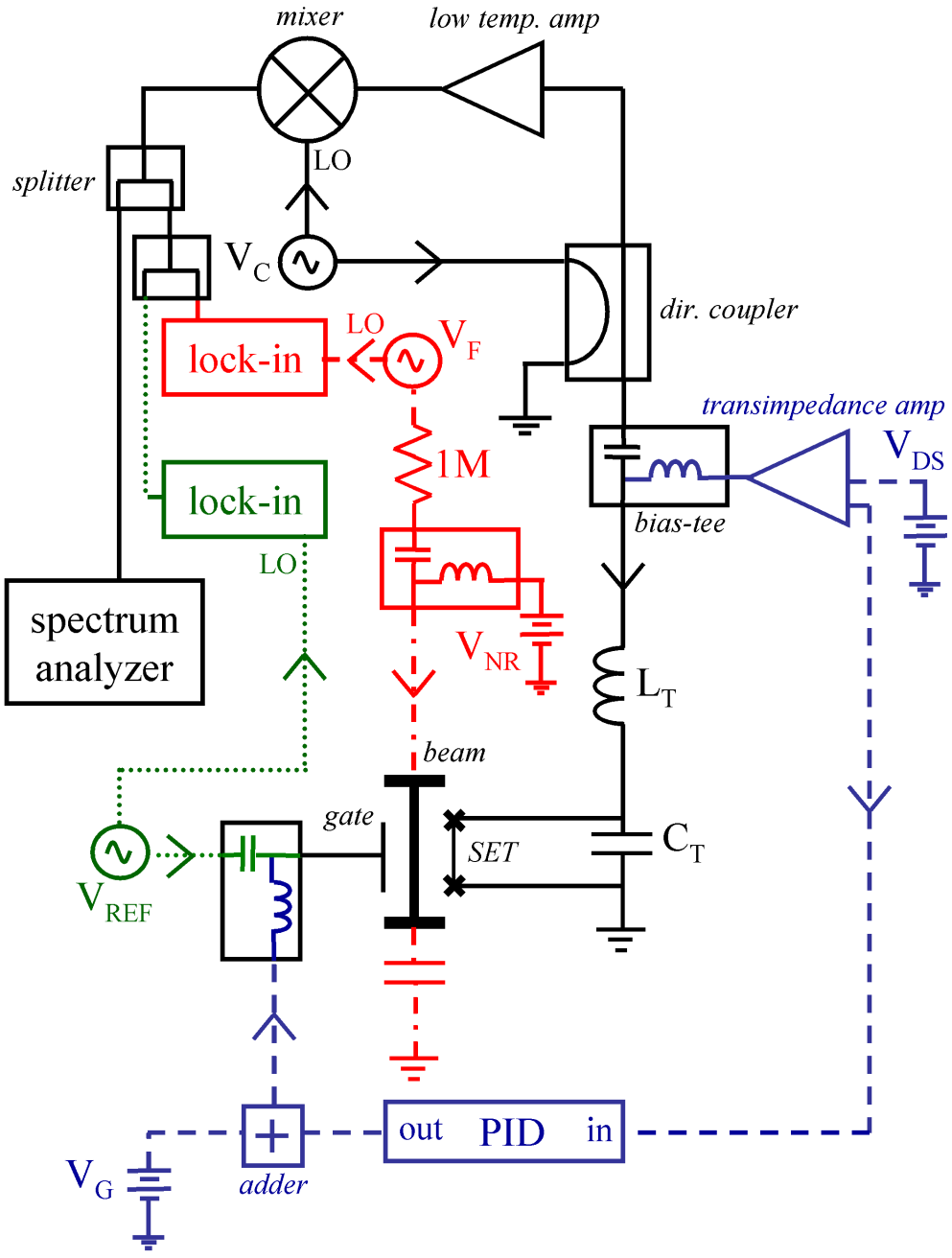

Figure 4.1: Circuit for RF-SET measurements of charge noise due to current-induced position fluctuations of a nanoresonator. The diagram is color coded to match the description of each part of the circuit in the text.

coefficient of the return signal is given by

$$\Gamma = \frac{R_S - R_0}{R_S + R_0} \tag{4.1}$$

where R_S is the resistance presented by the SET and tank circuit and R_0 is the impedance of the radio frequency source ($50\,\Omega$). The reflected signal is amplified by both a low temperature amplifier [36] and a room temperature amplifier [37].

As discussed in Chapter 2, I_{DS} is dependant on both V_{DS} and the charges on the gate and the beam. The SET impedance is modulated at the frequency of these signals, resulting in sidebands in the reflected power from the 1 GHz carrier. We mix the reflected signal with the original carrier to recover these sidebands (homodyne detection). The signal is split, with half the power going to lock-in amplifiers for monitoring the signals applied to the gate (see below) and half going to a spectrum analyzer (see Fig. 4.2) to observe the full bandwidth response of the SET to the nanoresonator's motion.

4.1.2 SET Biasing Circuit (Blue/Dashed Lines)

The gate bias, V_G, and the drain-source voltage, V_{DS}, are both controlled by a DAQ card connected to a PC. The overall charge bias seen by the SET can vary with time due to motion of charges in the sample substrate. To compensate for this a feedback scheme is implemented. The current through the SET, I_{DS}, is monitored with a transimpedance amplifier with the voltage output sent to a PID controller. The PID then adds a small correction to V_G in order to keep I_{DS} at a constant set

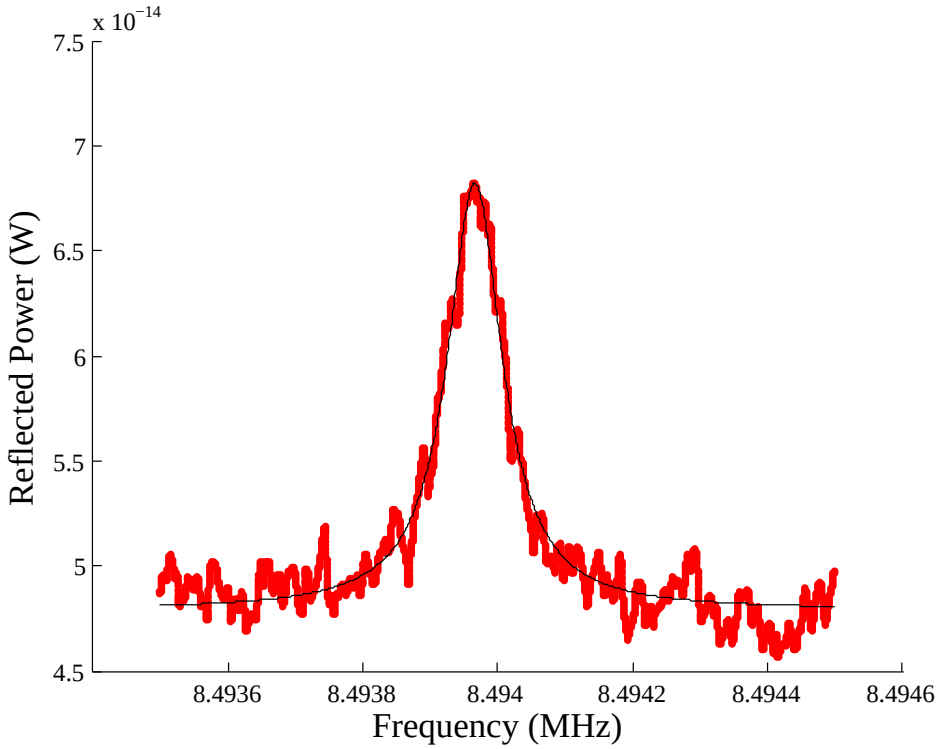

Figure 4.2: Example of reflected power from RF-SET due to nanoresonator's motion as measured by the spectrum analyzer. Fit is Lorentzian. Data is thermal noise from sample 2 at 100 mK.

value. Generally, the bias is set to a point of high current modulation, $\mathrm{d}I_{DS}/\mathrm{d}V_G$ in order to maximize the gain.

4.1.3 Charge Reference (Green/Dotted Lines)

In order to compare different mechanical spectra, a small AC voltage, V_{REF}, is sent to the gate for charge gain calibration near the resonant frequency of the mechanics. During a measurement, the sideband signal from the SET at this frequency is monitored by an RF lock-in amplifier and the spectra are scaled by the average gain.

It is useful to be able to know the charge signal on the gate due to the reference signal. With a DC bias corresponding to an integer number of electrons on the gate, the power in the sideband of the reflected response is approximately [38]

$$P = P_0 \sin\left(2\pi\Delta Q_G \sin\omega t\right) \tag{4.2}$$

where ΔQ_G is the AC charge signal sent to the gate. Since this function is a sine of a sine, it can be expanded as a series of Bessel functions

$$P = 2P_0 \sum_{n=0}^{\infty} J_{2n+1}\left(2\pi\Delta Q_G\right) \sin((2n+1)\omega t) \tag{4.3}$$

We sweep the amplitude of V_{REF} (proportional to ΔQ_G) and fit the amplitude of the response to a first-order bessel function as in Fig. 4.3. From the first zero of the fit we are then able to determine what voltage at the source corresponds to $1e$

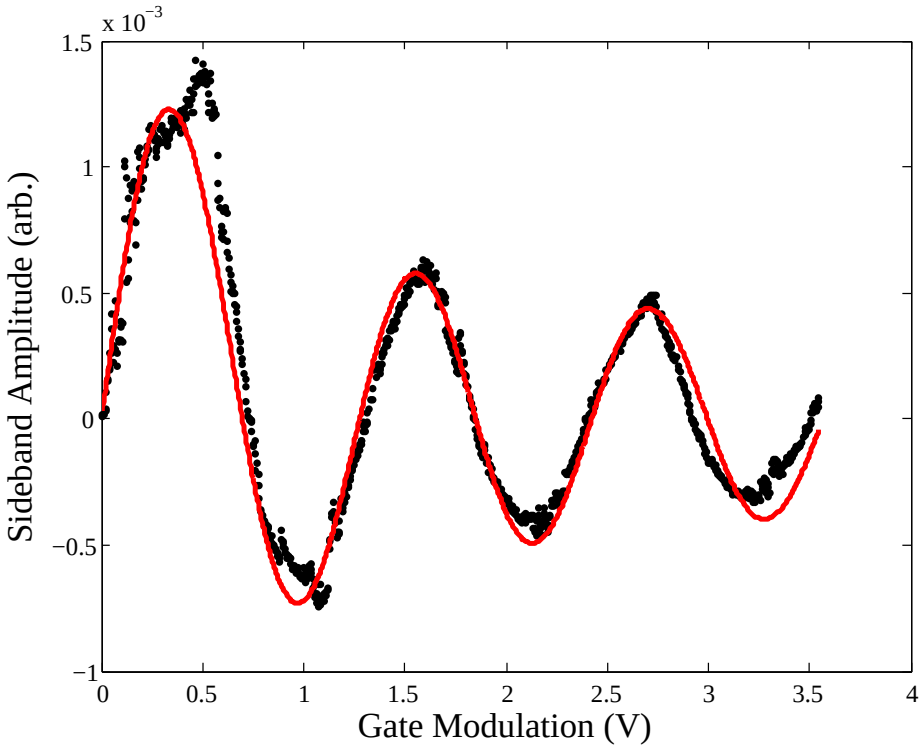

Figure 4.3: Example of Bessel fit for reference charge calibration. Data is for sample 3 with gate modulation at 10.5 MHz.

at the gate.

To reduce the effect of noise from the RF source, we sent a larger V_{REF} than needed and attenuated it where the signal entered the dilution refigerator. The result of the bessel fit can be compared with $Q_G = C_G V_G$ to find the attenuation in the lines from the voltage source to the gate. Figure 4.4 shows the results of charge calibration measurements at several frequencies for Sample 3, where the added attenuation has been subtracted, leaving only the attenuation in the line. Measurements performed for Samples 1 and 2 were within 2 dB of these values.

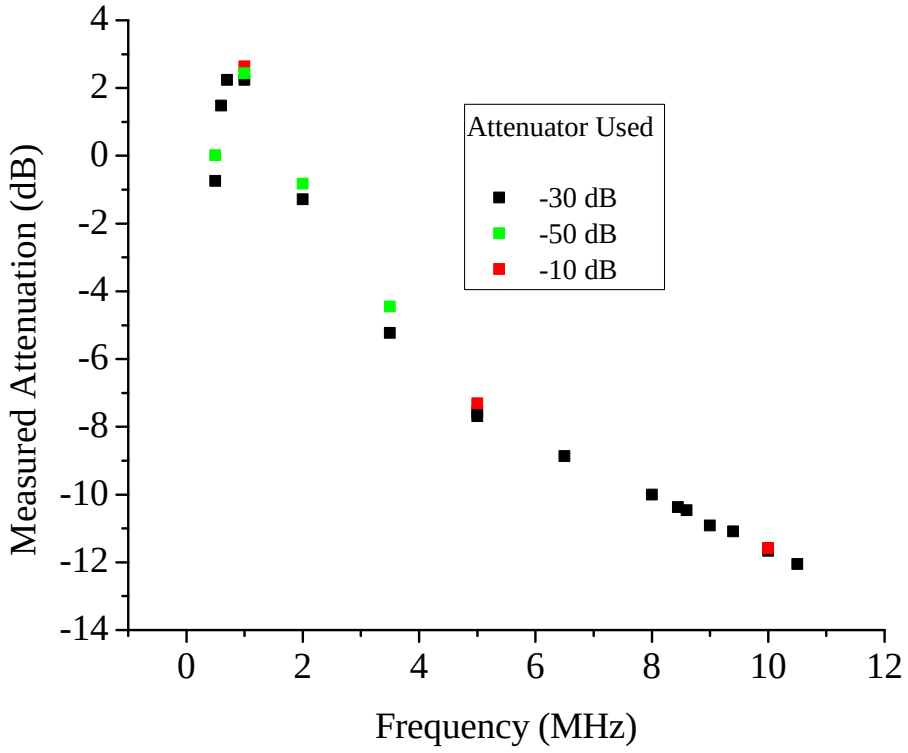

Figure 4.4: Gate line attenuation vs. frequency measured with sample 3. Each data set has been offset by the attenuator value used where the signal enters the fridge, so the data here shows the attenuation in the coaxial lines only.

4.1.4 Beam Current (Red/Dot-Dashed Lines)

For the noise measurements, we need not only a way to measure the displacement noise of the nanoresonator, but also a way to send current through the beam to generate the noise. We already have a DC voltage on the nanoresonator, V_{NR}, for coupling to the SET, but this is of the order of several volts and if the beam was grounded would produce currents that were much to high. So to generate the noise, we use a 1 MHz AC current, I_F, generated via an RF voltage source with a $1\,\mathrm{M}\Omega$ resistor in series. Both V_{NR} and I_F are coupled to the nanoresonator through a bias-tee on top of the dilution refigerator. On the other side of the beam is a blocking-capacitor, that was tested at low temperatures and has a capacitance of about 400 nF. This blocking capacitor acts as a short for the noise generating current, but keeps the coupling voltage V_{NR} from dropping across the device.

To know how much current is sent through the nanoresonator, I first measured the attenuation from the voltage source to the point where the signal passes through the $1\,\mathrm{M}\Omega$ resistor and found -3.35 dB of attenuation. Before going into the fridge, the signal passes through the bias-tee shown in Fig. 4.1 as well as a 2.5 MHz low-pass filter. The insertion loss through these components was measured to be less than 0.2 dB. Finally, the signal is carried on a low frequency line in the dilution refigerator. The attenuation at room temperature through this line at 1 MHz was measured to be about -8 dB. However, this attenuation can be attributed to the $150\,\Omega$ of DC resistance through the line, which includes an RF stripline for thermalization. I can model the impedance of the line with a lumped-element circuit model as shown in

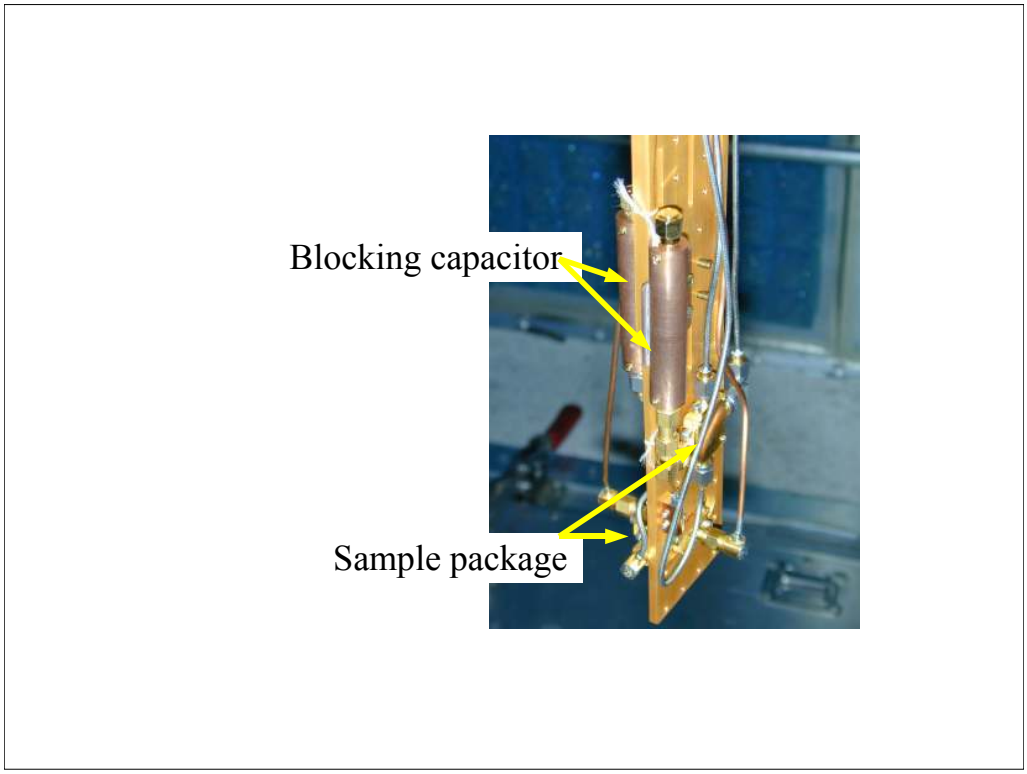

Figure 4.5: Two RF-SET based devices mounted on the dilution refigerator sample stage. The blocking capacitors used for the beam bias current are also shown..

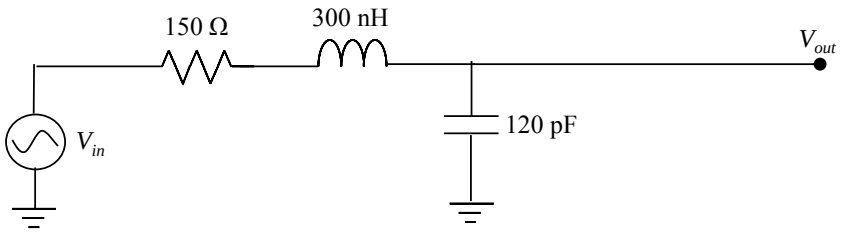

Figure 4.6: Lumped-element circuit model for the line that carries current down the to beam.

Fig. 4.6, where the 120 pF cable capacitance is chosen to fit the data and agrees with the expected 30 pF/ft for stainless steel coaxial lines [39]. The inductance in the model is chosen to give a characteristic impedance of 50 Ω.

The measured and modeled attenuation is shown in Fig. 4.7. With the beam resistance being on the order of 30 Ω (see below), the cable capacitance of 120 pF can be expected to shunt less than 5% of the current coming in at the top of the fridge at 1 MHz.

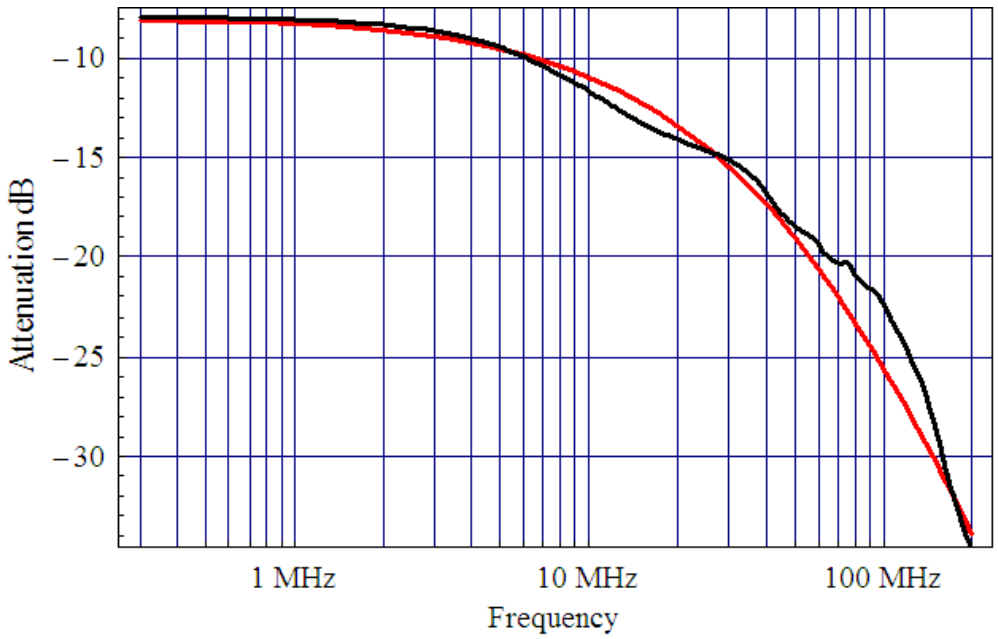

Figure 4.7: Measured (black) and modeled (red) attenuation in beam line. Measured data is at room temperature.

4.1.5 Measuring the Gate and Nanoresonator Capacitances

To find the capacitances between the gate or nanoresonator and the SET, we sweep the voltage on either electrode and monitor I_{DS}, as shown in Fig. 4.8. Since the current through the SET varies with the charge bias with a periodicity of $1e$, we can find the capacitances through the relation $e = C\Delta V$, where ΔV is the periodicity of I_{DS} with respect to the applied voltage.

4.1.6 I-V Curves, Charging Energy and Gain

The I-V characteristics of the SET are measured by sweeping both V_{DS} and V_G with a PC controlled DAQ card and measuring I_{DS} with the transimpedance amplifier. This data can be used to build up a conductance map such as shown in Fig. 4.9.

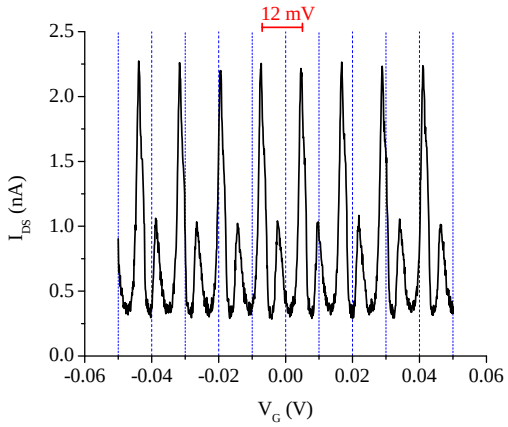

(a) a

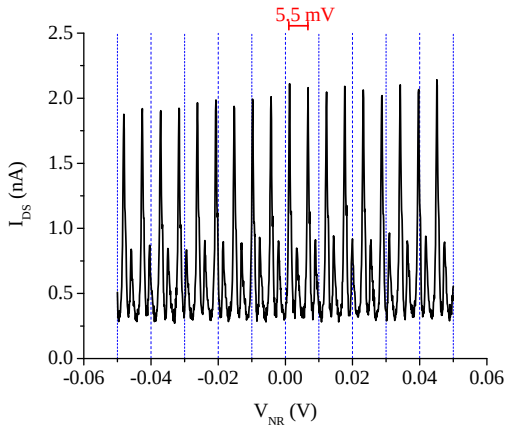

(b) b

Figure 4.8: I_{DS} versus (a) gate and (b) nanoresonator voltages. Data from sample 1.

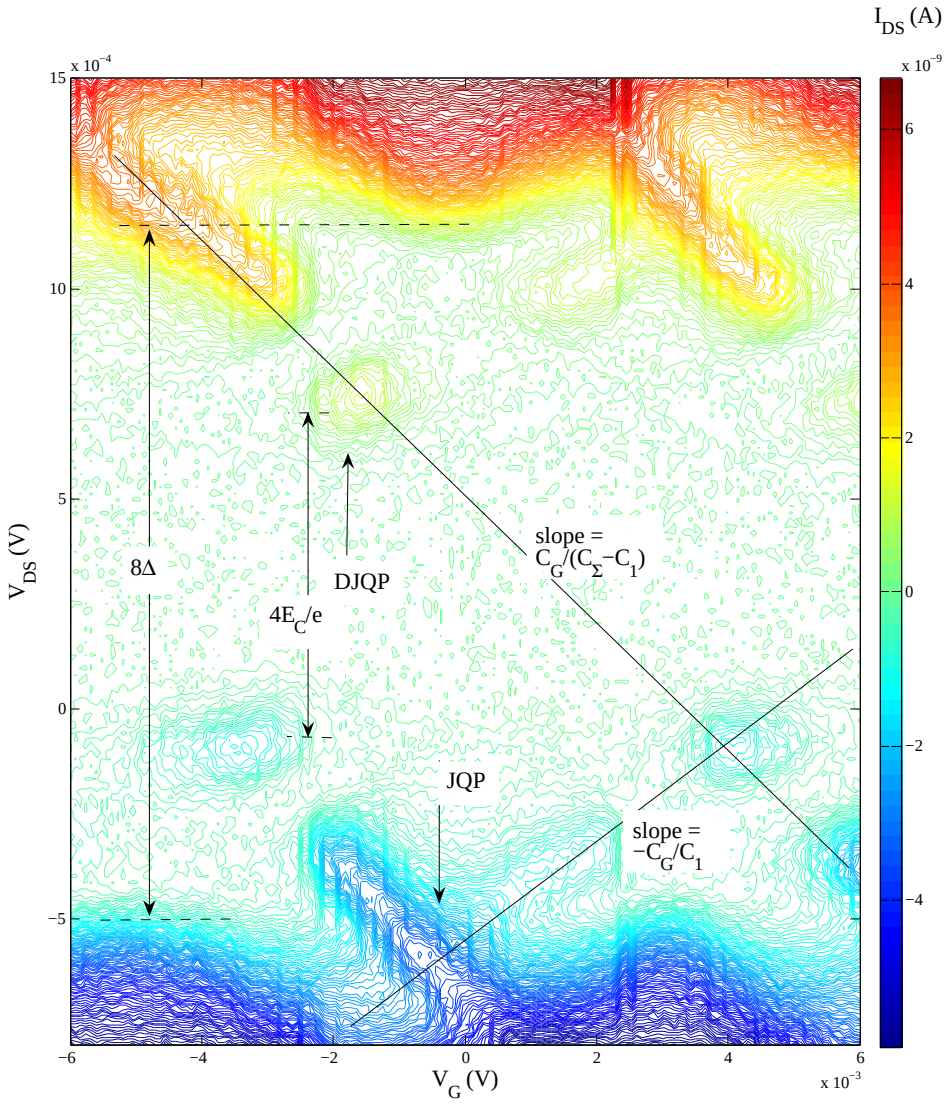

Figure 4.9: Conductance map of SET. Data is from sample 2.

	Sample 1	Sample 2	Sample 3
C_{NR} (aF)	29	31.2	30
C_G (aF)	13.4	19.5	17.8
C_1 (aF)	114	131	234
C_2 (aF)	165	187	259
E_C/k_B (K)	2.89	2.52	1.72

Table 4.1: Sample capacitances and charging energies.

Because our SET's are made out of aluminum, there are additional features in the conductance map due to their superconducting nature. The plateau due to the Coulomb blockade is widened by 8Δ, where Δ is the superconducting gap energy. There are also higher order tunneling processes known as the Josephson Quasiparticle (JQP) and Double Josephson Quasiparticle (DJQP) resonances [40].

These quasiparticle resonances can be used to determine the charging energy of the SET. The DJQP resonances are separated by $4E_C/e$ while the JQP resonances are separated by $8E_C/e$. Alternatively, we can use the slopes of the quasiparticle ridges to determine the junction capacitances, C_1 and C_2, as shown in Fig. 4.9 and calculate the charging energy from Eq. 2.13.

While collecting the data for the conductance map, we also monitor the power in the sideband due to the gate reference signal. Thus, we also have a measure of the gain as a function of V_G and V_{DS}. The gain map is shown in Fig. 4.10.

The capacitances and charging energies of the three SET based devices are summarized in Table 4.1.

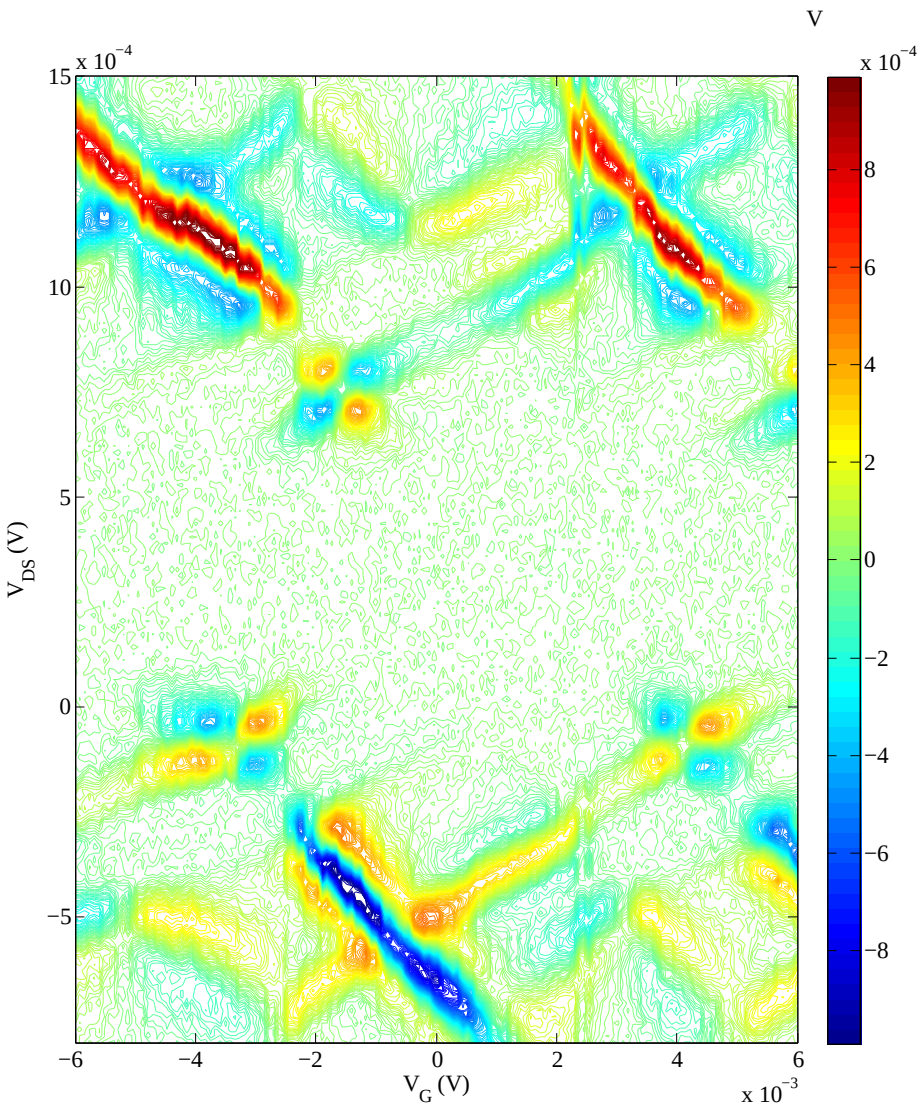

Figure 4.10: Gain map of SET. Data taken simultaneously with data in Fig. 4.9.

4.1.7 RF-Tank Circuit and SET DC Resistance

To characterize the properties of the RF measurement circuit, we measure shot noise in the SET. The SET shot noise is white and given by eI_{DS}. The resulting power spectral density measured by the spectrum analyzer is then

$$P = GeI_{DS}Z_0 \frac{\omega_T^4}{\left(\omega_T^2 - \omega^2\right)^2 - \left(\omega\omega_T/Q_T\right)^2} \tag{4.4}$$

where ω_T and Q_T are the center frequency and quality factor of the LC tank circuit, respectively, and G is the measurement circuit gain. An example is shown in Fig. 4.11.

We increase I_{DS} while measuring the noise power at the tank resonance, given by

$$P_N = G\left(k_B T_n + Q_T^2 Z_0 e I_{DS}\right) \tag{4.5}$$

Then from the slope and intercept we can find the measurement circuit gain and noise temperature as in Fig. 4.12.

This measurement also gives us I_{DS} versus V_{DS} for biases well beyond the Coulomb blockade from which we can find the SET DC resistance outside the Coulomb blockade region. The tank circuit properties and SET resistances for all three SET based samples are summarized in Table 4.2.

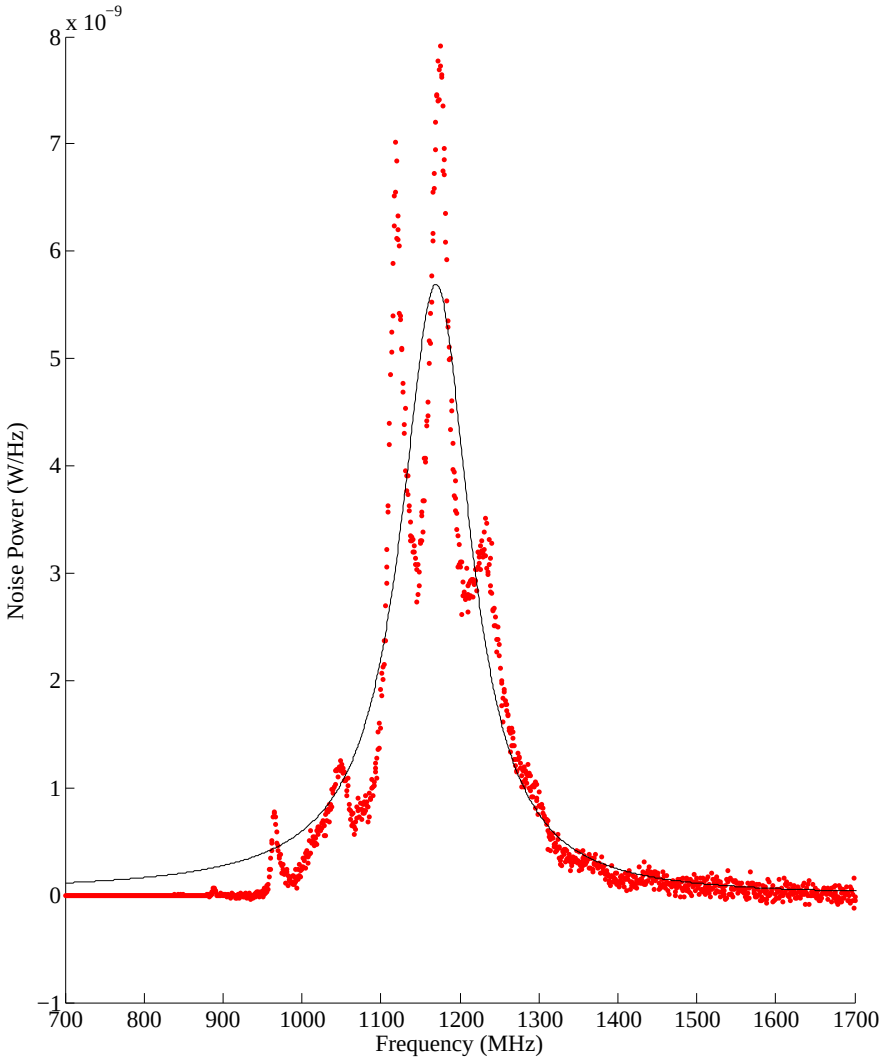

Figure 4.11: Example of shot noise ring-up of tank circuit from sample 1. $V_{DS} = 0.08$ V.

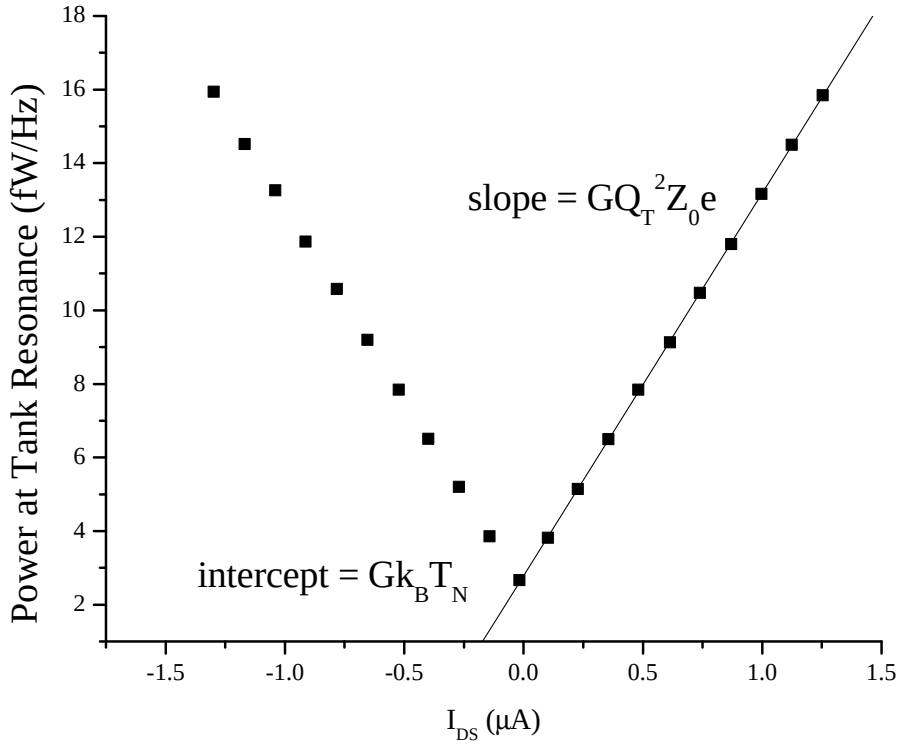

Figure 4.12: Example of using shot noise ring-up to characterize RF circuit. Data from sample 2.

	Sample 1	Sample 2	Sample 3
Tank Frequency (GHz)	1.168	1.1678	1.1704
Tank Q	10.2	9.2	10.3
RF Gain (dB)	70	72	71
Noise Temperature (K)	22	11.3	15
SET Resistance (kΩ)	85	78.6	34.7

Table 4.2: RF Circuit Properties.

4.1.8 Nanoresonator Characterization

For samples 2 and 3 we did noise thermometry measurements of the nanoresonator position noise. At several different bath temperatures we measured the reflected power from the RF-SET at the mechanical resonance frequency. An example is shown in Fig. 4.13, where the gate reference signal has been used to scale the noise power in charge units, e^2/Hz. This data provides a calibration to convert any position noise to an equivalent mechanical mode temperature, T_n. The noise power for sample 2 has an x-intercept consistent with zero. Sample 3, in contrast, intercepts the x-axis near 22 mK.

In principle, the noise thermometry data can be used to find the effective mass of the samples. First, we convert the noise from charge units to meters via

$$q^2 = \frac{C_{NR}^2}{d^2} V_{NR}^2 X_0^2 \tag{4.6}$$

Then we can find the mass from the slope of position noise vs. temperature in Fig. 4.14 and equipartition of energy, Eq. 1.11. There is a factor of 10 difference in the mass found for samples 2 and 3. These devices were fabricated to have the same dimensions and I do not expect those dimensions to vary by more than 20%.

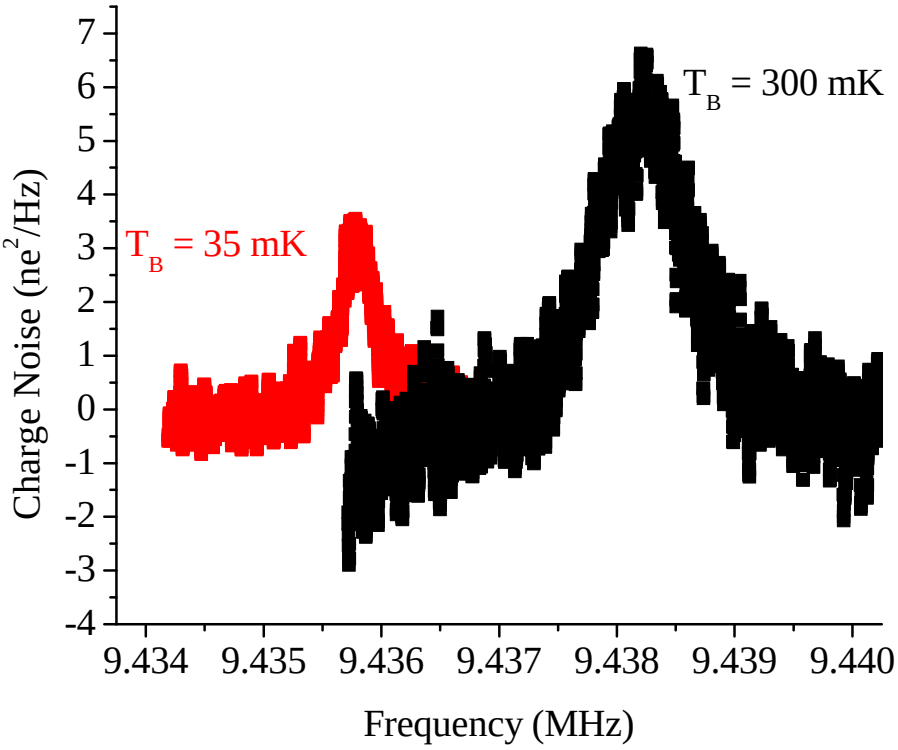

Figure 4.13: Thermal noise of sample 3. For clarity, the noise floor has been subtracted and the 300 mK resonance has been shifted up in frequency by 2 kHz.

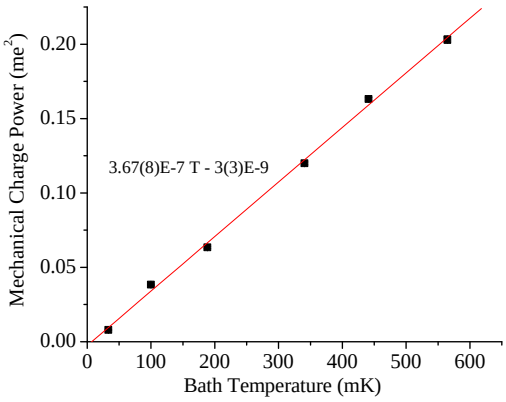

(a) Sample 2

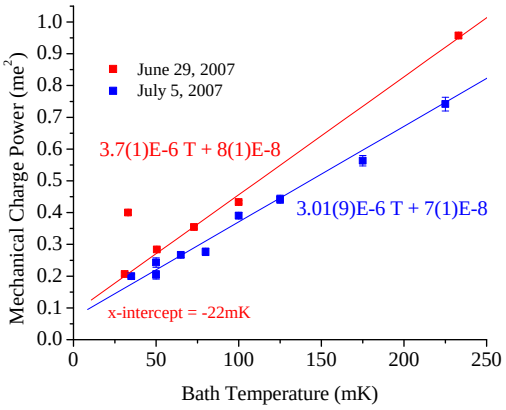

(b) Sample 2

Figure 4.14: Mechanical noise thermometry of samples 2 and 3.

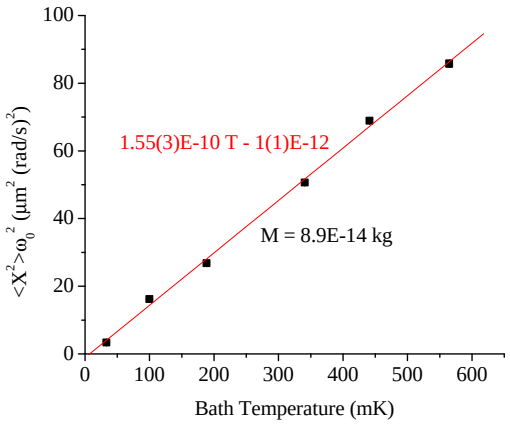

(a) Sample 2

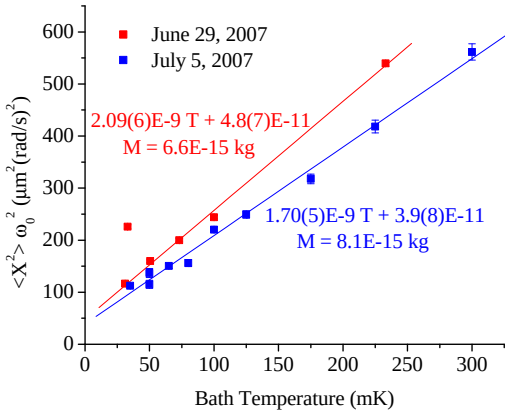

(b) Sample 2

Figure 4.15: Finding the effective mass of the nanoresonator in samples 2 and 3 using the noise thermometry data from Fig. 4.14.

	Sample 1	Sample 2	Sample 3
Frequency (MHz)	11.1	8.5	9.4
Resistance (Ω)		23	17.7, 29.9
Quality Factor	180,000	100,000	30,000
Effective Mass (kg)	1.8×10^{-15}	1.8×10^{-15}	1.8×10^{-15}

Table 4.3: Nanoresonator properties for RF-SET based samples.

Also, from the density of materials used and the nominal dimensions of the beams, I expect the mass to be about 1.8×10^{-15} kg. These differences lead me to conclude that the noise thermometry data given here is not an accurate calibration of the mass. A possible explanation for this discrepancy is given in the appendix. I will use the first principles mass throughout the remainder of this thesis.

By monitoring the sideband of the reflectance from the SET at the frequency of I_F, we can also determine the resistance of the beam. Comparing this sideband to the gate charge reference signal, we know the charge noise being produced at the center of the beam. Then, since we know the capacitance between the beam and the SET and we know how much current we are sending through the beam, we can calculate the resistance, as in Fig. 4.16. This measurement was done for samples 2 and 3. The resistance of sample 3 appeared to fluctuate between two values.

Nanoresonator masses, resistances, resonant frequencies, and quality factors are summarized in Table 4.3. The resistances of samples 2 and 3 are consistent with measurements of sample 1 at 77 K (30 Ω) and sample 3 at 4 K (20 Ω).

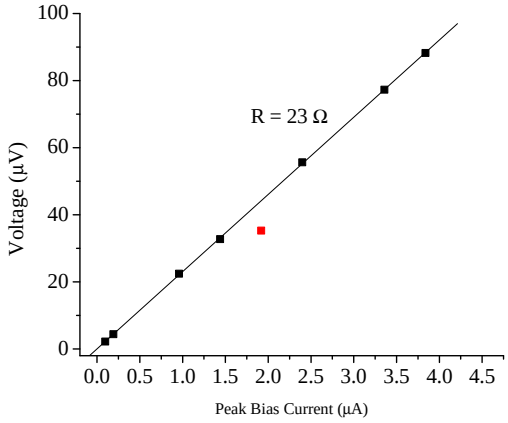

(a) Sample2

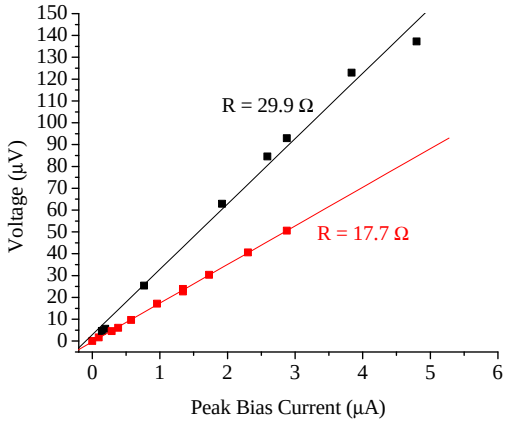

(b) Sample3

Figure 4.16: Beam resistance for samples 2 and 3.

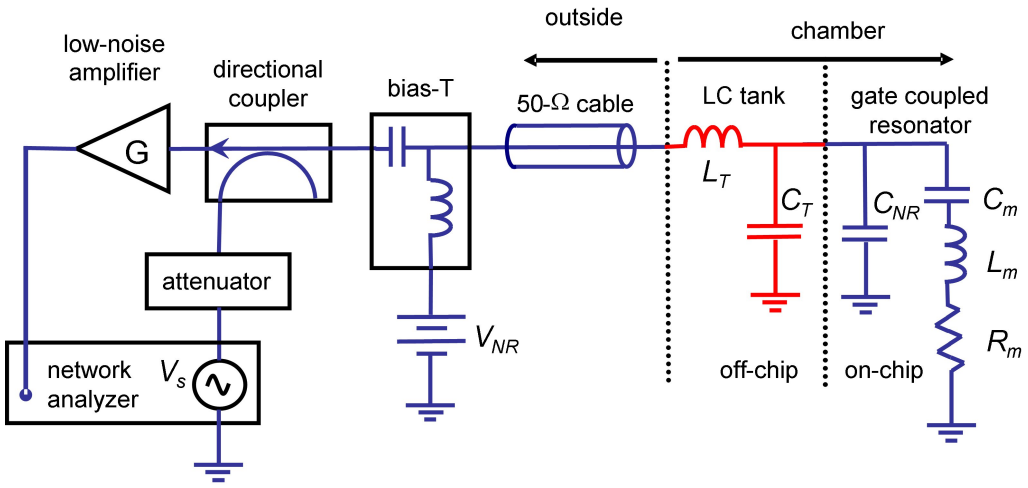

Figure 4.17: Schematic of measurement scheme for voltage biased and impedance matched capacitive detection.

4.2 Capacitive Detection Device Operation

Capacitive detection for dissipation measurements was also performed using reflectometry. The circuit diagram is shown in Fig. 4.17. A bias-tee allows for bringing both the DC bias voltage, V_{NR}, as well as the smaller AC driving voltage, V_s, to the device. Then, using a network analyzer and directional coupler we perform standard RF reflectometry on the device to monitor its impedance and thus detect the resonator's motion (see Appendix for further details).

4.3 Notes on Wiring

The desired values of the DC bias voltages were set by a PC controlled DAQ card and sent into the shielded room through optical isolators. Near the input to the fridge, they were divided by a factor of 100 to 1000 and then filtered. The filtering consisted of both commercial low-pass RF filters as well as homemade pi-powder filters [41] that provide more than 90 dB attenuation above 1 GHz. Inside the fridge,

these signals were carried by stainless steel coax down to the 1 K pot stage and then copper lines to the sample. The lines were thermalized at the 4 K flange and passed through powder filters at the 1 K pot and mixing chamber stages. The coupling voltage between the nanoresonator and the gate or SET, V_{NR}, was sent down to the beam in the same manner, except that it was supplied by batteries inside the shielded room.

RF signals entered the shielded room through DC blocks. The 1 GHz carrier for RF-SET detection was attenuated by 20 dB, then carried by stainless steel coax down to the 1 K pot stage. There, it was attenuated by another 20 dB before going into the input of a directional coupler (see Fig. 4.1). From the coupled port of the directional coupler, the signal was carried by niobium coax, the inner conductor of which was thermalized at 1 K via a short length of microstrip transmission line. The microwave carrier and V_{DS} were combined via a bias-tee before being sent to the sample via copper coax.

Chapter 5

Results

This chapter details the results of our attempts to measure electromechanical noise in nanomechanical resonators. I first discuss displacement noise measurements on gold coated nanoresonators driven by a 1 MHz bias current. Then, I discuss equilibrium dissipation measurements made on aluminum coated nanoresonators in both the normal and superconducting states.

5.1 Data for Current Biased Gold Nanoresonators

5.1.1 Displacement Noise

Displacement fluctuations of the gold coated current biased nanoresonators were measured using the RF-SET. Figure 5.1 shows the noise response of the three nanoresonators to an applied bias current, in equivalent charge noise units.

Each plot also includes a linear fit to the data. Some points in samples 2 and 3 are not included in the fit (red) as they do not fit the overall trend. These include points at low bias in sample 3 where the saturation to the bath temperature is evident and a few points at higher bias in both samples 2 and 3 where the nanoresonator appeared to be undergoing some change, possibly being damaged by the bias circuit.

I can convert the mechanical response spectra into equivalent mode tempera-

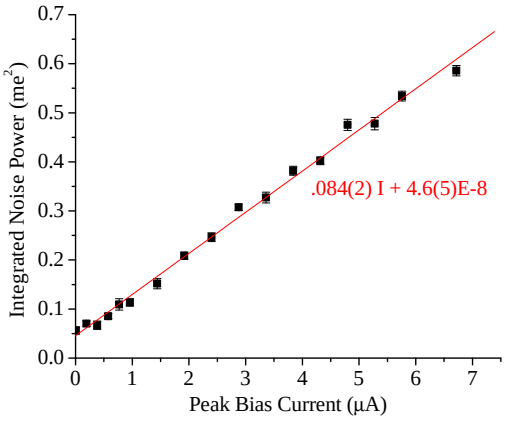

(a) Sample 1

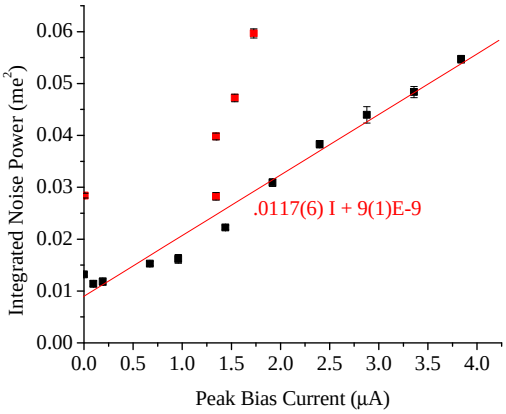

(b) Sample 2

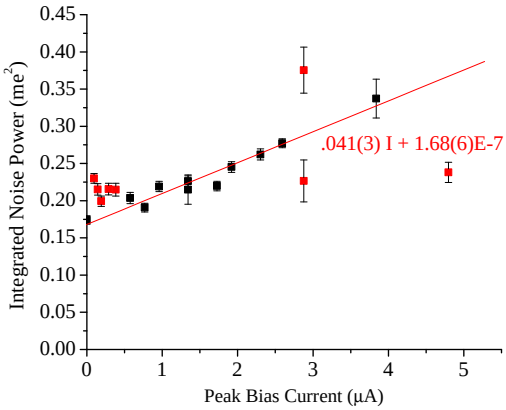

(c) Sample 3

Figure 5.1: Average integrated mechanical response in electron units vs. bias current.

tures by integrating the area under each curve and using the linear relation between integrated response and temperature found in the previous chapter as a calibration. The mode temperature vs. bias current is plotted in Fig. 5.2. For sample 1 there was no noise thermometry data taken, so the data is simply scaled so that the mode temperature is 30 mK (the bath temperature for those measurements), for the lowest bias current.

Superimposed on each mode temperature plot is the average temperature of the electron gas in the conducting layer, as predicted by Eq. 1.26. The resistance at 30 mK for sample 1 was not measured, so lines are drawn for $R = 23\,\Omega$, the average resistance of samples 2 and 3, and $R = 40\,\Omega$, which provides the best fit to the data. For sample 3, the measured resistance varied between two values as the data was taken. Red (triangle) data points were taken when the beam resistance was measured to be 29.9 Ω, while black (square) data points correspond to a beam resistance of 17.7 Ω.

To convert the data to equivalent force noise on the nanoresonator, we use Eq. 1.12 to find the force noise from the mode temperature and Q. The results are shown in Fig. 5.3 From the theory, the electromechanical force noise should follow

$$S_F = (.83)\frac{4}{5}\frac{p_F^2}{e}\frac{2}{\pi}I \tag{5.1}$$

where I have recast Eq. 1.20 in terms of current by using $V = IR$ and the Drude resistivity $p_F/n_e e^2 \ell$. Here, $p_F = 1.28 \times 10^{-24}$ is the Fermi momentum for gold [42] and the factor of $2/\pi$ accounts for averaging the AC current over a half-cycle. This

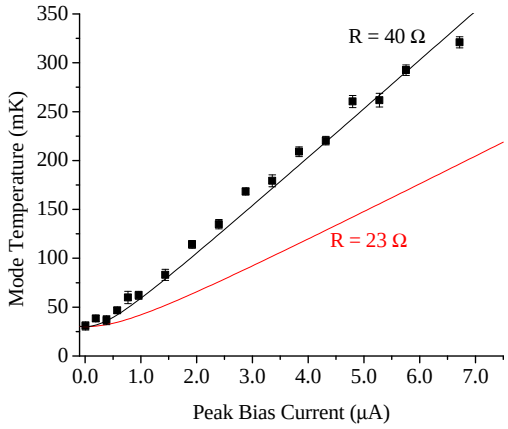

(a) Sample 1

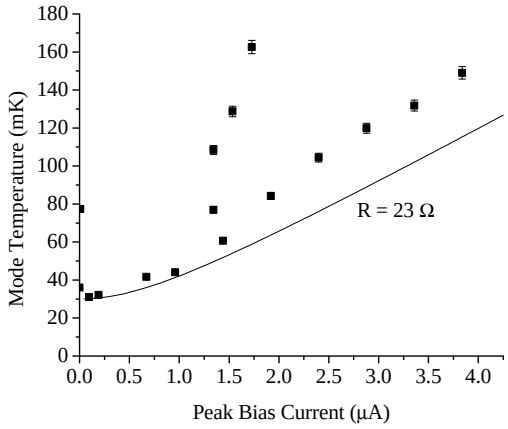

(b) Sample 2

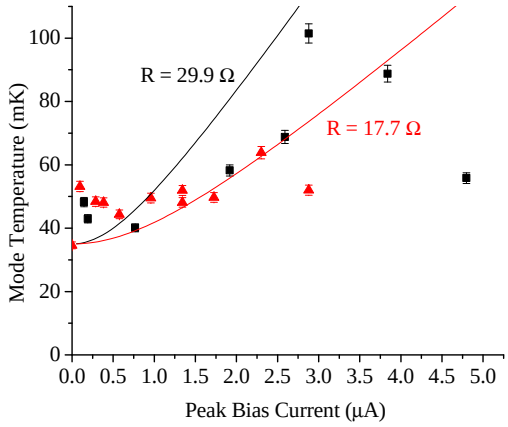

(c) Sample 3

Figure 5.2: Mode temperature vs. bias current. Lines are the expected average electron gas temperature along the beam profile.

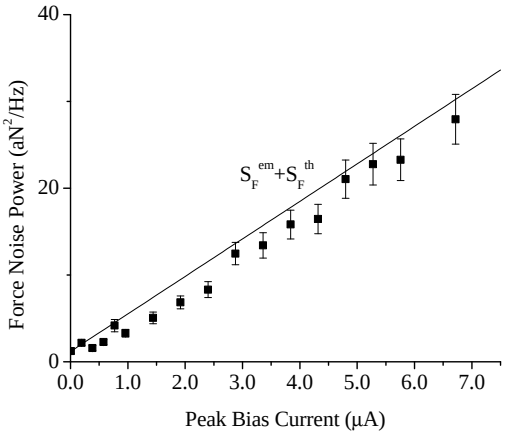

(a) Sample 1

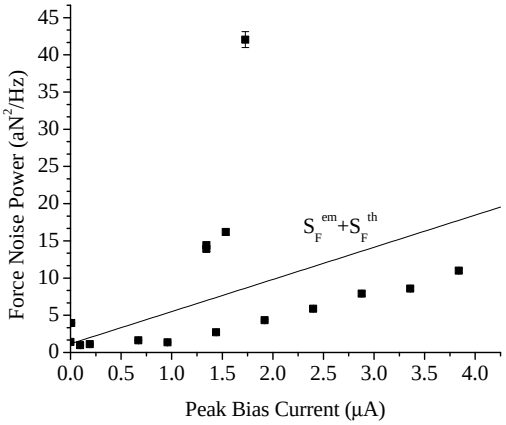

(b) Sample 2

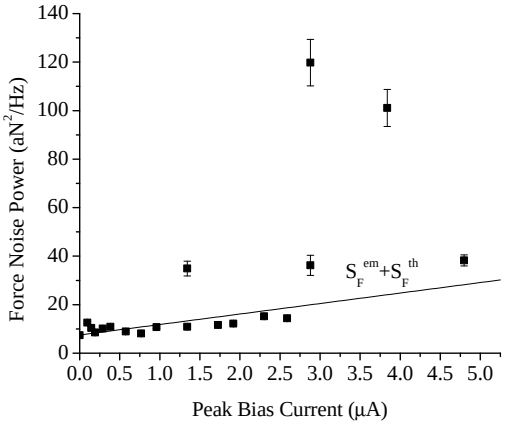

(c) Sample 3

Figure 5.3: Force noise power vs. bias current. Solid black lines are theory for electromechanical noise.

theoretical line has been included in Fig. 5.3, offset by the thermal noise at base temperature.

5.1.2 Dissipation and Frequency

It is also instructive to look at how the dissipation and frequency of the nanoresonators vary with temperature, both when the nanoresonator is in equilibrium with the bath and when it is driven to a higher temperature by application of a bias current. Figure 5.4 shows the dissipation, ω_0/Q for both cases (equilibrium data is missing from sample 1 as noise thermometry was not performed on that sample).

Previous experiments with nanoresonators have yielded a $T^{1/5}$ dependence of dissipation on temperature [43]. Such a curve has been fit for the dissipation data of samples 1 and 2. Sample 3 exhibited different behavior in that the overall dissipation was about an order of magnitude larger and the trend with increasing temperature was roughly linear. Also note that in samples 2 and 3, the dissipation is roughly the same whether the mode temperature is raised independently of the bath or with it.

The dissipation predicted for momentum noise is given by

$$\gamma_{em} = \frac{4.87}{5}\frac{p_F^2}{e^2}\frac{1}{RM} \tag{5.2}$$

For $R = 23\,\Omega$, the average resistance measured for samples 2 and 3, and $M = 1.8 \times 10^{-15}\,\mathrm{kg}$, I find $\gamma_{em} = 1502$ Hz.

This dissipation is larger than what is observed in samples 1 and 2. However,

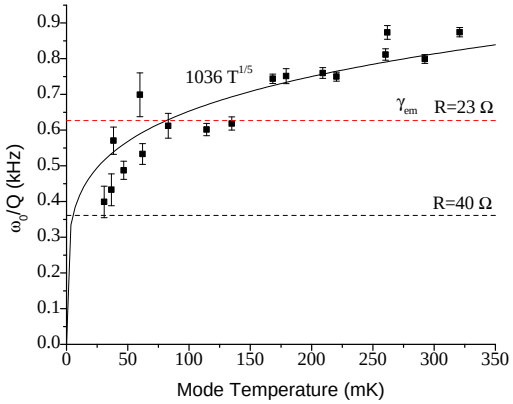

(a) Sample 1

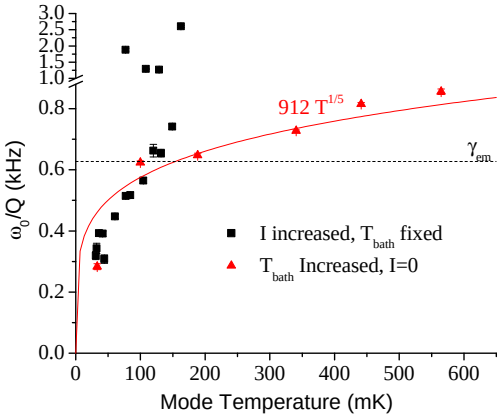

(b) Sample 2

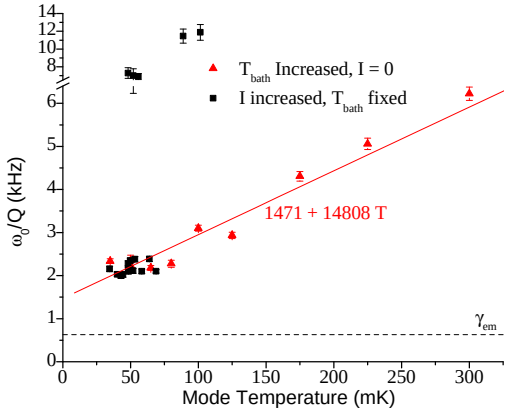

(c) Sample 3

Figure 5.4: Dissipation vs. temperature.

we must also account for the fact that the nanoresonator is a composite of a Si_3N_4 substrate and a gold film. The dissipation is defined as the energy loss per cycle over the total energy, both of which can be different in the two layers. Assuming that the electromechanical dissipation is confined to the gold film, we must use [44]

$$\gamma_{em} \rightarrow \frac{\beta}{1+\beta}\gamma_{em} \tag{5.3}$$

where

$$\beta = \frac{Y_{Au}t_{Au}}{Y_{SiN}t_{SiN}} \tag{5.4}$$

Assuming the Young's modulus of gold $Y_{Au} = 80$ GPa [45], nitride $Y_{SiN} = 290$ GPa [46] and the thicknesses are $t_{Au} = 130$ nm and $t_{SiN} = 50$ nm, I get $\gamma_{em} = 627$ Hz. This dissipation is the expected lower bound if electromechanical dissipation is the only source of dissipation. Though they exhibit a temperature dependance not predicted by Eq. 5.2, both samples 1 and 2 have dissipations that stay within approximately 50% of this value. I have also drawn a line on Fig. 5.4(a) for a dissipation of 361 Hz, which would be expected if $R = 40\,\Omega$

Figure 5.5 shows the frequency shifts as a function of bath or mode temperature for the three samples. Sample 2 exhibits a much larger frequency shift when the bath temperature is raised than when only the mode temperature is raised, though it should be noted that the frequency at base temperature, f_0, shifts up about 30 kHz between the two measurements. In contrast, sample 3 shows a similar frequency depedence on temperature for both cases.

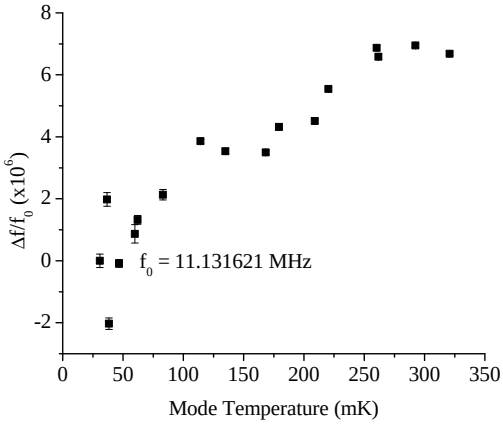

(a) Sample 1

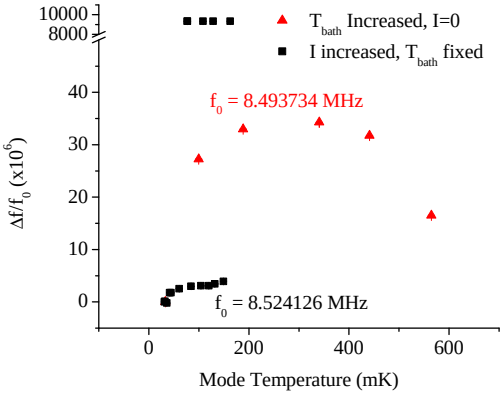

(b) Sample 2

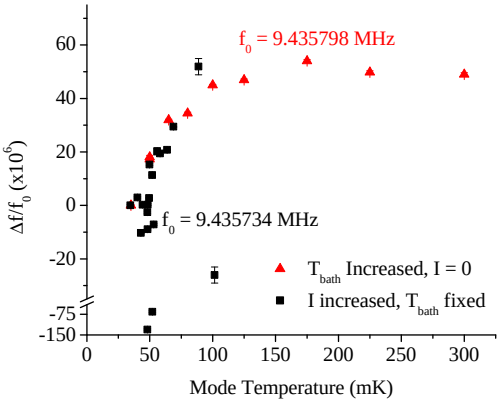

(c) Sample 3

Figure 5.5: Fractional frequency shift vs. temperature.

5.2 Data for Aluminum Coated Resonators

5.2.1 Quality Factor vs. Magnetic Field

The quality factor, Q, of aluminum coated resonators was measured using the capacitive detection technique, with the samples immersed in a magnetic field. Eddy current damping is expected to be a small effect for resonators of this size [47]. The resistance of sample 4 was measured with a 1-wire measurement from the top of the dilution refigerator, while sample 5 was measured with a 2-wire measurement at the nanoresonator bond pad. Sample 4 was oriented with the beam axis perpindicular to the field, while sample 5 was in a parallel orientation. In both cases, the sample substrate was parallel to the field. The resistance of the beams was also measured as a function of magnetic field to determine the critical fields of the two samples. The critical field behavior was measured with bias currents ranging from 50 to 1000 nA and at frequencies ranging from 25 to 100 kHz and exhibited no difference over these range of parameters. The quality factor's and beam resistances vs. magnetic field are shown in Fig. 5.6.

We attribute the two steps at higher fields to the aluminum. I first note that the resistance through the nanoresonator of sample 5 was measured at 4 K to be $30\,\Omega$, including the leads, bond pads, and about 1 m of stainless steel coax. This value is consistend with the combined $20\,\Omega$ resistance change shown in Fig. 5.6(b). Also, the resistance vs. temperature of sample 5 was measured and is shown in Fig. 5.7. There is a large step in resistance that has a height equal to the sum of the two steps shown in Fig. 5.6(b). The position of this step between 1.25 and 1.35

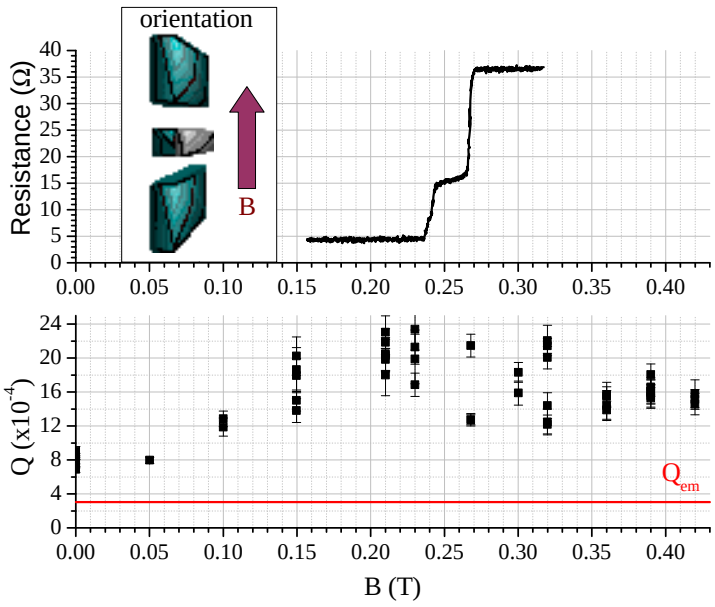

(a) Sample 4

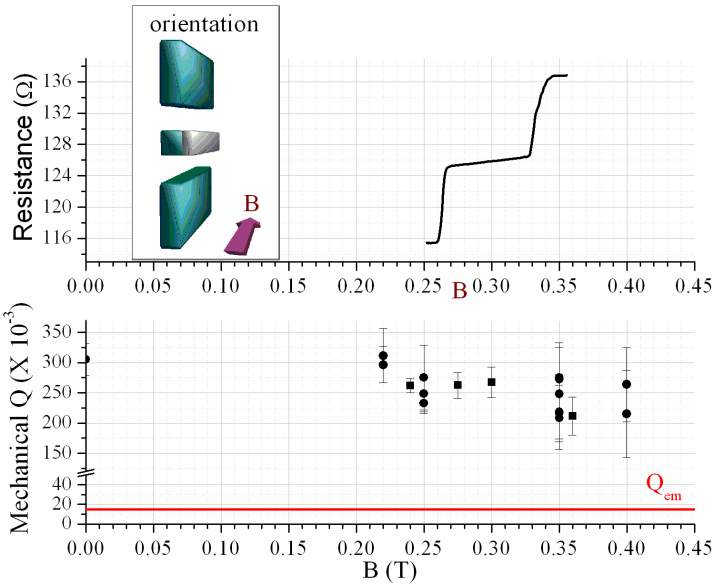

(b) Sample 5

Figure 5.6: Quality factor and beam resistances vs. magnetic field. Insets show beam orientation relative to magnetic field.

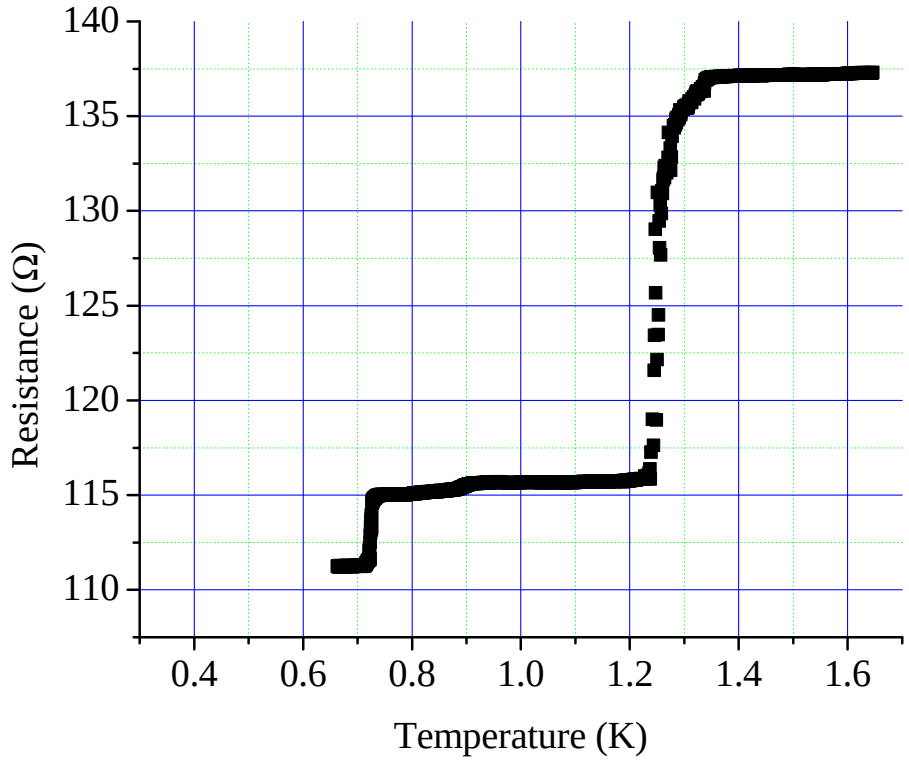

Figure 5.7: Resistance versus temperature of sample 5.

K is consistent measured reported values for the critical temperature of thin film aluminum [48, 49]. The smaller step can be attributed to the bond pads, which are made of an Al-Ti-Au trilayer known to superconduct below 700 mK [50].

Without a direct 4-wire measurement, it is difficult to speculate whether both resistance steps are due to the nanoresonator. It is possible that the existance of two steps is due to the aluminum leads from the bond pads to the nanoresonator having a different critical field than the nanoresonator itself. However, since there is not enough evidence to make this claim conclusively, I will simply use the combined sum of both steps as an upper bound.

Both samples are expected to have a bare mass of about 2×10^{-15} kg. From Eq. 5.2 and Eq. 5.3 (with the Young's modulus of aluminum, Y_{Al}, assumed to be 65 GPa), we expect electromechanical Q's in the normal state of 30,260 and 14,753 for samples 4 and 5, respectively. These values should be the upper bound for Q in the normal state, yet we observe Q's about 6 to 15 times larger.

5.2.2 Loading

The discrepancy in Q between theory and experiment becomes even more pronounced if we take into account loading from the external measurement circuit. Part of the dissipation in Fig. 5.6 results from energy being dissipated in the external circuit and is not indicative of the intrinsic losses in the nanoresonator [8]. To see how loading affects the overall quality factor, we put a complex external impedance $R_x + iX_x$ in series with the RLC model of the beam impedance (see Fig. 5.8). The loaded Q is given by

$$\frac{1}{Q_L} = \frac{1}{Q} + \frac{V_G^2 C_G^2}{\omega_0 d^2 M} R_x \tag{5.5}$$

We made several measurements of Q vs. V_G at different magnetic fields for sample 4. In Fig. 5.9, I plot $1/Q$ vs. V_G^2/ω_0. The intercept of these plots, shown in Fig. 5.10, should give the dissipation without loading. Except for the zero field case, the intercepts give an intrinsic Q of around 500,000. The analysis performed here assumes that a) $R_x(\omega_0)$ does not vary appreciably over the bandwidth of the mechanical resonance, which is a valid assumption given $Q/Q_T \sim 10^3$ and b) $R_x(\omega_0)$ does not vary much as the beam frequency shifts with V_G, an effect explained in the

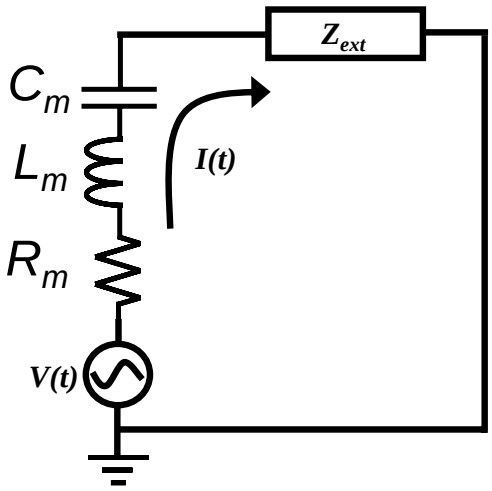

Figure 5.8: General loading model for capacitive detection.

appendix and shown in Fig. 5.11. In Fig. 5.12, I show the relative frequency range of the mechanics to the tank resonance at each field. It is clear that assumption (b) is not valid for B=0 Tesla, which may explain the difference in intercept at that field.

5.2.3 Temperature Dependence

For completeness, we also show the temperature dependence of the quality factor of samples 4 and 5. The dissipation vs. temperature is *not* expected to exhibit a discontinuity at the superconducting transistion as it should vary smoothly with the number of thermally excited quasiparticles, which goes as $e^{-\Delta/k_BT}$ [18]. The Q above T_C is consistent with the value predicted for electromechanical noise, however.

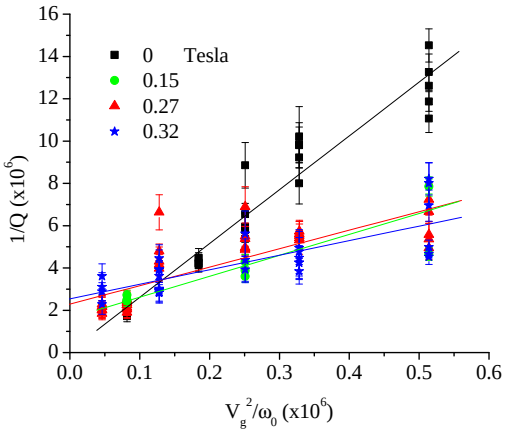

Figure 5.9: Dissipation vs. gate voltage squared/ω_0 for sample 4.

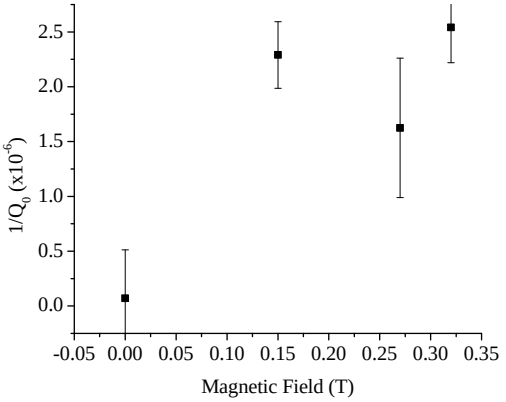

Figure 5.10: Sample 4 intrinsic dissipation vs. magnetic field.

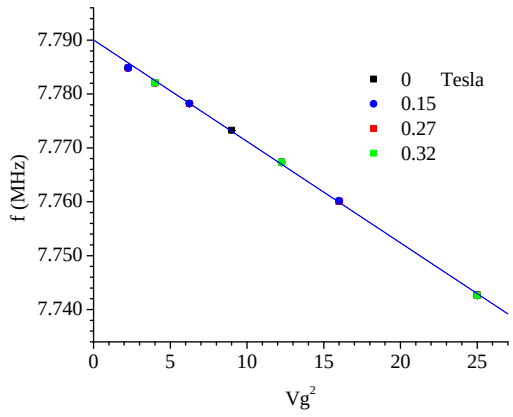

Figure 5.11: Resonant frequency of sample 4 vs. gate voltage squared.

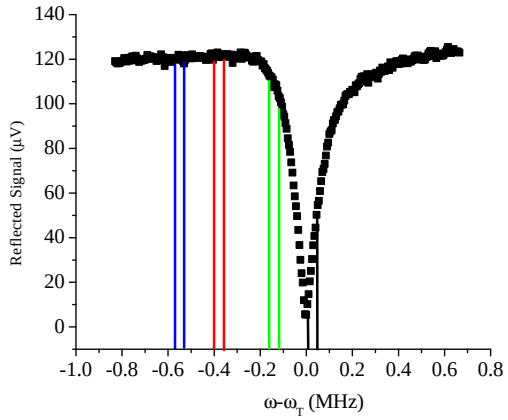

Figure 5.12: Mechanical resonance frequency range for data in Fig. 5.9 relative to tank resonance frequency, ω_T. Pairs of vertical lines show relevant range for each field. From right to left: Black=0, Green=0.15, Red=0.27, Blue=0.32 Tesla. Tank resonance data curve is taken from 0.32 Tesla data.

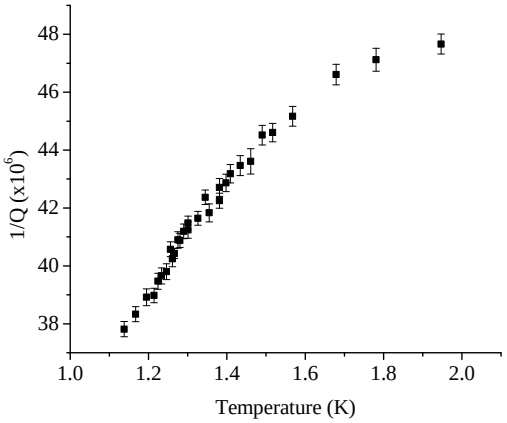

Figure 5.13: Quality factor vs. temperature of sample 4.

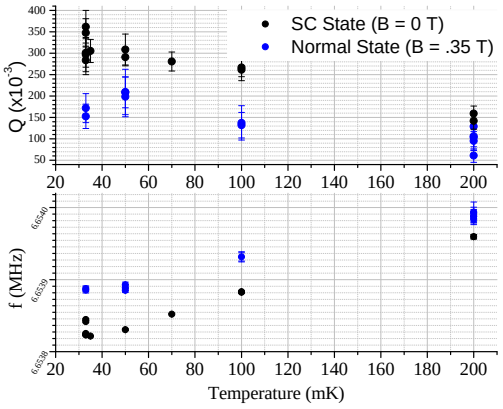

Figure 5.14: Quality factor vs. temperature of sample 5.

Chapter 6

Conclusion

6.1 Discussion of Results

Looking again at the data, Fig. 5.3 indicates a strong agreement between theory and experiment. The only adjustable parameters for the fits are the mass of the resonator and the Fermi momentum of the conducting medium.

On the other hand, Fig. 5.4 shows a clear dependence of Q on mode temperature, which is not explained by the theory. This temperature dependence argues that the nanoresonator is coupled to another thermal bath in addition to the electron gas. The total force on the nanoresonator mode is proportional to its temperature, T_m, over its quality factor Q_m. Assuming the nanoresonator is coupled to the electrons at temperature T_e with dissipation Q_e and a second bath we temperature T_p and dissipation Q_p, we have

$$\frac{T_m}{Q_m} = \frac{T_e}{Q_e} + \frac{T_p}{Q_p} \tag{6.1}$$

and

$$Q_m = \frac{Q_e Q_p}{Q_e + Q_p} \tag{6.2}$$

Figure 5.2 strongly suggests that the mode temperature follows the electron gas temperature, $T_m = Q_m$. The question is then how does it attain that temperature? Is heat being transferred directly from the electron gas, or from an intermediary

source that itself is heated by the electron gas? Looking at Eq. 6.1 and Eq. 6.2, one possibility is that $Q_e >> Q_p$, so that $T_m = T_e$ and $Q_m = Q_e$. However, in samples 1 and 2, the quality factor dropped by a factor of two over the range of temperatures studied, suggesting that Q_p is at least of the same order as Q_e. Also, sample 3 had a quality factor about three times lower than that predicted for electromechanical dissipation alone, yet still exhibits good agreement between mode temperature and predicted average electron temperature.

We next suppose that $Q_p = Q_e$ and $T_p << T_e$. In this scenario, we would be left with $T_m \simeq T_e/2$.

Thus it appears that, at least at higher bias currents, there is another source of dissipation coupled to the nanoresonator with temperature near T_e. We cannot be sure where this dissipation comes from, but one possible source to consider is the phonon gas. Normally, we would expect the phonon gas to stay cool relative to the electron gas, since electron-phonon coupling is very weak at low temperatures, giving rise to the "hot electron" effect [51]. However, even if very little heat is transferred to the phonon gas from the electrons, it will still heat up if thermal conduction out through the nanoresonator is even weaker.

To investigate this possibility, I consider a simple thermal circuit for the system, shown in Fig. 6.1. Here I assume that the bath temperature is T_b = .03 K and

- $Q1 = I^2R$, The power dissipated in the electron gas, I^2R, taken to be deposited at the center of the beam.

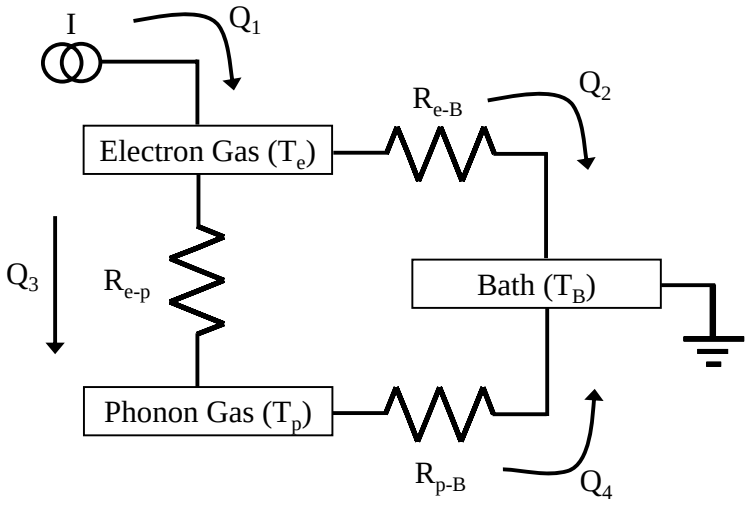

Figure 6.1: A simple thermal model for the nanoresonator.

- $Q2 = 2L_0/R \times (T_e^2 - T_b^2)$, The power flowing from the electron gas out through the leads (Weidemann-Franz). L_0 is the Lorenz number, equal to 2.45×10^{-8}. The factor of 2 takes into account that diffusion can occur in either direction with resistance $R/2$ from the center.

- $Q3 = \Sigma V(T_e^5 - T_p^5)$, The power from the electrons to the phonons through electron-phonon coupling. Σ is taken to be the empirical value 2×10^9 [52].

- $Q4 = (4\pi^2 k_B^2)/(3h) \times (T_p^2 - T_b^2)$, The power from the phonon gas to the bath through 8 times the quantum of thermal conductance (two directions, 4 modes per direction).

I solved this system numerically for the temperatures of the electron gas and phonon

gas and found the results shown in Fig. 6.2.

While a complete model would have to take into account the fact that the dissipated power is distributed along the length of the beam, the results do indicate that at the higher bias currents, the phonon temperature can follow the electron temperature.

Another possibility that cannot be ruled out by the data is that Shytov et al. have overestimated the direct coupling between the electrons and the resonator mode. In this scenario, the mode temperature would still follow the temperature of the electron gas because it is coupled to the phonons, which themselves are heated by the electron gas. The lack of a change in Q at the critical field for the aluminum resonators provides some support for this assertion.

In the end, it is difficult to ignore the quality of agreement between theory and experiment for the electromechanical noise itself. In our experience, the force noise due to impurity scattering of conduction electrons is well predicted by Shytov et al., with the role of dissipation requiring more study.

6.2 Suggestions for future work

Because the electromechanical force noise is predicted to be independent of geometry, future efforts to observe it should optimize their devices to suppress heating of the phonon gas. Making the nanoresonator as short as possible, so that hot electrons are able to diffuse out the leads before scattering off a phonon, would help in this regard. Figure 6.2 suggests that future efforts should concentrate on lower

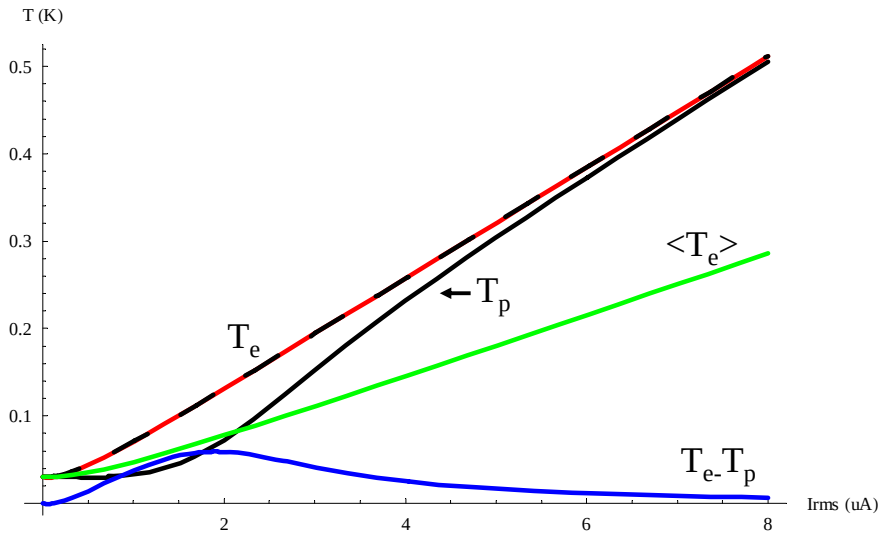

Figure 6.2: Results of numberical simulation of electron (red) and phonon (black) temperatures. The blue curve is the difference between the two temperatures, showing for what range of currents the electrons are hotter than the phonons. The black dashed line shows the temperature of the electron gas with electron diffusion only (no electron-phonon coupling), indicating that Weidemann-Franz type conduction is still the main factor in determining the temperature. The green curve gives the result for the average electron temperature for the full distributed power model with no electron-phonon coupling.

bias currents, in the region where the phonon gas temperature is still relatively flat while the electron gas has already started to increase its temperature linearly.

Appendix A

Appendix

Here I describe in more depth our research in regards to the capacitive detection technique. In the first section, I show how we are able to succesfully model the behavior using the equivalent circuit model described in Chapter 2. I then demonstrate how this technique can be applied to the readout of arrays of resonators. The third section briefly deals with parametric amplification. Finally, I conclude with a look at a linear coupling between transverse mechanical modes.

A.1 Testing of the Capacitive Detection Model

To test the implementation of our capacitive detection scheme we used the measurement setup shown previously in Section 4.2 and shown in Fig. 4.17. Measurements were performed in a vacuum probe (Fig. A.2) immersed in liquid helium at 4 K. The sample chip was mounted in the probe in a homemade sample package and wirebonded to SMA connectors leading to the readout cables (Fig. A.1).

With V_{NR} set at 15 V, we used the network analyzer as the drive source and swept the frequency through the beam's resonance. The measured signal was the reflected voltage. The network analyzer divides this signal by the input signal, giving the reflection coefficient

$$\Gamma_{11} = \frac{Z - 50}{Z + 50} \tag{A.1}$$

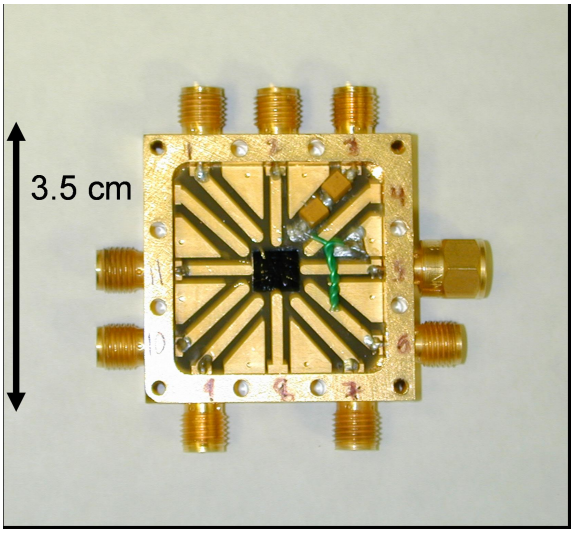

Figure A.1: Picture of sample in sample package. The tank circuit is composed of two chip inductors and a small length of twisted pair serving as the capacitor.

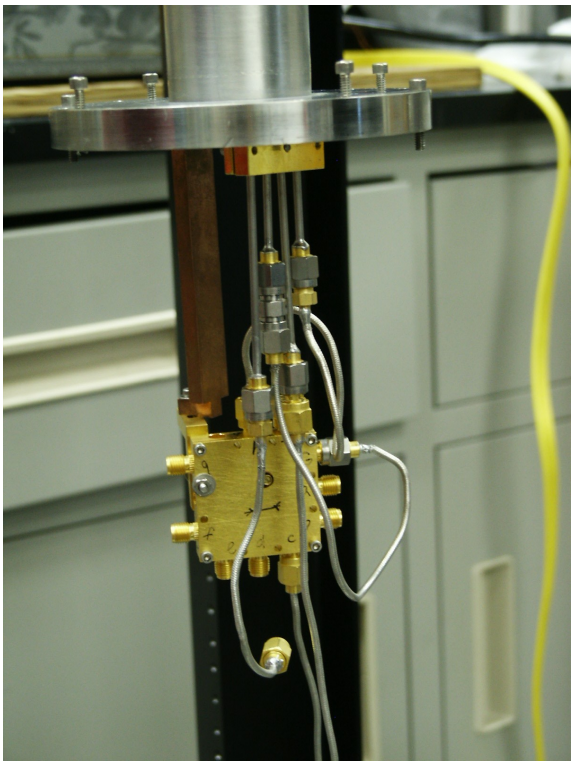

Figure A.2: Picture of 4.2 K probe.

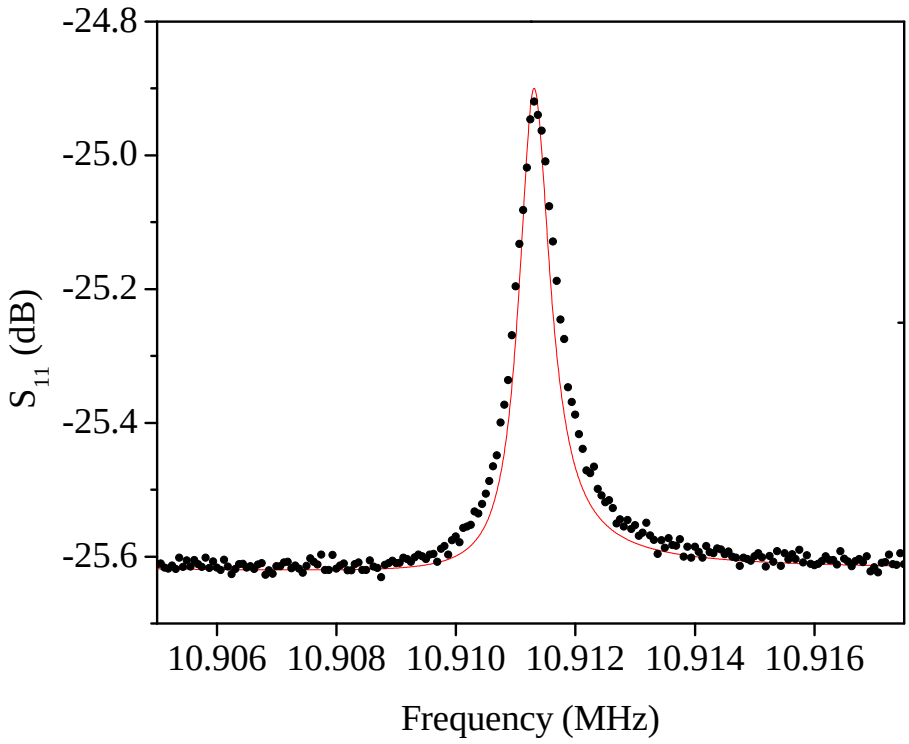

Figure A.3: Reflected signal as a function of drive frequency. The red line is a fit using the circuit model shown in Fig. A.5.

Figure A.3 shows the response of the reflected signal as the drive frequency is swept through the mechanical resonance. A measurement with a wider frequency span is shown in Fig. A.4.

The red curves in Fig. A.3 and A.4 are fits, both using the same circuit model, shown in Fig. A.5. This model incorporates the beam, gate and tank impedances, the same as shown in Fig. 2.4, as well as the nonzero resistance of the tank inductor, R_T, and a lumped element RLC model for the impedance of the coaxial line in the probe. The source resistance, R_S, is 50 Ω. Also, there is -22 dB of attenuation added to the model to account for the net result of the attenuation of the drive signal, V_s, the

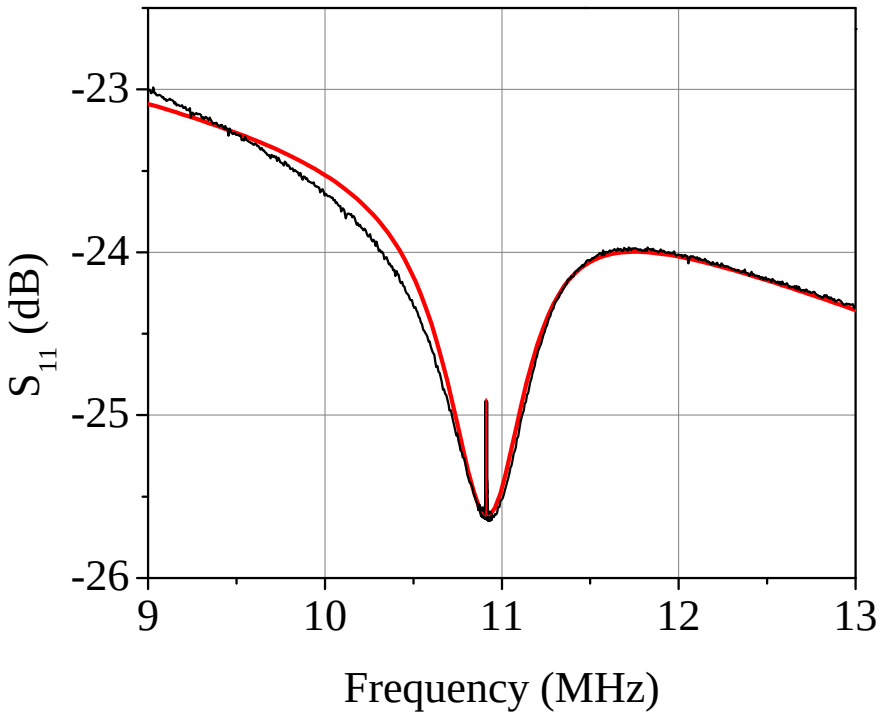

Figure A.4: Wider frequency sweep of the reflected signal showing the response of the tank circuit. The mechanical resonance can be seen as a sharp central peak.

L_m	4.94 H
C_m	28.1 aF
R_m	571 kΩ
L_T	33 μH
C_T	4.21 pF
R_T	470 Ω
L_c	100 nH
C_c	40 pF
R_T	3 Ω

Table A.1: Relevant dimensions for dissipation measurement devices.

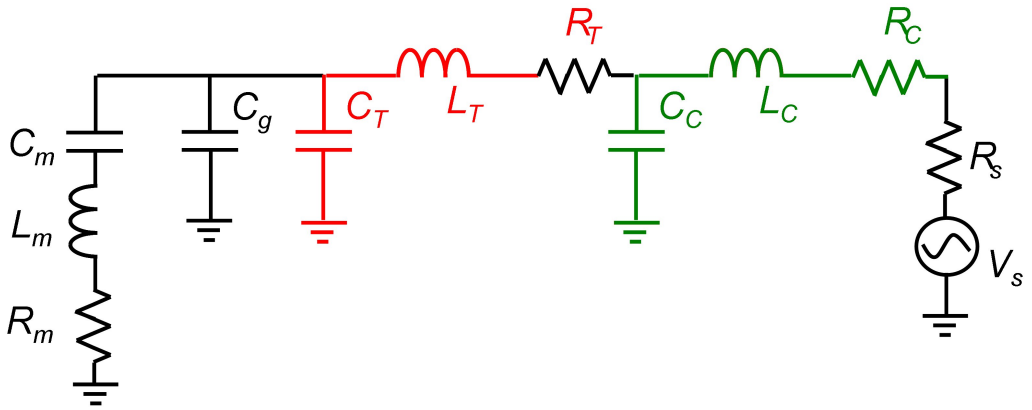

Figure A.5: Full circuit model for the measurement setup shown in figure 4.17.

insertion loss of the directional coupler and the gain from the readout amplifier. The circuit element values for the model are given in Table A.1. The electromechanical impedance values are derived from beam parameters: $M \simeq 1.2 \times 10^{-15}$ kg, $Q \simeq 26500$, $\omega_0/2\pi \simeq 11$ MHz, $C_{NR} \simeq 54$ aF and $d \simeq 180$ nm.

On resonance, the impedance seen by the network analyzer is the transformed electromechanical impedance (Eq. 2.12) plus the tank resistance, R_T (in our case, about 600 Ω). Off resonance, the impedance is simply R_T. I can calculate the peak

height by subtracting the reflection coefficients for these two impedances.

$$\begin{aligned} peakheight &= \Gamma_{11}(\omega_0) - \Gamma_{11}(background) \qquad \text{(A.2)} \\ &= \frac{\frac{Z_{LC}^2}{R_m} + R_T - 50}{\frac{Z_{LC}^2}{R_m} + R_T + 50} - \frac{R_T - 50}{R_T + 50} \\ &= \frac{100 Z_{LC}^2}{R_m R_T^2} \\ P &= \frac{100 Z_{LC}^2 C_G^2 Q V_{NR}^2}{d^2 M \omega_0 R_T^2} \qquad \text{(A.3)} \end{aligned}$$

In Fig. A.6, I plot the measured mechanical peak height divided by Q versus the applied bias voltage, V_{NR}. The V_{NR}^2 dependance implied by equation A.3 is clearly demonstrated.

Increasing the bias voltage, V_{NR}, not only increases the height of the reflectance peak, but also affects the frequency and quality factor of the mechanical resonance as well. These affects are seen in Fig. A.7

The frequency shift of an electromechanical resonator coupled to a nearby gate is a well-known effect and allows the resonator to be used as a sensitive electrometer [53]. The frequency of the mechanical resonance is determined by its spring constant and its mass through the relation $\sqrt{K/M}$. The spring constant is found from $k = \mathrm{d}^2U/\mathrm{d}X^2$, where the energy U is in two parts, the elastic energy stored in the lattice giving the spring constant in Eq. 1.7, as well as the energy stored in the

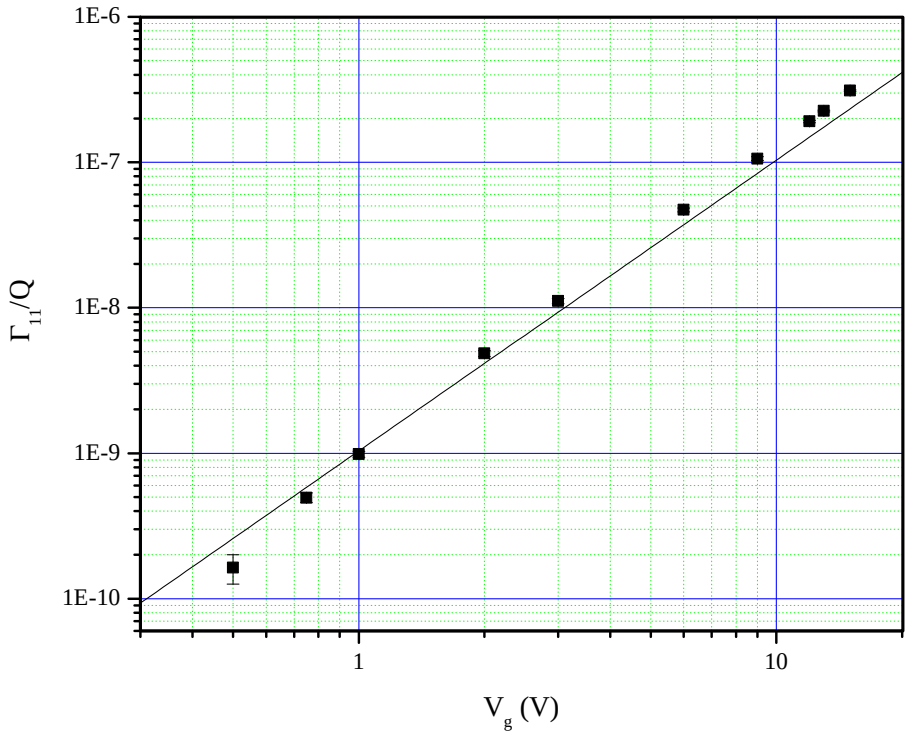

Figure A.6: Mechanical response amplitude vs. bias voltage V_{NR}. The data is scaled by the quality factor Q at each point to account for loading at higher bias voltages. The red line is a fit using the model in Fig. A.5.

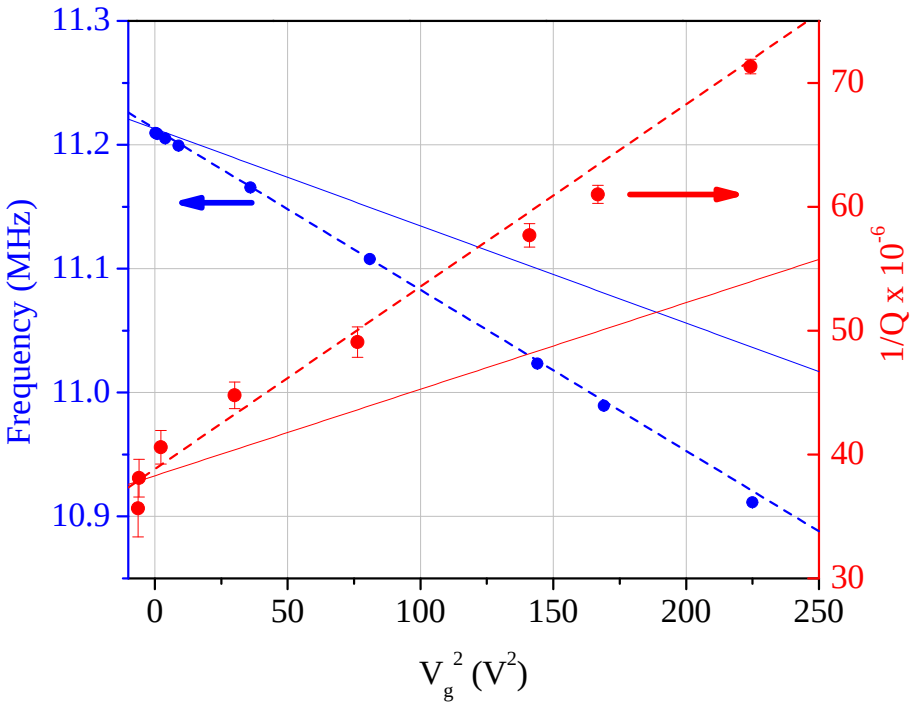

Figure A.7: Frequency and quality factor of mechanical resonance vs. bias voltage. Solid lines use parameters given in text. Dashed lines are best fit lines.

capacitance between the beam and gate. The effective spring constant is then

$$K_{eff} = K_{elastic} + K_{electrostatic} \tag{A.4}$$

$$= K - V_{NR}^2 \frac{\mathrm{d}^2 C(X)}{\mathrm{d}X^2} \tag{A.5}$$

$$K_{eff} \simeq K - V_{NR}^2 \frac{C_{NR}}{d^2} \tag{A.6}$$

Where again, I have used $X/d << 1$. The resonant frequency is then calculated from

$$\omega_m = \sqrt{\frac{K_{eff}}{M}} \tag{A.7}$$

Expanding about $K_C/K << 1$, I find

$$\omega_m = \omega_0 - \frac{1}{2}\frac{C_{NR}}{M d^2 \omega_0} V_{NR}^2 \tag{A.8}$$

The bias voltage also affects the loading contribution to the quality factor as discussed in Chapter 5. There, it was shown how the dissipation $1/Q$ goes as V_{NR}^2. The quadratic behavior of both the frequency and dissipation are demonstrated in Fig. A.7.

A.2 Capacitive Detection of Nanomechanical Resonator Arrays

One of the most important advantages to the capacitive detection technique is its suitability for the read-out of arrays of nanoresonators. As a proof of principle test of array read-out, we measured a device consisting of two separate banks of 10

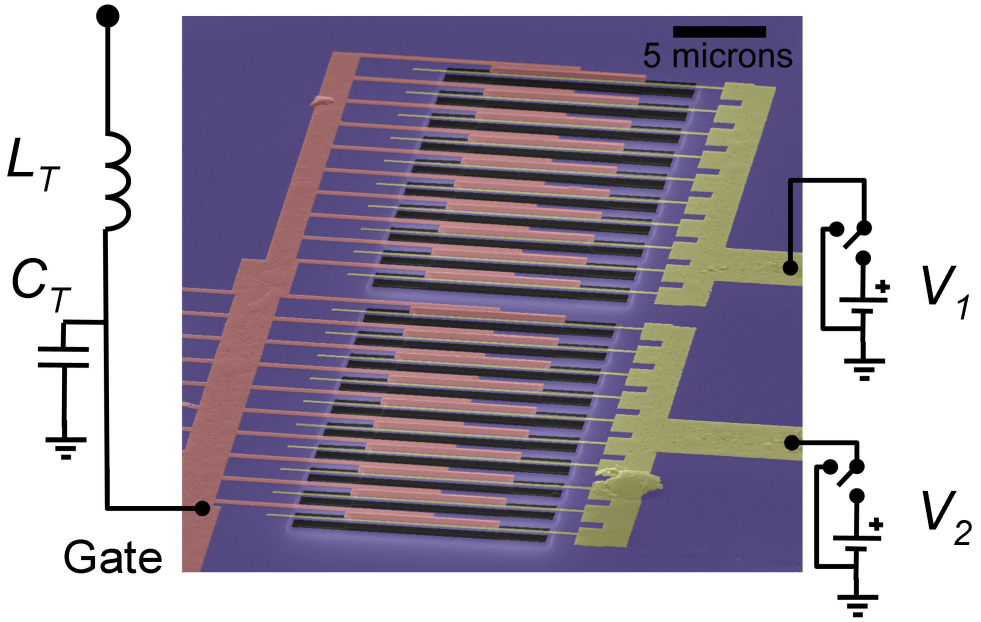

Figure A.8: SEM photo of two arrays of 10 resonators each with schematic showing ability to select which array of resonators is measured. The two arrays share a read-out circuit, but can be biased individually.

beams each. Both arrays are connected to a single gate and tank circuit read-out line, but can be biased individually, as shown in Fig. A.8. By choosing which array to apply a non-zero bias voltage to, we could choose which set of nanoresonators we observed.

When measuring a single array, the essential point is that off resonance the mechanical impedance is quite high, so that as long as the nanoresonators are separated in frequency (which is nearly always the case due to the beams' high quality factors and sensitive frequency dependance on minor variations in fabrication) a single mechanical resonance will not be appreciably loaded by the other nanoresonators sharing the circuit. Figure A.9 demonstrates that we can successfully measure several resonances from each array.

The number of nanoresonators that can be read-out by a single tank circuit

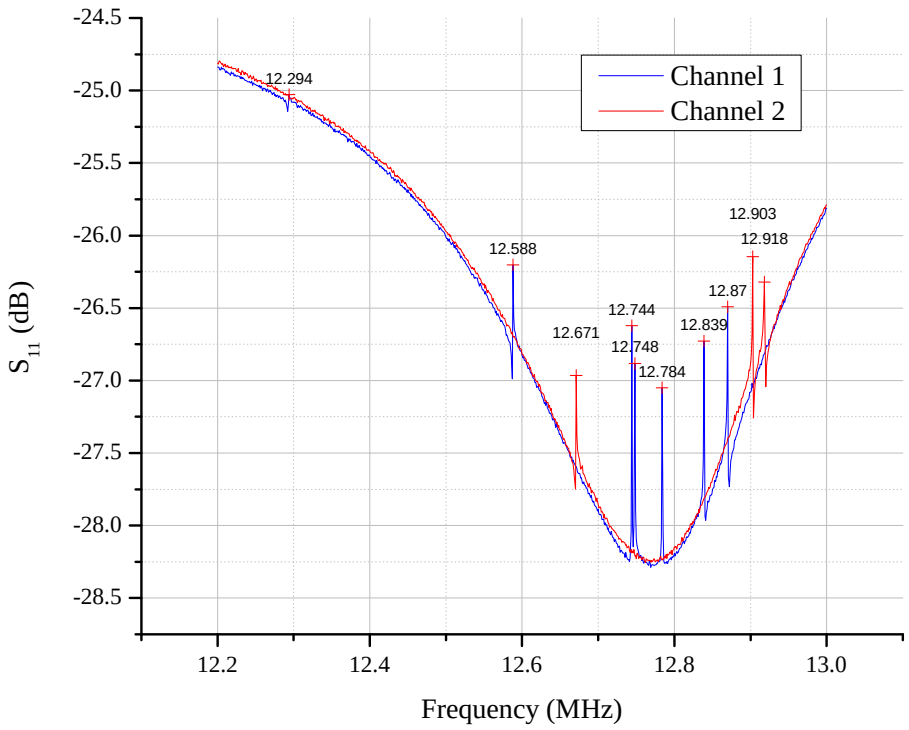

Figure A.9: Demonstration of array resonances.

is mainly determined by the ratio of the nanoresonator quality factor to the quality factor of the tank circuit, which in our experiments is typically on the order of $10^3 - 10^4$. For an application such as frequency-based molecular mass sensing, for which having the ability to read-out multiple nanoresonators functionalized to be sensitive to different molecules would be attractive, the nanoresonators would need to be separated in frequency enough to allow for the necessary frequency shifts. A single molecule, for instance, is expected to shift a nanoresonator's frequency by $\sim 10 - 100$ Hz [4].

A.3 Parametric Amplification

Having a nearby gate electrode capacitively coupled to the nanoresonator is also ideal for a form of amplification known as parametric amplification. There are two types of parametric amplification, degenerate and non-degenerate. In the degenerate case, a parameter of a resonant system is modulated at twice the resonance frequency with the result that energy is "pumped" into the system [54]. This amplification only supplies energy to oscillations in phase with the pump.

In mechanical resonators, modulating the spring constant at $2\omega_0$ increases the amplitude of the mechanical oscillations. To show that we could achieve gain with this method, we used the setup shown in Fig. A.10. The resonator was driven and detected using the magnetomotive technique [8], while a small AC voltage at $2\omega_0$ was sent to the gate to modulate the spring constant through Eq. A.6.

For pump voltage V_p and relative phase between pump and drive θ, the gain

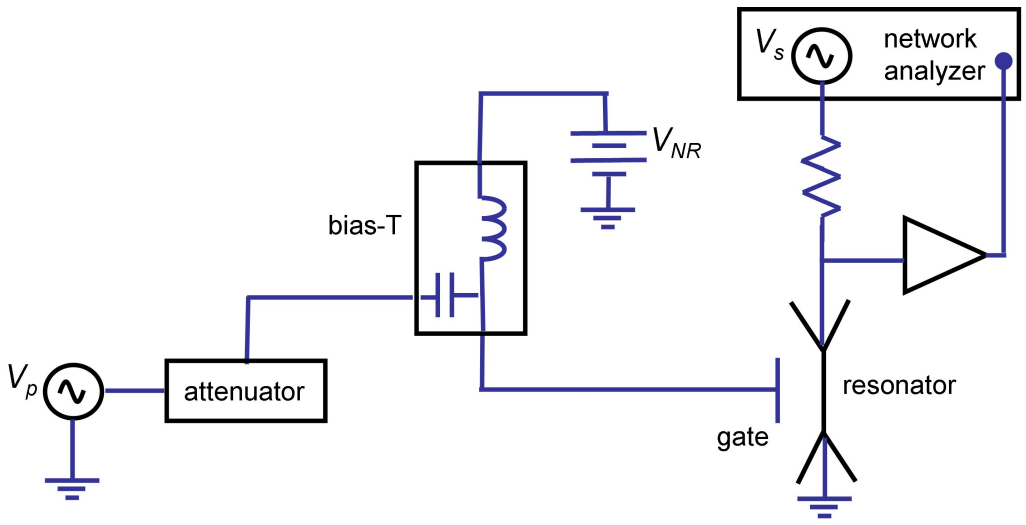

Figure A.10: Schematic of measurement setup for testing parametric amplification.

is given by [55]

$$G(\theta) = \frac{cos^2\theta}{(1 + V_p/V_T)^2} + \frac{sin^2\theta}{(1 - V_p/V_T)^2} \tag{A.9}$$

where V_T is the theshold pump voltage above which the system is excited into self-oscillation. Figures A.11 and A.12 show the measured gain of the system vs. the pump phase and amplitude, respectively. The fit uses $V_p/V_T = 0.68$. A rough estimate for this ratio was 0.83.

A.4 Coupled Transverse Modes

Throughout this thesis, I have only dealt with the fundamental transverse mode of a nanoresonator moving in the plane of the substrate: the in-plane mode. The detection schemes described are most sensitive to this mode. There is however, another, perpindicular mode: the out-of-plane mode. In the linear regime, the two modes are independent of each other and obey Eq. 1.5. However, if we include

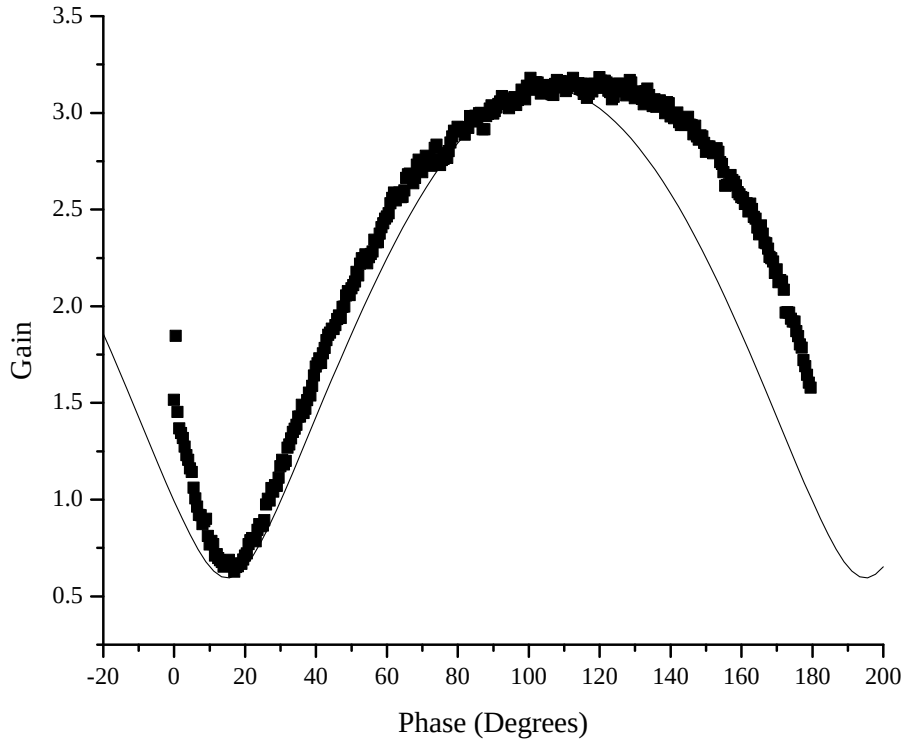

Figure A.11: Gain vs. relative phase between drive and pump signals.

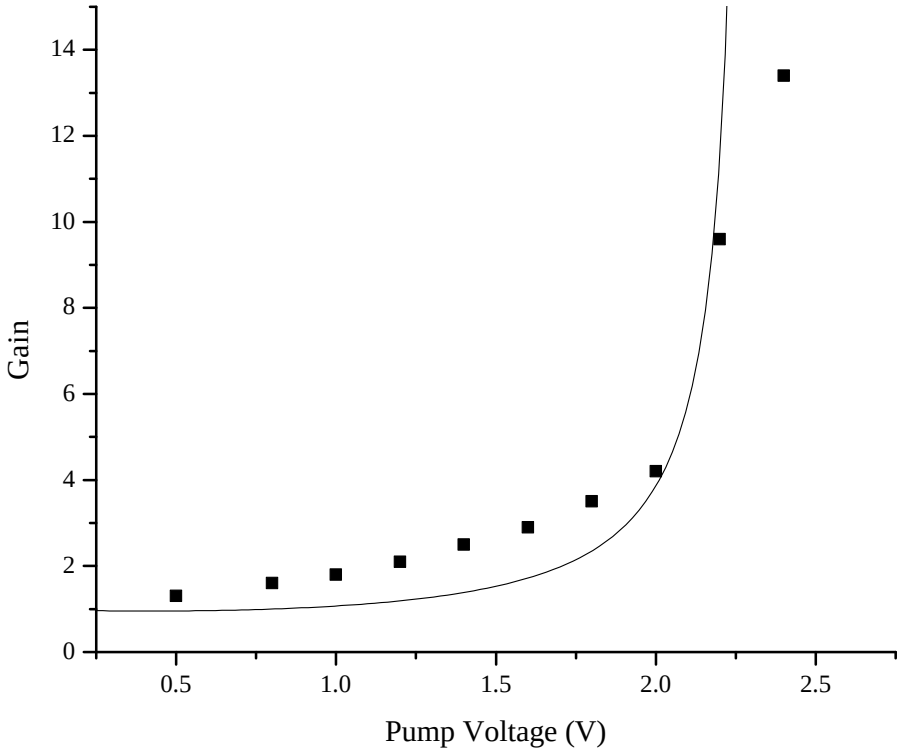

Figure A.12: Gain vs. pump signal amplitude.

the effect of tension, the modes are governed by a system of coupled differential equations

$$M\left(\frac{\mathrm{d}^2X}{\mathrm{d}t^2}+\frac{\omega_{0,\mathrm{x}}}{Q_\mathrm{x}}\frac{\mathrm{d}X}{\mathrm{d}t}\right)+K_\mathrm{x}X+K_3(X^3+Y^2X)=F_\mathrm{x} \tag{A.10}$$

$$M\left(\frac{\mathrm{d}^2Y}{\mathrm{d}t^2}+\frac{\omega_{0,\mathrm{y}}}{Q_\mathrm{y}}\frac{\mathrm{d}Y}{\mathrm{d}t}\right)+K_\mathrm{y}Y+K_3(Y^3+X^2Y)=F_\mathrm{y} \tag{A.11}$$

where X and Y refer to the in-plane and out-of-plane modes, respectively. K is the usual spring constant that has been used throughout this thesis and can include the electrostatic contribution given in Eq. A.6. It can be different for the two modes, since it depends on the geometry of the sample relative to its motion. The frequency, ω_0, is the resonant frequency without tension. K_3 is the nonlinear spring constant given by

$$K_3=\frac{AE}{2L}\left[\int_{-L/2}^{L/2}\left(\frac{\mathrm{d}u(z)}{\mathrm{d}z}\right)^2\mathrm{d}z\right]^2 \tag{A.12}$$

and describes the effect of tension of the beam as it is stretched when it undergoes displacement from its equilbrium position. The first nonlinear term in each equation is the effect of tension from that mode's own motion and gives the well known Duffing resonator response [56]. The second nonlinear term describes the coupling between the two modes, i.e. as one mode displaces, the resulting tension in the beam affects the other mode. For nondegenerate mode frequencies, I can substitute sinusoidal solutions $X(t)=X_0\cos\omega_x t$ and $Y(t)=Y_0\cos\omega_y t$. Solving for the mode frequencies as a function of the amplitudes (ignoring nonsecular terms in X^3, Y^3, X^2Y and

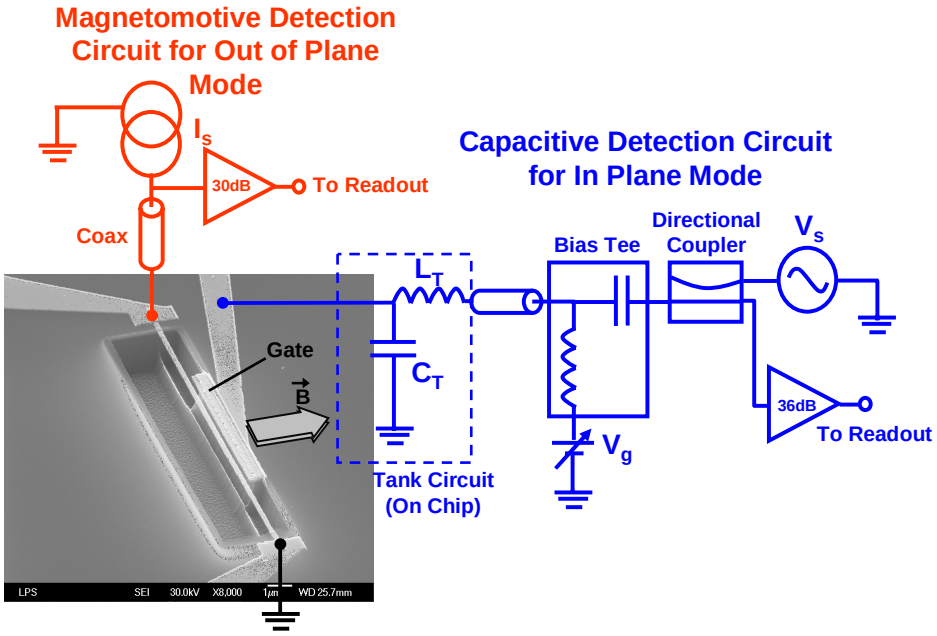

Figure A.13: Setup for measuring coupled transverse modes. The amplifier used to readout the out of plane mode (CLC425) has a 3 kΩ input impedance (DC resistance of beam $\simeq$ 1.6 kΩ), while a tank circuit (L_t = 62 μH, C_t = 5.4 pF) is used to match the impedance of the in plane mode to a 50 Ω amplifier (Miteq).

Y^2X), I find

$$\omega_x = \omega_{0,x}\left(1 + \frac{3}{8}\frac{K_3}{K_{1,x}}X_0^2 + \frac{1}{4}\frac{K_3}{K_{1,x}}Y_0^2\right), \tag{A.13}$$

$$\omega_y = \omega_{0,y}\left(1 + \frac{3}{8}\frac{K_3}{K_{1,y}}Y_0^2 + \frac{1}{4}\frac{K_3}{K_{1,y}}X_0^2\right). \tag{A.14}$$

We used the setup shown in Fig. A.13 to investigate the mode coupling for a 16.2 μm by 220 nm by 125 nm nanoresonator with an estimated mass of 1.3 $\times$ 10^{-15} kg. The sample was oriented in a magnetic field such that the out-of-plane mode could be easily detected magnetomotively. At low excitation, the resonant

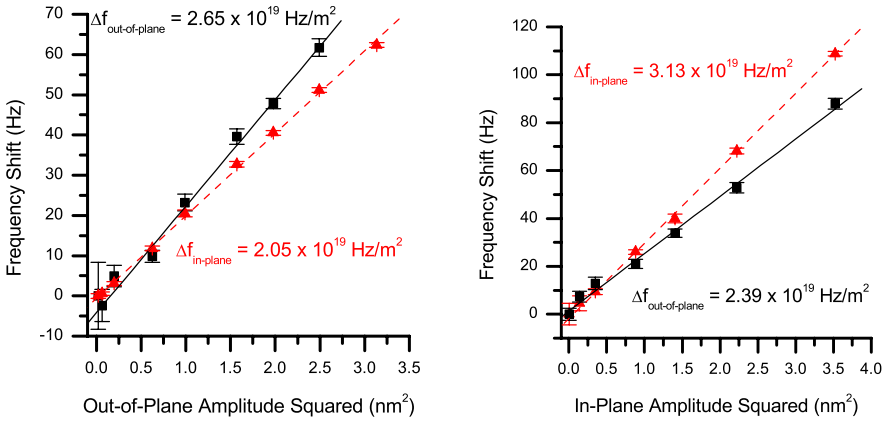

(a) (b)

Figure A.14: Measured frequency shift of out of plane and in plane modes versus out of plane (a) and in plane (b) amplitudes. Lines are linear fits to the data.

frequencies were found to be $\omega_{0,\mathrm{x}} = 2\pi$ 8417243 rad/s and $\omega_{0,\mathrm{y}} = 2\pi$ 8741763 rad/s, giving linear spring constants of (from $K = M\omega_0^2$) $K_\mathrm{x} = 5.3$ Nt/m and $K_\mathrm{y} = 5.75$ Nt/m.

We measured the non-linear response and non-linear mode coupling by measuring the change in resonance frequency while either increasing the drive on the measured mode (Duffing response) or increasing the drive on the orthogonal mode (frequency pulling).

Figure A.14 shows the results of these measurements. In both cases, the Duffing and frequency pulling slopes differ by a factor of about 1.2. Assuming that the spring constants are identical (which they nearly are), then equations (A.13) and (A.14) predict that this ratio should be $\frac{3}{2}$.

We also measured the mode frequencies versus the bias voltage V_{NR}. The in-plane mode frequency decreases with increasing bias as in Eq. A.8 and Fig. A.7.

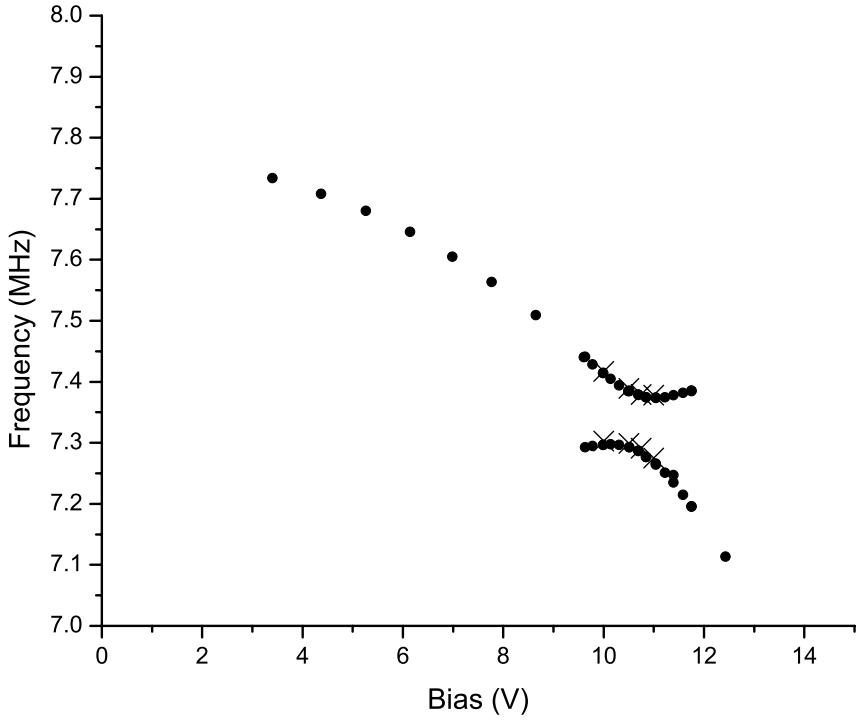

Figure A.15: Frequency of in-plane and out-of-plane modes vs. bias voltage V_{NR}. (·)-magnetomotive detection, (×)-capacitive detection.

In contrast, the out-of-plane mode increases in frequency since $\partial^2 C(X_0)/\partial Y^2$ is negative. Since in our case the in-plane mode begins at the higher frequency, the frequencies may be expected to cross at some point. Instead, we find the data shown in Fig. A.4: an avoiding crossing around $V_{NR} = 10$ V, indicating a coupling between the modes. Because the effect did not depend on detection method or drive level, we conclude that this is not due to the nonlinear effects described earlier, but rather is a linear coupling.

At least part of this coupling can be attributed to the electrostatics. To take

into account the presence of both modes we have to need to work with the Taylor expansion of the capacitance in two dimensions

$$\begin{aligned} C(X,Y) =& C(0,0) + \frac{\partial C}{\partial X}\,|_{0,0}\, X + \frac{\partial C}{\partial Y}\,|_{0,0}\, Y \\ &+ \frac{1}{2}\frac{\partial^2 C}{\partial X^2}\,|_{0,0}\, X^2 + \frac{1}{2}\frac{\partial^2 C}{\partial Y^2}\,|_{0,0}\, Y^2 + \frac{\partial^2 C}{\partial X \partial Y}\,|_{0,0}\, XY \end{aligned} \tag{A.15}$$

The forces on the two modes due to the electrostatics become

$$F_X = \frac{V^2}{2}\left[\frac{\partial C}{\partial X}\,|_{0,0} + \frac{1}{2}\frac{\partial^2 C}{\partial X^2}\,|_{0,0}\, X + \frac{\partial^2 C}{\partial X \partial Y}\,|_{0,0}\, Y\right] \tag{A.16}$$

$$F_Y = \frac{V^2}{2}\left[\frac{\partial C}{\partial X}\,|_{0,0} + \frac{1}{2}\frac{\partial^2 C}{\partial Y^2}\,|_{0,0}\, Y + \frac{\partial^2 C}{\partial X \partial Y}\,|_{0,0}\, X\right] \tag{A.17}$$

The first term in each of the above expressions describe the static deflecting. Note that if the beam and gate are in the same plane, then the first term in F_Y will be zero. The second term gives the electrostatic contribution to the spring constant, as discussed previously. The third term represents the coupling between the two modes due to the capacitance.

This coupling leads to the modes not being completely in-plane or out-of-plane. Magnetomotive experiments with the sample in different orientations in the magnetic field indicate that the modes do stay linearly polarized, but the planes they oscillate in rotate as the bias voltage is increased. This coupling may explain the abnormally high masses found in Fig. 4.15: if some of the motion was not in the plane of the resonator and SET, the observed motion would be less and give the impression of a larger mass.

Axial Length (m)	Length of Side (m)	Natural Frequency f (Hz)	Frequency Shift Δf (Hz)	$\Delta f/f$
10^{-6}	10^{-7}	1.03×10^{9}	2.4×10^{-5}	2.33×10^{-14}
10^{-5}	10^{-7}	1.03×10^{7}	2.4×10^{-6}	2.33×10^{-13}
10^{-6}	10^{-8}	1.03×10^{8}	2.4×10^{-1}	2.33×10^{-9}
10^{-5}	10^{-8}	1.03×10^{6}	2.4×10^{-2}	2.33×10^{-8}
10^{-6}	10^{-9}	1.03×10^{7}	2.4×10^{3}	2.33×10^{-4}
10^{-5}	10^{-9}	1.03×10^{5}	2.4×10^{2}	2.33×10^{-3}

Table A.2: Frequency and pulling frequency shift for a square cross section Si_3N_4 beam of various dimensions. The frequency shift is for 1 quanta of motion in the mode that does the pulling.

Quadratic coupling between two resonators has been proposed as a means of performing non-linear detection for quantum measurement [57]. Here, we have two modes of the same resonator coupled through the non-linear spring constant, K_3. The expressions for the eigenfrequencies given in (A.13) and (A.14) indicate the design a beam must have in order to maximize the non-linear effect of one mode's motion on the frequency of the other mode. For instance, as the square of the in-plane amplitude increases, the out of plane frequency goes as $K_3/(MK_{1,\mathrm{x}})^{1/2}$. Using the expressions for K and K_3 and considering a homogeneous prismatic beam (so $EI_{\mathrm{x}} = Ewh^3/12$, where h is the thickness in the direction of the out of plane mode and w is the width), we find that the frequency shift goes as $L^{-2}h^{-1}$. Thus, a short narrow beam will maximize the nonlinear coupling between the two modes. Table A.2 shows the frequency shift expected in one mode of a square cross-section resonator for one quantum in the other mode. These shifts are not observable with current technology.

Bibliography

[1] D. Rugar, C. S. Yannoni, and J. A. Sidles. Mechanical detection of magnetic resonance. *Nature*, 360(6404):563–566, December 1992.

[2] C.T.-C. Nguyen. Frequency-selective mems for miniaturized low-power communication devices. *Microwave Theory and Techniques, IEEE Transactions on*, 47(8):1486–1503, 1999.

[3] K. L. Ekinci, X. M. H. Huang, and M. L. Roukes. Ultrasensitive nanoelectromechanical mass detection. *Applied Physics Letters*, 84(22):4469–4471, 2004.

[4] Y.T. Yang, C. Callegari, X.L. Feng, K.L. Ekinci, and M.L. Roukes. Zeptogram-scale nanomechanical mass sensing. *Nano Lett.*, 6(4):583–586, April 2006.

[5] E. K. Irish and K. Schwab. Quantum measurement of a coupled nanomechanical resonator-cooper-pair box system. *Phys. Rev. B*, 68(15):155311–, October 2003.

[6] A. N. Cleland and M. R. Geller. Superconducting qubit storage and entanglement with nanomechanical resonators. *Physical Review Letters*, 93(7):070501, 2004.

[7] D. M. Karabacak, V. Yakhot, and K. L. Ekinci. High-frequency nanofluidics: An experimental study using nanomechanical resonators. *Physical Review Letters*, 98(25):254505, 2007.

[8] A. N. Cleland and M. L. Roukes. External control of dissipation in a nanometer-scale radiofrequency mechanical resonator. *Sensors and Actuators A: Physical*, 72(3):256–261, February 1999.

[9] Matthias Imboden, Pritiraj Mohanty, Alexei Gaidarzhy, Janet Rankin, and Brian W. Sheldon. Scaling of dissipation in megahertz-range micromechanical diamond oscillators. *Applied Physics Letters*, 90(17):173502, 2007.

[10] S. Reid, C. Cagnoli, D.R.M. Crooks, J. Hough, Pl Murray, and S. Rowan. Mechanical dissipation in silicon flexures. In *22nd Texas Symposium of Relativistic Astrophysics at Stanford University*, 2004.

[11] P. Mohanty, D. A. Harrington, K. L. Ekinci, Y. T. Yang, M. J. Murphy, and M. L. Roukes. Intrinsic dissipation in high-frequency micromechanical resonators. *Phys. Rev. B*, 66(8):085416–, August 2002.

[12] L. D. Landau and E. M. Lifshitz. *Theory of Elasticity*. Oxford: Butterworth-Heinemann, 1986.

[13] Y. T. Yang, K. L. Ekinci, X. M. H. Huang, L. M. Schiavone, M. L. Roukes, C. A. Zorman, and M. Mehregany. Monocrystalline silicon carbide nanoelectromechanical systems. *Applied Physics Letters*, 78(2):162–164, 2001.

[14] Andrew N. Cleland. *Foundations of Nanomechanics: From Solid-State Theory to Device Applications*. New York: Springer, 2003.

[15] B. Yurke, D. S. Greywall, A. N. Pargellis, and P. A. Busch. Theory of amplifier-noise evasion in an oscillator employing a nonlinear resonator. *Phys. Rev. A*, 51(5):4211–4229, May 1995.

[16] R. Kubo. The fluctuation-dissipation theorem. *Reports on Progress in Physics*, 29(1):255–284, 1966.

[17] A. V. Shytov, L. S. Levitov, and C. W. J. Beenakker. Electromechanical noise in a diffusive conductor. *Phys. Rev. Lett.*, 88(22):228303–, May 2002.

[18] Private communication with Andrei Shytov.

[19] Andrew H. Steinbach, John M. Martinis, and Michel H. Devoret. Observation of hot-electron shot noise in a metallic resistor. *Phys. Rev. Lett.*, 76(20):3806–, May 1996.

[20] D. E. Prober. Comment on "crossover between dissipative and nondissipative electron transport in metal wires". *Phys. Rev. Lett.*, 75(21):3964–, November 1995.

[21] Peter John Burke. *High Frequency Electron Dynamics in Thin Film Superconductors and Applications to Fast, Sensitive THz Detectors*. PhD thesis, Yale University, 1997.

[22] P.A. Truitt, J.B. Hertzberg, C.C. Huang, K.L. Ekinci, and K.C. Schwab. Efficient and sensitive capacitive readout of nanomechanical resonator arrays. *Nano Lett.*, 7(1):120–126, January 2007.

[23] K. L. Ekinci and M. L. Roukes. Nanoelectromechanical systems. *Review of Scientific Instruments*, 76(6):pN.PAG –, 20050601.

[24] L. Lin, C. T. Nguyen, R. T. Howe, and A. P. Pisano. Microelectromechanical filters for signal processing. *Technical Digest, IEEE Microelectromechanical Systems Workshop, Travemunde, Germany*, pages 226–231, 1992.

[25] A. N. Korotkov. Intrinsic noise of the single-electron transistor. *Phys. Rev. B*, 49(15):10381–, April 1994.

[26] D. V. Averin and K. K. Likharev. Coulomb blockade of single-electron tunneling, and coherent oscillations in small tunnel junctions. *Journal of Low Temperature Physics*, 62(3):345–373, February 1986.

[27] Robert G. Knobel and Andrew N. Cleland. Nanometre-scale displacement sensing using a single electron transistor. *Nature*, 424(6946):291–293, July 2003.

[28] M. D. LaHaye, O. Buu, B. Camarota, and K. C. Schwab. Approaching the quantum limit of a nanomechanical resonator. *Science*, 304(5667):74–77, 2004.

[29] Akshay Naik. *Near Quantum Limited Measurement in Nanoelectromechanical Systems*. PhD thesis, The University of Maryland, 2006.

[30] R. J. Schoelkopf, P. Wahlgren, A. A. Kozhevnikov, P. Delsing, and D. E. Prober. The radio-frequency single-electron transistor (rf-set): A fast and ultrasensitive electrometer. *Science*, 280(5367):1238–1242, 1998.

[31] Nems and Nanotechnology Exchange, Reston, VA 20191, tel. (703) 262-5368.

[32] T. A. Fulton and G. J. Dolan. Observation of single-electron charging effects in small tunnel junctions. *Phys. Rev. Lett.*, 59(1):109–112, Jul 1987.

[33] G. J. Dolan. Offset masks for lift-off photoprocessing. *Applied Physics Letters*, 31(5):337–339, 1977.

[34] Liudi Jiang, R. Cheung, R. Brown, and A. Mount. Inductively coupled plasma etching of SiC in SF6O2 and etch-induced surface chemical bonding modifications. *Journal of Applied Physics*, 93(3):1376–1383, 2003.

[35] Liudi Jiang, R. Cheung, M. Hassan, A. J. Harris, J. S. Burdess, C. A. Zorman, and M. Mehregany. Fabrication of SiC microelectromechanical systems using one-step dry etching. *Journal of Vacuum Science & Technology B: Microelectronics and Nanometer Structures*, 21(6):2998–3001, 2003.

[36] L1.5-30H by Berkshire Technologies, Oakland, Ca 94609, Tel. (510) 655-1986.

[37] Mini-Circuits, Brooklyn, NY 11235, Tel., (718) 934-4500.

[38] P. Wahlgren. *The Radio-Frequency Single-Electron Transistor and the Horizon Picture for Tunneling*. PhD thesis, Chalmers University of Technology, Goteborg University, 1998.

[39] ICEoxford, Oxford, UK, tel. +44 (0) 1865 202300.

[40] A. A. Clerk and S. Bennett. Quantum nano-electromechanics with electrons, quasiparticles and cooper pairs: effective bath descriptions and strong feedback effects. *New Journal of Physics*, 7:238, 2005.

[41] John M. Martinis, Michel H. Devoret, and John Clarke. Experimental tests for the quantum behavior of a macroscopic degree of freedom: The phase difference across a josephson junction. *Phys. Rev. B*, 35(10):4682–4698, Apr 1987.

[42] Neil W. Ashcroft and N. David Mermin. *Solid State Physics*. Brooks Cole, 1976.

[43] A. B. Hutchinson, P. A. Truitt, K. C. Schwab, L. Sekaric, J. M. Parpia, H. G. Craighead, and J. E. Butler. Dissipation in nanocrystalline-diamond nanomechanical resonators. *Applied Physics Letters*, 84(6):972–974, 2004.

[44] B. E. White and R. O. Pohl. Elastic properties of thin films. In *Material Research Society Symposium Proceedings*, 1995.

[45] IEEE Micro Electro Mechanical Systems Workshop,Feb 1993, Florida, p.25.

[46] Osamu Tabataa, Ken Kawahataa, Susumu Sugiyamaa, and Isemi Igarashia. Mechanical property measurements of thin films using load-deflection of composite rectangular membranes. *Sensors and Actuators*, 20:135, 2002.

[47] X.M.H. Huang, X.L. Feng, C.A. Zorman, M. Mehregany, and M.L. Roukes. Vhf, uhf and microwave frequency nanomechanical resonators. *New J. Phys.*, 7:247, 2005.

[48] P. Santhanam, S. Wind, and D. E. Prober. Localization, superconducting fluctuations, and superconductivity in thin films and narrow wires of aluminum. *Phys. Rev. B*, 35(7):3188–3206, Mar 1987.

[49] I. Yu Borisenko, V. I. Kuznetsov, V. A. Tulin, and D. Esteve. Thin-film aluminum microstructure as a hot-electron microwave radiation detector. *Journal of Low Temperature Physics*, 119:483, 2000.

[50] Matt. D. LaHaye. *The Radio-Frequency Single-Electron Transistor Displacement Detector*. PhD thesis, The University of Maryland, 2005.

[51] F. C. Wellstood, C. Urbina, and John Clarke. Hot-electron effects in metals. *Phys. Rev. B*, 49(9):5942–, March 1994.

[52] D. R. Schmidt, C. S. Yung, and A. N. Cleland. Temporal measurement of hot-electron relaxation in a phonon-cooled metal island. *Physical Review B (Condensed Matter and Materials Physics)*, 69(14):140301, 2004.

[53] A. N. Cleland and M. L. Roukes. A nanometre-scale mechanical electrometer. *Nature*, 392:160–162, 1998.

[54] William H. Louisell. *Coupled Mode and Parametric Electronics*. New York: Wiley, 1960.

[55] D. Rugar and P. Grütter. Mechanical parametric amplification and thermomechanical noise squeezing. *Phys. Rev. Lett.*, 67(6):699–702, Aug 1991.

[56] Ronen Almog, Stav Zaitsev, Oleg Shtempluck, and Eyal Buks. Signal amplification in a nanomechanical duffing resonator via stochastic resonance. *Applied Physics Letters*, 90(1):013508, 2007.

[57] D. H. Santamore, Hsi-Sheng Goan, G. J. Milburn, and M. L. Roukes. Anharmonic effects on a phonon number measurement of a quantum mesoscopic mechanical oscillator. *Physical Review A*, 70:052105, 2004.